2015

First-principles Study of Superconducting MAX Phases

Hadi, Md. Abdul

University of Rajshahi

First-principles Study of Superconducting MAX Phases

A Dissertation by

Md. Abdul Hadi
Roll No. 10214, Registration No. 12068
Session: 2010-2011

Submitted to the University of Rajshahi
in Candidacy for the Degree of
MASTER OF PHILOSOPHY
in Physics

University of Rajshahi

Condensed Matter Physics
Department of Physics
University of Rajshahi, Bangladesh
Rajshahi-6205
June, 2015

To
My daughter
Lutfia Jaima Suha

Declaration

The work presented in the thesis entitled "*First-principles Study of Superconducting MAX Phases*" was carried out by the author in the Condensed Matter Physics Lab. in the Department of Physics, University of Rajshahi, Bangladesh. The work has not been submitted for any other degree in the University of Rajshahi or elsewhere, and unless stated otherwise, is the original work of the author.

The Author
(Md. Abdul Hadi)
June, 2015

Professor Saleh Hasan Naqib
M.Sc. (Raj), PhD (Cambridge)
Regular Associate, AS-ICTP, Trieste, Italy

Department of Physics
University of Rajshahi
Rajshahi-6205, Bangladesh
Tel. : +880721750041/4102 (0ff)
E-mail : salehnaqib@yahoo.com

Certificate

I hereby certify that the thesis entitled "First-principles Study of Superconducting MAX Phases" submitted by Md. Abdul Hadi, Department of Physics, University of Rajshahi, Rajshahi, Bangladesh, has been completed under my direct supervision. This is a bona fide record of the research carried out by the candidate.

To the best of my knowledge, this thesis has not been submitted for the award of any degree or award elsewhere.

(*Saleh Hasan Naqib*)
Principal Supervisor

(*A. K. M. Azharul Islam*)
Co-Supervisor

Abstract

First-principles investigation of the structural, elastic, electronic, thermodynamic and optical properties along with theoretical hardness of the four superconducting MAX compounds Mo_2GaC, Nb_2AsC, Nb_2InC and Ti_2GeC have been carried out by the plane-wave pseudopotential method based on the density functional theory (DFT) implemented in the CASTEP code. The hardness has been studied by means of Mulliken bond population analysis and electronic energy density of states. The thermodynamic properties are derived from the quasi-harmonic Debye model with phononic effect. The calculated structural properties are in excellent agreement with experiments. The pressure effect on the structural properties of these MAX compounds has been investigated. The results show that both lattice constants and unit cell volume decrease almost linearly with the increase of pressure, while the hexagonal ratio increases gradually with increasing pressure. This implies that the lattice constant *a* decreases at a faster rate than *c*. Thus, the compressibility along *c*-axis is lower than that along *a*-axis. Our results on the elastic parameters indicate the elastic anisotropy and brittleness of the compounds. Nb_2InC and Ti_2GeC possess small elastic anisotropy but for other two phases it is comparatively large since they exhibit the maximal deviation from unity. The calculated elastic constants at different pressures exhibit the monotonous increase of the five independent elastic constants C_{ij} with the pressure up to 50 GPa and satisfy the Born criteria for the mechanical stability with the prediction of no phase transition of the studied four MAX phases. The electronic structures calculations reveal that the chemical bonding of the MAX nanolaminates may be a combination of covalent, ionic and metallic in nature. The phase Nb_2AsC is relatively soft and easily machinable compared to the other three metallic-ceramics due to its lowest hardness value. The investigated Fermi surfaces are formed mainly by the low-dispersive bands, which should be responsible for the presence of superconductivity in the four MAX materials. All optical functions are determined and analyzed for two different polarization directions. The theoretical findings are compared with available experimental data. The reflectivity spectra imply that the four MAX phases are the potential candidate materials for coating to reduce the solar heating. Finally, the thermodynamic properties such as bulk modulus, Debye temperature, volume thermal expansion coefficient and specific heats have been investigated successfully and analyzed in detail.

List of papers

A. List of papers relevant to this thesis

1. ***Band Structure, Hardness, Thermodynamic and Optical Properties of Superconducting Nb_2AsC, Nb_2InC and Mo_2GaC***

M. A. Hadi, M. S. Ali, S. H. Naqib, and A. K. M. A. Islam

International Journal of Computational Materials Science and Engineering, Vol. 2, Issue 2, Article ID 1350007 (2013);

DOI: 10.1142/S2047684113500073

2. ***New MAX Phase Superconductor Ti_2GeC: A First-principles Study***

M. A. Hadi, M. Roknuzzaman, F. Parvin, S. H. Naqib, A. K. M. A. Islam, and M. Aftabuzzaman

Journal of Scientific Research, Vol. 6, Issue 1, Pages 11-27 (2014);

DOI: htt://dx.doi.org/10.3329/jsr.v6i1.16604

B. List of papers relevant to the first-principles study

1. ***Zirconium Metal Based MAX Phases Zr_2AC (A = Al, Si, P and S): A First-principles Study***

M. T. Nasir, **M. A. Hadi**, S. H. Naqib, F. Parvin, A. K. M. A. Islam, M. Roknuzzaman, and M. S. Ali

International Journal of Modern Physics B, Vol. 28, Issue 32, Article ID 1550022 (2014);

DOI: 10.1142/S0217979215500228

2. ***Physical Properties of Predicted Ti_2CdN versus Existing Ti_2CdC MAX Phase: An ab initio Study***

M. Roknuzzaman, **M. A. Hadi**, M. J. Abden, M. T. Nasir, A. K. M. A. Islam, M. S. Ali, K. Ostrikov, and S. H. Naqib

Submitted into the Journal Computational Material Science

3. ***A First-principles Study of a New Ternary Silicide Superconductor Li_2IrSi_3***

M. A. Hadi, M. A. Alam, M. Roknuzzaman, M. T. Nasir, A. K. M. A. Islam, and S. H. Naqib

Presented and submitted into the International Conference on Advances in Physics (ICAP 2015), held on April 18-19, 2015,

Organized by Department of Physics, University of Rajshahi, Bangladesh and Bangladesh Physical Society

Acknowledgement

I would like to express my sincere gratefulness to my honorable teacher Professor Dr. A K M Azharul Islam who agreed to supervise me as a research fellow for the M.Phil. degree at Rajshahi University. Initially, my research work advanced under his supervision with patience, guidance, encouragement and motivation. He had to take the charge as the Vice Chancellor of International Islamic University, Chittagong, Bangladesh. According to the regulations of Rajshahi University, his position was changed from Principal supervisor to Co-supervisor. In spite of being extremely busy, he always finds time for me for discussions and feedback on my research. I have learned a lot from him about how to write a research paper. I am really grateful that he brings me to the exciting research field of MAX phases.

Next, I would like to confer my appreciation to Professor Dr. Saleh Hasan Naqib who switched from Co-supervisor to Principal supervisor. From the beginning of my research, he has been supporting me and pushing my boundaries of science towards more research with quality and quantity. Most importantly, he has given me the friendly association and guidance in the entire period of my work.

I want to express my gratitude to my respected teacher Professor Dr. M Musfiqur Rahman, Former Chairman, Department of Physics, University of Rajshahi, who gave me the kind permission to carry out this research work. He left us in the days when I was finishing this study. I pray that his departed soul may rest in peace.

I am also thankful to my honorable teacher Professor Dr. Somnath Bhattacharjee, Incumbent Chairman, Department of Physics, University of Rajshahi, who always provided me with all the supports related to the academic and administrative affairs.

I am expressing my deep sense of overwhelming gratitude and immense respect to my teacher Professor Emeritus Dr. Arun Kumar Basak who always gives us the shelter under the shed of his tenderness.

I also express my immense feelings of gratitude to my teacher Mr. M Rezaul Islam Mollah who has taught us more than Physics. He was a kind and gentle soul who was endowed with a great sense of humor. His good humor should be an example for us all to follow. He was not so old to leave us. I pray for his departed soul.

Now, I would like to give my heartfelt thanks to my honorable teachers Professor Dr. M Aminul Islam, Professor Dr. M Golam Mortuza, Professor Dr. M Alfaz Uddin, Professor Dr. M Khalilur Rahman Khan, Professor Dr. M Rafiqul Ahsan, Professor Dr. F Nazrul Islam, Mr. A F M Abdul Wahed, and Dr. M Rezaur Rahim. They always wish me success in my present research.

Then I would like to thank Dr. Fahmida Parveen for her useful discussions, nice collaboration, and help for my understanding of every concept in the field. Also, my special thanks would go to Dr. M Abdur Razzaque Sarker, Dr. M Atiqur Rahman Patoary, Mr. M Masum Billah, Mr. M Leaket Ali, Mr. M Alomgir Hassan and Mr. M Saiful Islam for their encouragement and support all through my present study.

I also want to thank all younger researchers, former and current, in the CMP Lab, namely, Mr. M Anower Hossain, Mr. M Abtabuzzaman, Mr. M Mozahar Ali, Mr. M Mukter Hossain, Mr. M Ashraf Ali, Mr. M Al-Helal, Mr. M Shahjahan Ali, Mr. M Zahid Hassan, Mr. M Roknuzzaman, Mr. M T Nasir and Mr. Abu Rayhan. Without their cordial association, I could not make this thesis a complete one. I would like to extend my thanks to all those who helped me from behind but were not listed here.

I am indebted to Dr. Yuxiang Mo who currently works at University of Pennsylvania as a Postdoctoral Researcher on DFT exchange-correlation functionals and long-range van der Waals interactions. He was always ready to help me whenever I asked.

I would like to thank all my colleagues, especially Mr. M Abdus Samad Azad, Mr. M Nazmul Hassan, Mr. M Mozzammel Haque Pramanik, Mr. M Kamrul Ahsan, Mr. Sultan Mohammad Alamgir, Mr. M Delower Hossain Pramanik, Mr. M Rabiul Awal Talukder, Mr. M Anower Hossain, Mr. Ahmedur Rahman, Mr. M Sheehab Uddin for their support.

I acknowledge the support from Ministry of Education and Directorate of Secondary and Higher Education of Bangladesh through providing deputation for two years without which my study could not be completed. I also acknowledge the fellowship of the University Grand Commission of Bangladesh which paved the way of completing my research work smoothly.

The Author
(Md. Abdul Hadi)
June 2015

CONTENTS

LIST OF ACRONYMS

CASTEP	Cambridge Serial Total Energy Package
DFT	Density Functional Theory
DOS	Density of States
EOS	Equation of States
eV	Electron Volts
FCC	Face Centered Cubic
GGA	Generalized Gradient Approximation
GPa	Giga Pascal
HEG	Homogeneous Electron Gas
HCP	Hexagonal Closed Packed
HF	Hartree-Fock
HK	Hohenberg-Kohn
IR	Infrared
LAPW	Linearized Augmented Plane Wave
LDA	Local Density Approximation
LDOS	Local Density of States
LSDA	Local Spin Density Approximation
NMR	Nuclear Magnetic Resonance
PBE	Perdew-Burke-Ernzerhof
PDOS	Projected/Partial Density of States
QM	Quantum Mechanical
STM	Scanning Tunneling Microscopy
TEM	Transmission Electron Microscopy
USP	Ultra Soft Pseudopotentials
UV	Ultra Violet
XC	Exchange-Correlation

LIST OF FIGURES

LIST OF TABLES

1. Introduction

This chapter introduces the main topics covered in this thesis and provides a summary of the objective of this work, along with an outline of how the various chapters are structured.

1.1 Background

The world around us is largely made of *condensed matter*, i.e., matter whose energy is low enough that it has condensed to form stable systems of atoms and molecules, usually in solid or liquid phases. The large variety of ways in which these systems can take form leads to a rich diversity of physical phenomena that is practically endless in scope. Because of this, approaching the field of condensed matter physics from a theoretical or computational angle can be a very important and challenging task to undertake. For most part, the way this is done is to pick a particular macroscopic phenomenon, which has been well studied experimentally, and to build empirical, or semi-empirical models to describe the experimentally observed results. This often provides a good understanding of the physics of the system under study, and it is often possible to interpolate or extrapolate these models in order to predict the behavior of systems under conditions not yet tested experimentally. However, due to the complexity of condensed matter systems, and the difficulty in building accurate models, the predictive power of such an approach can be severely limited.

The *first principles* approach to condensed matter theory is entirely different from this. It starts from what we know about all condensed matter systems - which they are made of atoms, which in turn are made of a positively charged nucleus and a number of negatively charged electrons. The interactions between atoms, such as chemical and molecular bonding, are determined by the interactions of their constituent electrons and nuclei. All of the physics of condensed matter systems arises ultimately from these basic interactions. If we can model these interactions accurately, then all of the complex physical phenomena that arise from them should emerge naturally in our calculations.

The physics that describes the interaction of electrons and nuclei that is relevant to most problems in condensed matter is actually relatively simple. There are only two different types of particle involved, and the behavior of these particles is mostly governed by basic quantum mechanics. What makes first principles calculations difficult is not so much the complexity of the physics, but rather the size of the problem in terms of a numerical formulation. The development of accurate and efficient theoretical and computational techniques for dealing with so many particles is therefore central to the ongoing research in this field. Simply, in physics, a study is said to be from the *first-principles*, or *ab initio*, if it starts directly at the level of established laws of physics and does not make assumptions such as empirical model and fitting parameters. For example, investigation of electronic structure using Schrodinger's equation within a set of approximations that do not include fitting the model to experimental data is an *ab initio* approach, or *first-principles* calculation.

The *MAX phases* are a family of ternary layered condensed compounds of transition metal carbides and nitrides with a unique combination of both metallic and ceramic properties [1], which are stimulating numerous researches with the hope that they will open the door to viable commercial applications for these materials in future. Like metals, they are electrically [2] and thermally [3] conductive, not susceptible to thermal shock [4], plastic at very high temperature [4], exceptionally damage tolerant [5], and most readily machinable [6]. Like ceramics, they are elastically rigid [7], lightweight [8], creep [9], fatigue [10], oxidation [11] and corrosion [12] resistant, and maintain their strengths to high temperatures [4]. These fascinating properties triggered extensive explorations on synthesis, microstructure, property, and design of *MAX phases*, and they highlighted technological perspectives of *MAX phases* as high-performance structural ceramics. The *MAX materials* are developed for defense, aerospace, automotive applications, medical, and portable electronic devices. A detailed study of such materials is important as the MAX phases have many advantages over the commonly used materials. The *MAX phases* are often termed as metallic ceramics due to their metallic and ceramic properties.

The *MAX phases* are thermodynamically stable nanolaminates that possess the chemical formula: $M_{n+1}AX_n$, where *n* is 1, 2, or 3, M is an early transition metal, A is an A-group element, and X is either carbon and/or nitrogen. The terms MAC phases and MAN phases are sometimes used to refer to the *MAX phase* carbides (X = C) and nitrides (X = N) respectively. The *MAX phases* serve as effective nanolaminate materials because of their laminated layers having thickness in the nanometer range. The *MAX phases* aggregate into a big family that includes more than 70 members identified in experiments. There are also about 15 phases predicted theoretically that are awaiting exploration. The *MAX phases* are classified into three groups depending on the number of M, A, and X atoms in the unit cell of the compound: the M_2AX or 211 *MAX phases* (n = 1), M_3AX_2 or 312 *MAX phases* (n = 2), and M_4AX_3 or 413 *MAX phases* (n = 3). Experimental or theoretical evidence supports the possible existence of higher order MAX compounds such as 514 [13], 615 [14], and 716 [15] phases.

Up to now, only eight members of the *MAX family* are identified as low transition temperature T_c superconductors: namely, Mo_2GaC [16], Nb_2SC [17], Nb_2SnC [18], Nb_2AsC [19], Ti_2InC [20], Nb_2InC [21], Ti_2InN [22], and Ti_2GeC [23]. All these superconducting *MAX compounds* belong to the 211 phases. When we started this study, the Ti_2GeC phase was not identified as superconducting phase. By this time a complete study on structural, elastic, electronic, thermodynamic, and optical properties of Nb_2SC and Nb_2SnC as well as Ti_2InC and Ti_2InN has been carried out [24,25]. So, we have restricted our study on Nb_2AsC, Nb_2InC, Mo_2GaC, and Ti_2GeC.

Theoretical studies related to *MAX phase* properties are numerous, ranging from investigations of, e.g., elastic properties to electronic-structure calculations. Such work is relevant to gain knowledge and understanding of existing phases. However, surprisingly little has been done to reflect on whether or not studied phases not yet synthesized can be expected to exist experimentally. Further, the theoretical study is needed to stimulate the experimental research on synthesis and applications of new *MAX compounds* with better characteristics.

1.2 History of MAX phases

Hans Nowotny and his group, in the sixth decade of the twentieth century in Vienna, discovered more than 100 new carbides and nitrides [26-42]. Amongst them were more than thirty, the so-called H-phases that have a M_2AX chemistry, where M is an early transition metal, A is an A-group element comes from column 13 – 16 in the periodic table and X is either C and/or N. They are layered and hexagonal with M_2X layers interleaved with layers of pure A-group element. In 1967, Nowotny and coworkers also discovered Ti_3SiC_2 [35] and Ti_3GeC_2 [36], both of which have the structure similar to the H-phases in which M_3X_2 layers separate the A-layers. Schuster, a coworker of Nowotny and Pietzka added Ti_3AlC_2 as a new member of these phases [43,44]. In spite of these striking achievements, these compounds remained largely unexplored until the 1990s, when several researchers engaged themselves with great interest. The breakthrough contribution that triggered a renaissance came in the mid-1990s, when Barsoum and El-Raghy [2] synthesized relatively phase-pure samples of Ti_3SiC_2 and revealed a material with a unique combination of metallic and ceramic properties. After discovery of Ti_4AlN_3 [45], it became clear that these phases possessed a basic structure that gave them similar properties. This realization led to the introduction of the nomenclature of MAX phases with chemical formula: $M_{n+1}AX_n$, where n varies from 1 to 3 and all symbols represent the same elements as mentioned for H-phases.

The history of H-phases, henceforth referred to as the 211 phases, before 1997, is quite short. Surprisingly, from the time their discovery until the first report of Barsoum and El-Raghy [2]- and apart from the some Russian papers [46-48] in the mid 1970s in which it was claimed that 90-92% dense compacts of Ti_2AlC and Ti_2AlN were synthesized- they were totally ignored. Some magnetic permeability measurements on Ti_2AlC and Cr_2AlC were also reported in 1996 [33]. Nowotny [40] defined H-phases as a synonym for M_2AX phases which are also referred to as Cr_2AlC-type phases after the archetype Cr_2AlC. In MAX phase articles a common misunderstanding is seen that the term H-phase and Hägg phase are synonyms. However, The H in H-phases does not stand for Hägg. Toth [49] in his famous book

'Transition metal carbides and nitrides' published a list for H-phases or Cr_2AlC type phases and shown clearly that H-phases are different from Hägg phases. The H-phases are probably named following an alphabetic system; for example, Nowotny and his coworkers also studied D-phases [50,51], E-phases [52], and G-phases [53]. The erroneous belief that H-phases and Hägg phases are synonyms does not occur outside the MAX phase field; in other fields, the latter term is used in its correct sense: Hägg phases are carbides, nitrides, borides, and hydrides with close-packed or hexagonal arrays of metal atoms in which C, N, B, or H occupy the interstitial octahedral or trigonal sites [49,54]. The H-phases do not fulfill this criterion; the C or N atoms occupy an interstitial octahedral site, but the metal substructure is not close-packed or nearly close-packed.

History of superconducting MAX phases: The compound Mo_2GaC became the first MAX phase, for which superconductivity with transition temperature T_c~ 4 K was discovered in 1967 by Toth [16]. This compound, in fact, the first, and sole, Mo containing MAX phase first synthesized in the same year. Sakamaki *et al*. [17] in 1999 reported the discovery of a new class of superconductors, carbosulfide MAX superconductor, Nb_2SC which was synthesized in 1968 by Backmann *et al* [38]. An experimental study conducted by Bortolozo *et al*. [18] in 2006 revealed that Nb_2SnC shows superconducting transition at ~7.8 K. El-Raghy *et al*. [55] synthesized Nb_2SnC in 2000. In 1968 Beckmann *et al*. [38] synthesized Nb_2AsC first in powder form and Lofland *et al*. [19] in 2006 reported the discovery of its superconducting transition at 2 K. Bortolozo *et al*. [20] in 2007, reported the observation of superconductivity in the Ti_2InC compound with T_c 3.1 K. In 2009, Bortolozo *et al*. [21] showed that Nb_2InC compound superconducts at 7.5 K and Jeitschko *et al*. [31] first synthesized the Nb_2InC phase in 1964. Bortolozo *et al*. [22] in 2010 confirmed that Ti_2InN is the first nitride MAX superconductor which was discovered in 1963 by Jeitschko *et al*. [30]. Recently, in 2012, Bortolozo *et al*. [23] have shown that the bulk superconductivity is induced at 9.5 K in Ti_2GeC. Ti_2GeC was first synthesized in 1963 by Jeitschko *et al*. [29].

1.3 Research objective

The aim of the present study is to investigate the ground state structural, elastic, electronic, optical, and thermodynamic properties along with theoretical Vickers hardness of the four superconducting MAX phases Nb_2AsC, Nb_2InC, Mo_2GaC, and Ti_2GeC and also to elucidate the thermodynamic properties at elevated temperature and pressure. In fact, the goal of the present study is to evaluate the ground state crystal energy and from this the equilibrium volume, bulk modulus, elastic constants, band structure, total and partial density of states (DOSs). To describe the bonding nature and to calculate the theoretical Vickers' hardness the Mulliken bond populations are investigated. Further, the shape of the Fermi surface is determined to add the information about the bonding character of the four MAX phase superconductors. All the optical properties e.g., dielectric function, refractive index, extinction coefficient, absorption spectrum, energy loss function, reflectivity and photoconductivity are calculated and analyzed. The thermodynamic properties such as bulk modulus, Debye temperature, specific heats and volumetric thermal expansion coefficient are also calculated and discussed. Finally all properties are compared with available theoretical and experimental data.

1.4 Outline of the thesis

In the present thesis, the background of the work, history of the MAX phases and research objective are discussed in this first chapter. Chapter two describes the crystal structure. As one of the main components of this research, first-principles methodology will be presented in chapter three, titled First-principles methods, while the detailed theory for investigated properties will be given in chapter four. Chapter five will focus on the computational tools used in present study. The results associated with different properties investigated in this research will be presented and discussed in chapter six. Conclusions will be presented in chapter seven along with several possibilities for technological applications.

References:

[1] M.W. Barsoum, "*The $M_{n+1}AX_n$ Phases; Thermodynamically Stable Nanolaminates*", Prog. Solid State Chem. **28** (2001) 201.

[2] M.W. Barsoum and T. El-Raghy, "*Synthesis and Characterization of a remarkable ceramic: Ti_3SiC_2*", J. Am. Ceram. Soc. **79** (1996) 1953.

[3] H.-I. Yoo, M.W. Barsoum, T. El-Raghy, "*Materials science: Ti_3SiC_2 has negligible thermopower*", Nature (London) **407** (2000) 581.

[4] T. El-Raghy, M.W. Barsoum, A. Zavaliangos, S.R. Kalidindi, "*Processing and Mechanical Properties of Ti_3SiC_2: II, Effect of Grain Size and Deformation Temperature*", J. Am. Ceram. Soc. **82** (1999) 2855.

[5] M.W. Barsoum, L. Farber, and T. El-Raghy, "*Dislocations, kink bands, and room-temperature plasticity of Ti_3SiC_2*", Metall. Mater. Trans. A **30** (1999) 1727.

[6] Z.M. Sun, H. Hashimoto, Z.F. Zhang, S.L. Yang, and S. Tada, "*Synthesis and Characterization of a Metallic Ceramic Material-Ti_3SiC_2*", Mater. Trans. **47** (2006) 170.

[7] P. Finkel, M.W. Barsoum, and T. El-Raghy, "*Low temperature dependencies of the elastic properties of Ti_4AlN_3,$Ti_3Al_{1.1}C_{1.8}$, and Ti_3SiC_2*", J. Appl. Phys. **87** (2000) 1701.

[8] M.W. Barsoum, "*Physical properties of the MAX phases*", Encyclopedia of Materials: Science and Technology (Elsevier, Amsterdam, 2009)

[9] M. Radovic, M.W. Barsoum, T. El-Raghy, and S.M. Wiederhorn, "*Tensile creep of coarse-grained Ti_3SiC_2 in the 1000–1200°C temperature range*", J. Alloys and Compds. **361** (2003) 299.

[10] C.J. Gilbert, D.R. Bloyer, M.W. Barsoum, T. El-Raghy, A.P. Tomsia, and R.O. Ritchie, "*Fatigue-crack growth and fracture properties of coarse and fine-grained Ti_3SiC_2*", Scri. Mater. **42** (2000) 761.

[11] M. Sundberg, G. Malmqvist, A. Magnusson, and T. El-Raghy, "*Alumina forming high temperature silicides and carbides*", Ceram. Inter. **30** (2004) 1899.

[12] V.D. Jovic, M.W, Barsoum, B.M. Jovic, S. Gupta, T. El-Raghy, and M.W. Barsoum, "*Corrosion behavior of select MAX phases in NaOH, HCl and H_2SO_4*", Corr. Sci. **48** (2006) 4274.

[13] J.-P. Palmquist, S. Li, P.O.A. Persson, J. Emmerlich, O. Wilhelmsson, H. Högberg, M.I. Katsnelson, B. Johansson, R. Ahuja, O. Eriksson, L. Hultman, and U. Jansson**,** "*$M_{n+1}AX_n$ phases in the Ti-Si-C system studied by thin-film synthesis and ab initio calculations*", Phys. Rev. B **70** (2004) 165401.

[14] Z.J. Lin, M.J. Zhuo, Y.C. Zhou, M.S. Li, and J.Y. Wang, "*Microstructures and Theoretical Bulk Modulus of Layered Ternary Tantalum Aluminum Carbides*", J. Am. Ceram. Soc. **89** (2006) 3765.

[15] J. Zhang, B. Liu, J.Y. Wang, and Y.C. Zhou, "*Low-temperature instability of Ti_2SnC: A combined transmission electron microscopy, differential scanning calorimetry, and x-ray diffraction investigations*", J. Mater. Res. **24** (2009) 39.

[16] L.E. Toth, "*High superconducting transition temperature in the molybdenum carbibe family of compounds*", J. Less comn. Metals, **13** (1967) 129.

[17] K. Sakamaki, H. Wada, H Nozaki, Y. Onuki, and M. Kawai, "*Carbosulfide superconductor*", Solid State Commun., **112** (1999) 323.

[18] A.D. Bortolozo, O.H. Sant'Anna, M.S. da Luz, C.A.M. dos Santos, A.S. Pereira, K.S. Trentin, and A.J.S. Machado, "*Superconductivity in the Nb_2SnC compound*", Solid State Commun. **139** (2006) 57.

[19] S.E. Lofland, J.D. Hettinger, T. Meehan, A. Bryan, P. Finkel, S. Gupta, M.W. Barsoum, and G. Hug, "*Electron-phonon coupling in $M_{n+1}AX_n$-phase carbides*", Phys. Rev. **B 74** (2006) 174501.

[20] A.D. Bortolozo, O.H. Sant'Anna, C.A.M. dos Santos, A.J.S. Machado, "*Superconductivity in the hexagonal-layered nanolaminates Ti_2InC compound*", Solid State Commun. **144** (2007) 419.

[21] A.D. Bortolozo, Z. Fisk, O.H. Sant'Anna, C.A.M. dos Santos, and A.J.S. Machado, "*Superconductivity in Nb_2InC*", Physica **C 469** (2009) 256.

[22] A.D. Bortolozo, G. Serrano, A. Serquis, D. Rodrigues Jr., C.A.M. dos Santos, Z. Fisk, and A.J.S. Machado, "*Superconductivity at 7.3 K in Ti_2InN*", Solid State Commun. **150** (2010) 1364.

[23] A.D. Bortolozo, O.H. Sant'Anna, C.A.M. Dos Santos, and A.J.S. Machado, "*Superconductivity at 9.5 K in the Ti_2GeC compound*", Mater. Science-poland **30** (2012) 92.

[24] M.T. Nasir and A.K.M.A. Islam, "*MAX phases Nb_2AC (A = S, Sn): An ab initio study*," Comp. Mater. Sci. **65** (2012) 365-371.

[25] M. Roknuzzaman and A.K.M.A. Islam, "*Ab Initio Investigation of Nitride in Comparison with Carbide Phase of Superconducting Ti_2InX (X = C, N)*", ISRN Condensed Matter Physics **2013** (2013) 646042.

[26] W. Jeitschko, H. Nowotny, and F. Benesovsky, "*Kohlenstoffhaltige ternare Verbindungen* (*H-phase*)", Monatsh. Chem. **94** (1963) 672.

[27] W. Jeitschko, H. Nowotny, and F. Benesovsky, "*Kohlenstoffhaltige ternare Verbindungen* (*V-Ge-C, Nb-GaC, Ta-Ga-C, Cr-Ga-C und Cr-Ge-C*)", Monatsh. Chem. **94** (1963) 844.

[28] W. Jeitschko, H. Nowotny, and F. Benesovsky, "*Ti_2AlN, eine Stickstoffhaltige H-Phase*", Monatsh. Chem. **94** (1963) 1198.

[29] W. Jeitschko, H. Nowotny, and F. Benesovsky, "*Die H-Phasen: Ti_2InC, Hf_2InC, und Ti_2GeC*", Monatsh. Chem., **94** (1963) 1201.

[30] W. Jeitschko, H. Nowotny, and F. Benesovsky, "*Die H-Phasen: Ti_2CdC, Ti_2GaC, Ti_2GaN, Ti_2InN, Zr_2InN und Nb_2GaC*", Monatsh. Chem. **95** (1964) 178.

[31] W. Jeitschko, H. Nowotny, and F. Benesovsky, "*Die H-Phasen: Ti_2TlC, Ti_2PbC, Nb_2InC, Nb_2SnC, und Ta_2GaC*", Monatsh. Chem. **95** (1964) 431.

[32] W. Jeitschko, H. Holleck, H. Nowotny, and F. Benesovsky, "*Phasen mit Aufgefulltem Ti_2Ni-Typ*", Monatsh. Chem. **95** (1964) 1004.

[33] E. Reiffenstein, H. Nowotny and F. Benesovsky, "*Strukturchemische und magnetochemische Unterstruchungen an Komplacarbiden*", Monatsh. Chem. **97** (1966) 1428.

[34] H. Boller and H. Nowotny, "*Ronthenographische Untersuchungen in System: V-As-C*", Monatsh. Chem. **97** (1966) 1053.

[35] W. Jeitschko and H. Nowotny, "*Die Kristallstuktur von Ti_3SiC_2 – Ein Neuer Komplxcaebid-Typ*", Monatsh. Chem., **98** (1967) 329.

[36] H. Wolfsgruber, H. Nowotny and F. Benesovsky, "*Die Kristallstuktur von Ti_3GeC_2*", Monatsh. Chem., **98** (1967) 2401.

[37] H. Boller and H. Nowotny, "*Die Kristallstruktur von V_2PC und V_5P_3N*", Monatsh. Chem., **99** (1968) 672.

[38] O. Backmann, H. Boller and H. Nowotny, "*Neue H-Phasen*", Monatsh. Chem., **99** (1968) 1580.

[39] O. Beckmann, H. Boller, H. Nowotny and F. Benesovsky, "*Einige Komplex carbide und –nitride in den Systemen Ti-{Zn,Cd,Hg}-{C,N} und Cr-Ga-N*", Monatsh. Chem., **100** (1969) 1465.

[40] H. Nowotny, "*Struktuchemie Einiger Verbindungen der Ubergangsmetalle mit den element C, Si, Ge, Sn*", Prog. Solid State Chem., **5** (1971) 27

[41] H. Nowotny and S. Windisch, *Annual Review Inc*., Palo Alto, CA. **3** (1973) 171.

[42] J.C. Schuster, H. Nowotny and C. Vaccaro, "*The Ternary Systems: Cr-Al-C, V-Al-C and Ti-Al-C and the Behavior of the H-phases (M_2AlC)*", J. Solid State Chem., **32** (1980) 213.

[43] M.A. Pietzka and J.C. Schuster, "*Summary of Constitution Data of the System Al-C-Ti*", J. Phase Equilibria **15** (1994) 392.

[44] M.A. Pietzka and J.C. Schuster, "*The Ternary Boundary Phases of the Quaternary System Ti-Al-C-N*"; in Concerted action on Materials Science, Leuvan Proceedings, Part A, Commission of the European Communities, Brussels, Belgium, 1992.

[45] M.W. Barsoum, L. Farber, I. Levin, A. Procopio, T. El-Raghy, and A. Bermer, "*High-Resolution Transmission Electron Microscopy of Ti_4AlN_3, or $Ti_3Al_2N_2$ Revisited*", J. Amer. Cer. Soc. **82** (1999) 2545.

[46] V.I. Ivchenko, M.I. Lesnaya, V.F. Nemchenko, and T.Y. Kosolapova, "*Preparation and Some Properties of the Ternary Compound Ti_2AlN*", Porosh. Metall. **160** (1976) 60.

[47] V.I. Ivchenko and T.Y. Kosolapova, "*Conditions of Preparation of Ternary Ti-C-Al alloy Powders*", Porosh. Metall., **150** (1975) 1.

[48] V.I. Ivchenko, M.I. Lesnaya, V.F. Nemchenko, and T.Y. Kosolapova, "*Some Physical Properties of Ternay Compounds in the System Ti-Al-C*", Porosh. Metall. **161**(1976) 45.

[49] L.E. Toth, "*Transition Metal Carbides and Nitridies*", Academic Press, New York, 1971.

[50] D.I. Bardos and P. A. Beck, "*Electron Phases in Certain Ternary Alloys of Transition Metals with Silicon*," Trans. Metall. Soc. AIME **236** (1966) 64.

[51] S. Setz, H. Nowotny, and F. Benesovsky, "*Untersuchungen in den Systemen: Mangan-{Vanadin, Rhenium, Eisen}-silicium*", Monatsh. Chem. **99** (1968) 2004.

[52] W. Jeitschko, "*The crystal structure of MoCoB and related compounds*", Acta. Crystallogr. **B24** (1967) 930.

[53] E. Ganglberger, H. Nowotny, F. Benesovsky, "*Neue* G *-Phasen*", Monatsh. Chem. 97 (1966) 829.

[54] G. Hägg, "*Metalliska Nitrider, Karbider, Borider och Hydrider*", Teknisk Tidskrift för Bergsvetenskap **4** (1931) 23.

[55] T. El-Raghy, S. Chakraborty, M.W. Barsoum, "*Synthesis and characterization of Hf_2PbC, Zr_2PbC and M_2SnC (M=Ti, Hf, Nb or Zr)*", J. Eur. Ceram. Soc. **20** (2000) 2619.

2. Crystal structure

This present chapter provides the crystal structure and structural aspects of MAX phases with a special attention on superconducting 211 MAX phases.

2.1 Crystal structure

As defined by Barsoum [1], the MAX phases adopted the chemical formula $M_{n+1}AX_n$ (n = 1, 2, 3), where M is an early transition metal, A is an A-group element comes from column 13 – 16 in the periodic table, and X is C or N, or both. The different MAX stoichiometries are sometimes addressed as 211 (n = 1), 312 (n = 2), and 413 (n = 3) MAX phases. Fig. 2.1(a) represents the hexagonal unit cells of 211, 312, and 413 MAX phases. The number of M-layers separating the A-layers makes the difference between the three structures: in the 211 phases there are two; in the 312 phases three, and in the 413 phases four. The unit cells consisting of M_6X octahedra, e.g. Nb_6C, interleaved with layers of A-elements (e.g. As, In, Ga or Ge). The M_6X edge-sharing octahedral building block in the MAX phases is the same as in the binary carbides and nitrides, MX. In the 312 and 413 MAX structures, there are two different M sites, those adjacent to A, and those not. These sites are mentioned as M(1) and M(2), respectively. In the 413 structure, there are also two nonequivalent X sites, X(1) and X(2). In the MAX phases, the MX layers are twinned with respect to each other and separated by the A-layer which acts as mirror plane. This is illustrated in Fig. 2.1(b), which is a high resolution transmission electron microscopy (TEM) image provided a cross section of the structure of Ti_3SiC_2 [2]. The twinning and resulting characteristic "zig-zag" stacking of the MAX phases is evident. The MAX structure is anisotropic: the lattice parameters are typically around a ~ 3 Å and c ~ 13 Å (for 211 phases), c ~ 18 Å (for 312 phases), and c ~ 23-25 Å (for 413 phases).

MAX phase compounds have nanolaminate structure. In fact, nanolaminates are multilayered thin film structures with nanometer dimensions and very high interfacial density. These multilayer structures can display novel properties, which

can be optimized by manipulating the thickness and composition of the individual nanolayer. Nanolaminates show unique physical properties when the nanolayer thickness is less than the characteristic length scale that defines the physical property. For example, thermal conductivity is reduced when the nanolayer thickness is less than the mean free path of the phonon that transfers the heat. Likewise, hardness is increased when the nanolayer thickness is less than the dislocation length for the slip plane motion that characterizes the response of the material to stress.

In principle, a MAX phase does not necessarily have to be thermodynamically stable. The term "thermodynamically stable nanolaminates" is used to distinguish them from artificial nanolaminates, e.g., superlattice thin films. An equivalent, but more stringent, description to "thermodynamically stable nanolaminates" is to refer to the MAX phases as "inherently nanolaminated" (i.e., they are nanolaminated by nature, not by artificial design). However, that these terms are not restricted to the MAX phases, but include many other phases with a laminated structure.

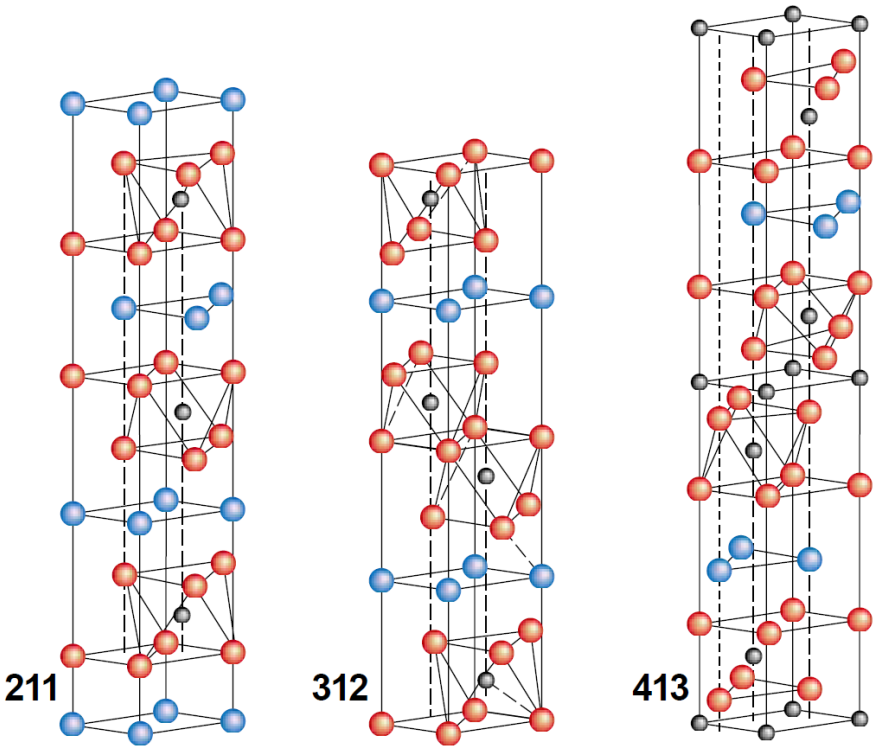

Fig. 2.1(a). Crystal structures of the three MAX groups. Early transition metal atoms are colored in red, A-group elements in blue, carbon or nitrogen in black [2]

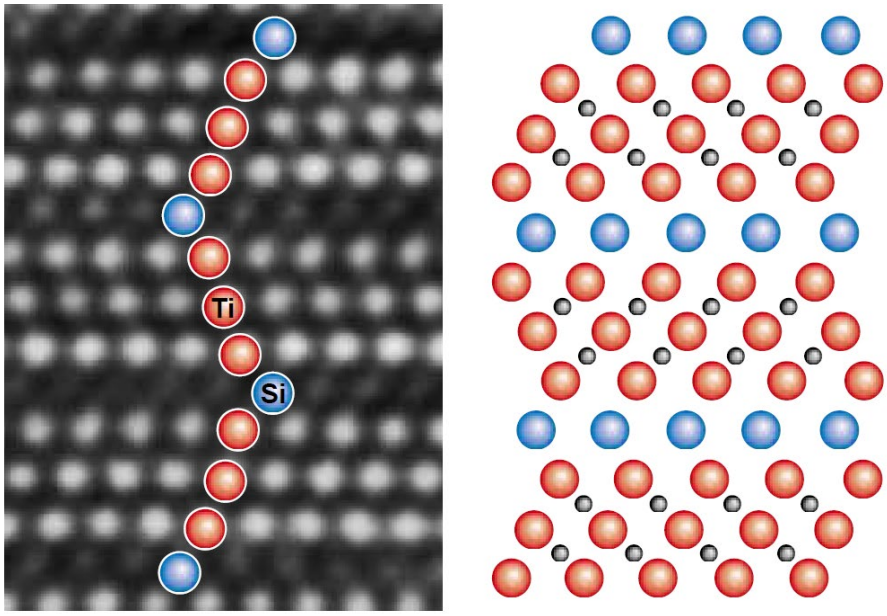

Fig. 2.1(b). The TEM image shows the cross section of the structure of Ti_3SiC_2. Small carbon atoms are not visible in the image (left). Diagram on the right is a micrograph of the same [2].

2.2 Structural aspects

2.2.1 Lattice parameters

A group of lattice constants is referred to as lattice parameters. A lattice constant is a measure of either length or angle that defines the size and shape of the unit cell of a crystal lattice. In fact, the lattice constants refer to the physical dimension of unit cells in a crystal lattice. In general, lattices in three dimensions have three lattice constants, namely, *a*, *b* and *c* that measures the length of the side of unit cell and three angles between the sides, namely, α, β, and γ that also denotes the angles between the vectors '***b*** and ***c***', '***c*** and ***a***', and '***a*** and ***b***', respectively. Actually, a full set of lattice parameters consist of the three lattice constants and the three angles between them. However, in hexagonal crystal structure as in e.g., MAX phases, the *a* and *b* constants are equal, and we only refer to the *a* and *c* constants representing the basal and height parameters respectively, and for this system, the angles are $\alpha = \beta = 90°$ and $\gamma = 120°$. The M-M distances in the MAX phases are strongly correlated with, and almost equal to, the M-M distances in the MX phase [2,3]. As

for the binary MX compounds [4,5], it is useful to consider the MAX compounds to be interstitial compounds in which the A atoms and the X atoms fill the interstitial sites between the M atoms. In such a scheme, the c parameter of the 211 phases- composed of four layers per unit cell-should be ~4 times the a parameter. Similar arguments for 312 and 413 phases, with six and eight M layers per unit cell, respectively, predict ratios of ~6 and ~8. The actual c/a ratios are ~4 in 211 phases, ~5.8 to 6 in the 312 phases, and 7.8 in 413 phases, are consistent with this simple structural notation. The lattice constants for selected 211 MAX phases are given in Table 2.2.1.

Table 2.2.1: Calculated lattice constants of superconducting 211 MAX phases Nb_2AsC, Nb_2InC, Mo_2GaC, and Ti_2GeC.

Phases	*a* (Å)	*c* (Å)	*c/a*
Nb_2AsC	3.324	11.979	3.60
Nb_2InC	3.186	14.526	4.56
Mo_2GaC	3.064	13.178	4.30
Ti_2GeC	3.085	12.961	4.20

2.2.2 Unit cell

The unit cell of the MAX phases are characterized by near closed-packed M layers interleaved with layers of pure A-group element, with the X atoms filling the octahedral sites between the former. The M_6X octahedra are identical to those found in the rock salt structure of the corresponding binary MX carbides. The A-group elements are located at the corners of trigonal prisms, which are slightly larger, and thus better able to accommodate the larger A atoms, than the octahedral sites [6-9]. When n = 1, two M layers separate the A layers. For n = 2, there are three M layers and for n = 3, there are four M layers that separate the A layers. The 312 and 413 MAX phases exist in two polymorphs, α and β. The polymorphism of 413 phases is different than the one observed in the 312 phases, where the difference is in the A-element layers. The difference between α- and β-413 is in the positions of the M(2) and C(2) atoms. Only Ta_4AlC_3 exists in the bulk in the both polymorphs

[10-13], the remaining 413 phases crystallize in the bulk form in the α polymorph [14-16]. The superconducting MAX compounds are the member of 211 phases and these phases have two formula units as well as eight atoms per unit cell.

2.2.3 Crystallography

The MAX phases crystallize in the hexagonal space group D^4_{6h}, with Hermann-Mauguin notation $P6_3/mmc$, No. 194 in the International Tables. The meaning of this nomenclature is as follows:

∗*P* - "Primitive" Bravais lattice, which means there is no additional translational symmetry for the lattice points, and the lattice points are on the cell corners only, *i.e.*, there are no other face-, base-, or body-centered positions. All the hexagonal space groups have a primitive lattice.

∗6_3 - This is the screw-axis (rotational and translational) symmetry, where the "6" refers to 6-fold symmetry and the "3" subscript refers to the distance for translation along the primary axis. For hexagonal systems, the primary direction is [0001] (along the *c* axis). The notation n_r describes a symmetry with a rotation by $2\pi/n$ followed by a translation of a fraction r/n of the unit cell length along the rotation axis [0001] (*i.e.* the *c* lattice parameter). For 6_3, this is rotation by $2\pi/6=\pi/3$ (60˚) around the *c* axis and translation halfway along *c*.

∗*mmc* - The part after the slash refers to mirror and glide plane symmetry perpendicular to the primary, secondary, and tertiary axes. For hexagonal systems, the primary direction is [0001] (along the *c* axis), secondary is [10$\underline{1}$0] (along the *a* axis) and the tertiary is [11$\underline{2}$0] (the bisector of the *a* and *b* axes). The "*mm*" represents mirror symmetry across the (0001) and (10$\underline{1}$0) planes. The "*c*" denotes axial glide plane symmetry perpendicular to the (11$\underline{2}$0) plane, with glide vector *c*/2. Although the full notation is $P6_3/m$ 2/*m* 2/*c*, the number 2 may be omitted due to the fact that a 2-fold symmetry is trivial. Therefore, the shortened symbol is typically used.

The atoms in MAX phases are arranged in alternate nanolaminate layers consisting of close-packed layers of *M* and *X* atoms – where the *X* atoms fill the octahedral sites between *M* layers – interleaved with layers of pure *A* elements. The Wyckoff positions for the atom sites in 211, 312, and 413 structures are listed in Table 2.2.3.

Table 2.2.3: The Wyckoff positions for the atom sites in 211, 312, and 413 MAX Phases

Phases		Space group	Atoms	Wyckoff	x	y	z
211	M_2AX	$P6_3/mmc$	*M*	4*f*	1/3	2/3	$z_M \approx 0.08$
			A	2*d*	1/3	2/3	3/4
			X	2*a*	0	0	0
312	α-M_3AX_2	$P6_3/mmc$	M_1	2*a*	0	0	0
			M_2	4*f*	2/3	1/3	$z_M \approx 0.14$
			A	2*b*	0	0	1/4
			X	4*f*	1/3	2/3	$z_M \approx 0.07$
312	β-M_3AX_2	$P6_3/mmc$	M_1	2*a*	0	0	0
			M_2	4*f*	2/3	1/3	$z_M \approx 0.14$
			A	2*d*	1/3	2/3	3/4
			X	4*f*	1/3	2/3	$z_M \approx 0.07$
413	α-M_4AX_3	$P6_3/mmc$	M_1	4*e*	0	0	$z_M \approx 0.16$
			M_2	4*f*	1/3	2/3	$z_M \approx 0.05$
			A	2*c*	1/3	2/3	1/4
			X_1	4*f*	2/3	1/2	$z_M \approx 0.10$
			X_2	2*a*	0	0	0
413	β-M_4AX_3	$P6_3/mmc$	M_1	4*f*	1/3	2/3	$z_M \approx 0.66$
			M_2	4*f*	1/3	2/3	$z_M \approx 0.05$
			A	2*c*	1/3	2/3	1/4
			X_1	4*e*	0	0	$z_M \approx 0.10$
			X_2	2*a*	0	0	0

References

[1] M.W. Barsoum, "*The $M_{n+1}AX_n$ Phases; Thermodynamically Stable Nanolaminates*", Prog. Solid State Chem. **28** (2001) 201.

[2] M.W. Barsoum and T. El-Raghy, "*The MAX Phases: Unique new Carbides and Nitrides Materials*" Am. Sci. 89 (2001) 334.

[3] H. Nowotny, "*Struktuchemie einiger Verbindungen der Ubergangsmetalle mit den Elementen C, Si, Ge, Sn*", Prog. Solid State Chem. **5** (1971) 27.

[4] H.O. Pierson, "*Hand book of Refractory Carbides and Nitrides*", Westwood, NJ: Noyes, 1996.

[5] A. Cottrell, "*Chemical Bonding in Transition Metal Carbides*", London: Inst. Mater. 1995.

[6] W. Jeitschko, H. Nowotny, and F. Benesovsky, "*Ti_2AlN, eine stickstoffhaltge H-Phase*" Monatsh. Chem. **94** (1963) 1198.

[7] W. Jeitschko, H. Nowotny, and F. Benesovsky, "*Die H-Phasen: Ti_2CdC, Ti_2GaC, Ti_2GaN, Ti_2InN, Zr_2InN und Nb_2GaC*", Monatsh. Chem. **95** (1964) 178.

[8] W. Jeitschko, H. Nowotny, and F. Benesovsky, "*Kohlenstoffhaltige ternare Verbindungen* (*V-Ge-C, Nb-GaC, Ta-Ga-C, Cr-Ga-C und Cr-Ge-C*)" Monatsh. Chem. **94** (1963) 844.

[9] W. Jeitschko, H. Nowotny, and F. Benesovsky, "*Kohlenstoffhaltige ternare Verbindungen* (*H-phase*)", Monatsh. Chem. **94** (1963) 672.

[10] P. Eklund, J.-P. Palmquist, J. Höwing, D.H. Trinh, T. El-Raghy, H. Högberg, L. Hultman, "*Ta_4AlC_3: Phase determination, polymorphism and deformation*", Acta Materialia **55** (2007) 4723.

[11] J. Etzkorn, M. Ade, H. Hillebrecht, "*Ta_3AlC_2 and Ta_4AlC_3: single-crystal investigations of two new ternary carbides of tantalum synthesized by the molten metal technique*", Inorg. Chem. **46** (2007) 1410.

[12] C. Hu, Z. Lin, L. He, Y. Bao, J. Wang, M. Li, and Y. Zhou, "*Physical and mechanical properties of bulk Ta_4AlC_3 ceramic prepared by an in situ reaction synthesis/hot-pressing method*", J. Am. Ceram. Soc. **90** (2007) 2542.

[13] B. Manoun, S.K. Saxena, T. El-Raghy, and M.W. Barsoum. "*High-pressure X-ray study of Ta_4AlC_3*", Appl. Phys. Lett. **88** (2006) 201902.

[14] M.W. Barsoum, L. Farber, I. Levin, A.T. Procopio, T. El-Raghy, A. Berner, "*High-resolution transmission electron microscopy of Ti_4AlN_3, or $Ti_3Al_2N_2$ revisited*", J. Am. Ceram. Soc. **82** (1999) 2545.

[15] C.J. Rawn, M.W. Barsoum, T. El-Raghy, A.T.Procopio, C.M. Hoffman, C.R. Hubbard, "*Structure of $Ti_4AlN_3{-}x$: a layered $M_{n-1}AX_n$ nitride*", Mater. Res. Bull. **35** (2000) 1785.

[16] J. Etzkorn, M. Ade, H. Hillebrecht, "*V_2AlC, V_4AlC_{3-x} (x approximate to 0.31), and $V_{12}Al_3C_8$: synthesis, crystal growth, structure, and superstructure*", Inorg. Chem. **46** (2007) 7646.

3. First-principles methods

Various computational methods are available for materials modeling. One important tool is the use of calculations based on first principles, which are especially useful for materials in the solid state and phenomena that are controlled by properties of materials on the atomic length scale. These calculations are known as "first-principles," or "*ab initio*", calculations, which refer to the fact that they are derived from the first principles of quantum mechanics, with no experimental parameters used in the numerical model. While the central equations of quantum mechanics for many-body system are virtually impossible to solve explicitly, approximations and reformulations can be used to obtain a result that converges to the solution of the Schrödinger equation. One important first-principles method for quantum mechanical modeling that uses functionals of the electron density is known as density functional theory (DFT). This chapter will summarize relevant concepts behind these calculations.

3.1 Many-body problems in quantum mechanics

The field of quantum mechanics makes it possible to describe a many-body system at the atomic level based only on its electronic structure and atomic arrangement, without the need to input any empirical parameters. Here we walk through important topics in quantum mechanics to set the stage for what equations must be solved to describe materials.

3.1.1 Schrödinger's equation

In principle, the properties of a system may be obtained by solving the quantum mechanical wave equation governing the system dynamics. For non-relativistic systems this is simply the Schrödinger equation [1]. The dynamics of a time-independent non-relativistic system are governed by the Schrödinger equation

$$H\Psi = E\Psi, \tag{3.1}$$

where Ψ is the many-electron wave function, E is the system energy and H is the Hamiltonian of the system. For a system of N_e electrons and N_n nuclei, the Hamiltonian can be written as

$$H = -\frac{1}{2}\sum_{i=1}^{N_e}\nabla_i^2 - \sum_{k=1}^{N_n}\frac{1}{2M_k}\nabla_k^2 - \sum_{i\neq k}^{N_eN_n}\frac{Z_k}{|r_i - R_k|}$$

$$+\sum_{i\neq j}^{N_eN_e}\frac{1}{|r_i - r_j|} + \sum_{k\neq l}^{N_nN_n}\frac{Z_kZ_l}{|R_k - R_l|} \qquad (3.2)$$

The first and second terms are the kinetic energies of the electrons and nuclei, respectively. The third term describes the Coulomb attraction between nuclei and electrons. The fourth and fifth terms represent the electron-electron and nucleus-nucleus Coulomb repulsion, respectively. While there is an analytical solution for the hydrogen atom, the main problem with Schrödinger's equation for many-particle systems is that it is not possible, in general, to solve analytically. Approximations must therefore be made.

3.1.2 Born-Oppenheimer approximation

Born-Oppenheimer approximation [2] allows us to separate the nuclear and electronic degrees of motion; the nuclei are of order ~10^3 times more massive than the electrons, and therefore may be considered to be stationary on the electronic timescale. As a result of this, it is possible to neglect the nuclear kinetic energy contribution to the system total energy. Thus the second term in Eq. 3.2 can be set to zero. Since, the motion of the nuclei and electrons can be separated; the electronic and nuclear problems can be solved with independent wave functions. With the nuclei assumed as stationary then the Coulomb interaction between the nuclei is constant. Therefore, the final term can be omitted in solving the Schrödinger equation and added later as a constant to the total energy. This separation of electronic and nuclear problems is known as the Born-Oppenheimer approximation.

Applying the Born-Oppenheimer approximation in Eq. 3.2, the Hamiltonian can now be simplified to:

$$H = -\sum_{i=1}^{N_e} \nabla_i^2 - \sum_{i\neq k}^{N_e N_n} \frac{Z_k}{|r_i - R_k|} + \sum_{i\neq j}^{N_e N_e} \frac{1}{|r_i - r_j|} + \sum_{k\neq l}^{N_n N_n} \frac{Z_k Z_l}{|R_k - R_l|} \tag{3.3}$$

Although Schrödinger's equation is exact within the non-relativistic regime, it is not possible, except for trivially simple cases, to solve it. There are two reasons for this: one mole of a solid contains $N \sim 10^{28}$ electrons; since the many-electron wave function contains $3N$ degrees of freedom, this is simply intractable; further, the electron-electron Coulomb interaction results in the electronic motions being correlated. Consequently the many-body wave function is a complicated mathematical object that incorporates the effects of this correlation, preventing a separation of the electronic degrees of freedom into N single-body problems. Further, the interaction is too strong to be treated as a perturbation. Thus we must search for approximations that render the Schrödinger equation tractable to numerical solution, whilst retaining as much of the key physics as is possible.

3.1.3 Hartree and Hartree-Fock approximations

The simplest method for approximating electron-electron interactions is through the Hartree approximation [3] where the N electron wave function Ψ is replaced by the product of the single-particle orbitals, $\Psi_i(\mathbf{r}_i s_i)$

$$\Psi(\mathbf{r}_1 s_1, \mathbf{r}_2 s_2, \ldots \mathbf{r}_N s_N) = \frac{1}{\sqrt{N}} \Psi_1(\mathbf{r}_1 s_1)\ \Psi_2(\mathbf{r}_2 s_2) \ldots \Psi_N(\mathbf{r}_N s_N) \tag{3.4}$$

However, this does not account for exchange interactions; in order to overcome this, the wave function is used as antisymmetrized product of its component orbitals – the Hartree-Fock [4] wave function, Ψ_{HF}

$$\begin{aligned}\Psi_{HF} = \frac{1}{\sqrt{N!}} [\, &\Psi_1(\mathbf{r}_1 s_1)\, \Psi_2(\mathbf{r}_2 s_2) \ldots \Psi_N(\mathbf{r}_N s_N) \\ &- \Psi_1(\mathbf{r}_2 s_2)\, \Psi_2(\mathbf{r}_1 s_1) \ldots \Psi_N(\mathbf{r}_N s_N)\end{aligned} \tag{3.5}$$

The Hartree-Fock wave function can be represented as an $N \times N$ determinant, as described by Slater [5]:

$$\Psi_{\mathrm{HF}} = \frac{1}{\sqrt{N!}} \begin{vmatrix} \Psi_1(\mathbf{r}_1 s_1) & \Psi_1(\mathbf{r}_2 s_2) & \cdots & \Psi_1(\mathbf{r}_N s_N) \\ \Psi_2(\mathbf{r}_1 s_1) & \Psi_2(\mathbf{r}_2 s_2) & \ldots & \Psi_2(\mathbf{r}_N s_N) \\ \vdots & \vdots & \ddots & \vdots \\ \Psi_N(\mathbf{r}_1 s_1) & \Psi_N(\mathbf{r}_2 s_2) & \ldots & \Psi_N(\mathbf{r}_N s_N) \end{vmatrix} \tag{3.6}$$

which can also be written as:

$$\Psi_{\mathrm{HF}} = \frac{1}{\sqrt{N!}} \det\left[\Psi_1(\mathbf{r}_1 s_1)\, \Psi_2(\mathbf{r}_2 s_2) \ldots \Psi_N(\mathbf{r}_N s_N)\right] \tag{3.7}$$

The Slater determinant and the expected value of the Hamiltonian can be used to evaluate the Hartree-Fock energy E_{HF}. The final term of this is equal to zero when the orbitals are antisymmetric; this is referred to as the exchange energy, E_{X},

$$E_{\mathrm{HF}} = \langle \Psi_{\mathrm{HF}} | H | \Psi_{\mathrm{HF}} \rangle$$

$$= \sum_i^N \int \Psi_i^*(\mathbf{r}) \left(-\frac{1}{2}\nabla^2 + v_{ext}(\mathbf{r}) \right) \Psi_i(\mathbf{r}) d\mathbf{r}$$

$$+ \frac{1}{2} \sum_i^N \sum_j^N \iint \frac{[\Psi_i(\mathbf{r})]^2 [\Psi_i(\mathbf{r}')]^2}{|\mathbf{r} - \mathbf{r}'|} d\mathbf{r} d\mathbf{r}'$$

$$- \frac{1}{2} \sum_i^N \sum_j^N \iint \frac{\Psi_i^*(\mathbf{r})\, \Psi_i(\mathbf{r}')\, \Psi_j^*(\mathbf{r})\, \Psi_j(\mathbf{r}')}{|\mathbf{r} - \mathbf{r}'|} \delta_{sisj} d\mathbf{r} d\mathbf{r}' \tag{3.8}$$

The last term on the right-hand side is the *exchange* term; this looks similar to the direct Coulomb term, but for the exchanged indices. It is a manifestation of the Pauli exclusion principle, and acts so as to separate electrons of the same spin; the consequent depletion of the charge density in the immediate vicinity of a given electron due to this effect is called the *exchange hole*. The exchange term adds considerably to the complexity of these equations.

The Hartree-Fock equations deal with exchange exactly; however, the equations neglect more detailed correlations due to many-body interactions. The effects of electronic correlations are not negligible; indeed the failure of Hartree-Fock theory to successfully incorporate correlation leads to one of its most celebrated failures. The individual contributions to the total energy per electron for the homogeneous electron gas, as a function of Wigner-Seitz radius ($\mathbf{r_s}$) is depicted in Fig. 3.1, from which the momentousness of exchange and correlation contributions to the total energy can be realized. The requirement for a computationally practicable scheme that successfully incorporates the effects of both exchange and correlation leads us to consider the conceptually disarmingly simple and elegant density functional theory.

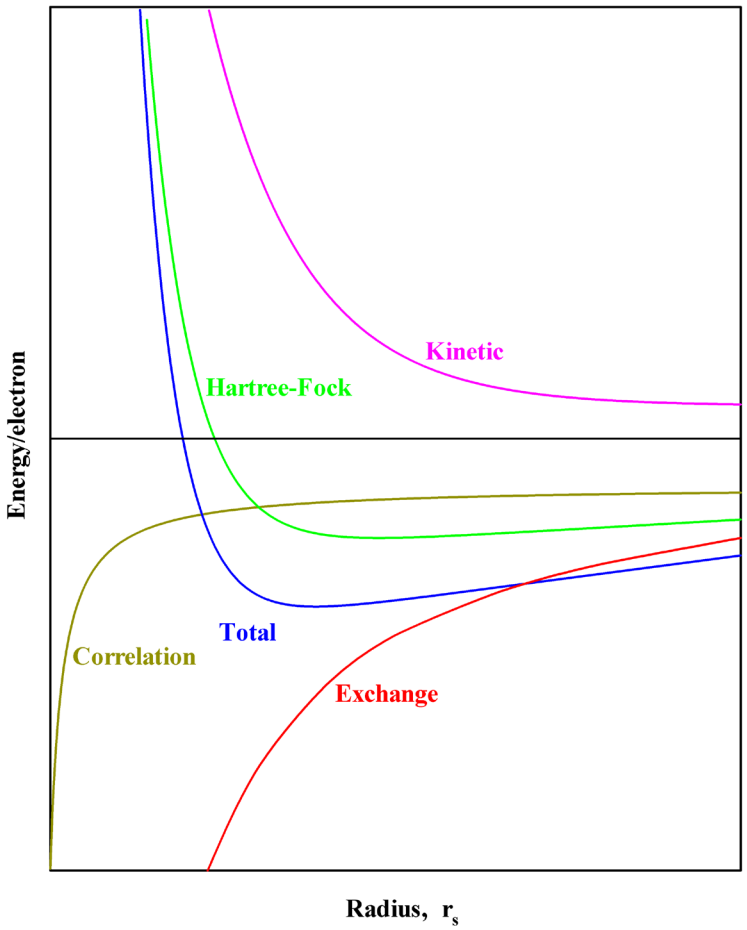

Fig. 3.1. The contributions to the total energy per electron as a function of the Wigner-Seitz radius.

3.2 Density functional theory

Density Functional Theory (DFT) is one of the most widely used method for first-principles calculations of the ground state electronic structure of many-body systems in particular atoms, molecules, crystals, surfaces, and the condensed phases. The DFT determines the properties of a many-body system using functional i.e., function of another function, which, in this case, is the spatially dependent electron density. Hence the name density functional theory comes from the use of functional of the electron density.

The DFT treats the electron density as the central variable rather than the many-body wave function. This conceptual difference leads to a remarkable reduction in difficulty: the density is a function of three variables, *i.e.* the three Cartesian directions, rather than $3N$ variables as the full many-body wave function is. An early density functional theory was proposed by Thomas and Fermi [6,7]. This took the kinetic energy to be a functional of the electron density, but in common with the Hartree and Hartree-Fock methods, only incorporated electron-electron interactions via a mean field potential: as such it neglected *both* exchange and correlation; a subsequent proposal by Dirac [8], formulating an expression for the exchange energy in terms of the electron density failed to significantly improve the method. Here we consider the Hohenberg-Kohn-Sham formulation of DFT; this technique is one of the choice state-of-the-art methods routinely applied in electronic structure theory, and has enjoyed success in fields ranging from quantum chemistry and condensed matter physics to geophysics. DFT is formulated quantum mechanically based on the remarkable and deceptively simple Thomas-Fermi model and two Hohenberg-Khon theorems implemented in Khon-Sham equations.

3.2.1 Thomas-Fermi model

One of the earliest tractable schemes for solving the many-electron problem was proposed by Thomas and Fermi [6,7]. In this model the electron density, $\rho(\mathbf{r})$, is

the central variable rather than the wave function, and the total energy of a system is written as a functional $E\,[\rho(\mathbf{r})]$, where square brackets are used to enclose the argument of the functional, which in this case is the density. The Thomas-Fermi energy functional is composed of three terms,

$$E[\rho(\mathbf{r})] = A_k \int \rho(\mathbf{r})^{5/3} d\mathbf{r} + \int \rho(\mathbf{r}) v_{\text{ext}}(\mathbf{r}) d\mathbf{r} + \frac{1}{2} \iint \frac{\rho(\mathbf{r})\rho(\mathbf{r}')}{|\mathbf{r} - \mathbf{r}'|} d\mathbf{r} d\mathbf{r}' \qquad (3.9)$$

The first term is the electronic kinetic energy associated with a system of non-interacting electrons in a homogeneous electron gas. This form is obtained by integrating the kinetic energy density of a homogeneous electron gas $T_o[\rho(\mathbf{r})]$ [9,10],

$$T[\rho(\mathbf{r})] = \int T_o[\rho(\mathbf{r})]\, d\mathbf{r}, \qquad (3.10)$$

where $T_o[\rho(\mathbf{r})]$ is obtained by summing all of the free-electron energy states $\varepsilon = k^2/2$, up to the Fermi wave vector $k_F = [3\pi^2\rho(\mathbf{r})]^{1/3}$,

$$T_o[\rho(\mathbf{r})] = \frac{2}{(2\pi)^3} \int \frac{k^2}{2} n_k dk = \frac{1}{2\pi^2} \int_0^{k_F} k^4 dk, \qquad (3.11)$$

n_k is the density of allowed states in reciprocal-space. This leads to the form given in (3.9) with coefficient $A_k = \frac{3}{10}(3\pi^2)^{2/3}$. The power-law dependence on the density can also be established on dimensional grounds [11]. The second term is the classical electrostatic energy of attraction between the nuclei and the electrons, where $v_{\text{ext}}(\mathbf{r})$ is the static Coulomb potential arising from the nuclei,

$$v_{\text{ext}}(\mathbf{r}) = -\sum_{j=1}^{M} \frac{Z_j}{|\mathbf{r} - \mathbf{R}_j|} \qquad (3.12)$$

Finally, the third term in (3.9) represents the electron-electron interactions of the system, and in this case is approximated by the classical Coulomb repulsion

between electrons, known as the Hartree energy which does not take into account of quantum phenomenon such as the exchange interaction.

To obtain the ground state density and energy of a system, the Thomas-Fermi equation (3.9) must be minimized subject to the constraint that the number of electrons is conserved.

3.2.2 Hohenberg-Khon theorems

The Hohenberg-Kohn (HK) theorems [12] relate to any system consisting of electrons moving under the influence of an external potential $v_{ext}(\mathbf{r})$. Stated simply they are as follows:

Theorem 1: *The electron density uniquely determines the external potential of many body systems and thus the Hamiltonian and hence all the ground state properties are functionals of the electron density.*

The many-body Hamiltonian H fixes the ground state of the system under consideration *i.e.* it determines the ground state many-body wave function Ψ, and thus the above theorem ensures that this itself is also a unique functional of the ground state density. Consequently, the kinetic and electron-electron interaction energies will also be functionals of electron density $\rho(\mathbf{r})$. One may therefore define the functional $F[\rho(\mathbf{r})]$

$$F[\rho(\mathbf{r})] = T[\rho(\mathbf{r})] + V_{ee}[\rho(\mathbf{r})] \tag{3.13}$$

where T is the kinetic energy operator, and V_{ee} is the electron-electron interaction operator. This functional F is a universal functional in the sense that it has the same dependence on the electron density for any system, independent of the external potential concerned. The exact density dependence of this functional is, however, unknown. Using this functional, the energy functional $E[\rho(\mathbf{r})]$ that alluded to in the first Hohenberg-Kohn theorem can be written in terms of external potential $v_{ext}(\mathbf{r})$ in the following way,

$$E[\rho(\mathbf{r})] = F[\rho(\mathbf{r})] + \int \rho(\mathbf{r}) v_{\text{ext}}(\mathbf{r}) d\mathbf{r} \tag{3.14}$$

Correspondingly, a Hamiltonian for the many-body system can be written such that the electron wave function Ψ that minimizes the expectation value gives the ground state energy (assuming a non-degenerate ground state),

$$E[\rho(\mathbf{r})] = \langle \Psi | H | \Psi \rangle \tag{3.15}$$

The Hamiltonian can be written as,

$$H = F + V_{\text{ext}} \tag{3.16}$$

where V_{ext} is the operator corresponding to the external potential $v_{\text{ext}}(\mathbf{r})$.

***Proof*:** The proof of the first theorem is remarkably simple and proceeds by *reductio ad absurdum*. Assume that there are two potentials $v_1(\mathbf{r})$ and $v_2(\mathbf{r})$ that differ by more than an additive constant and further that these two potentials lead to different ground state wave functions $\Psi_1(\mathbf{r})$ and $\Psi_2(\mathbf{r})$ as well as the Hamiltonians H_1 and H_2. Now assume that these both lead to the same ground state density $\rho_o(\mathbf{r})$. The variational principle then asserts that

$$\begin{aligned} E_1 \leq \langle \Psi_2 | H_1 | \Psi_2 \rangle &= \langle \Psi_2 | H_2 | \Psi_2 \rangle + \langle \Psi_2 | H_1 - H_2 | \Psi_2 \rangle \\ &= E_2 + \int \rho_o(\mathbf{r}) [v_1(\mathbf{r}) - v_2(\mathbf{r})] d\mathbf{r} \end{aligned} \tag{3.17}$$

where E_1 and E_2 are the ground state energies of H_1 and H_2 respectively. Note that this inequality applies only to the ground state and that DFT, as a result, is only rigorously applicable to the ground state. Interchanging 1 and 2 gives a similar expression, and adding the two inequalities leads to

$$E_1 + E_2 \leq E_2 + E_1 \,, \tag{3.18}$$

which is a contradiction, and as a result the ground state density uniquely determines the external potential $v_{\text{ext}}(\mathbf{r})$, to within an additive constant.

Thus theorem 1 is proved.

Theorem 2: *The ground state energy can be obtained variationally: the density that minimizes the total energy is the exact ground state density.*

Proof: The proof of the second theorem is also straightforward: as just shown, the ground state density $\rho_o(\mathbf{r})$ determines the external potential $v_{\text{ext}}(\mathbf{r})$ and $v_{\text{ext}}(\mathbf{r})$ determines H and therefore Ψ. This ultimately means Ψ is a functional of $\rho_o(\mathbf{r})$, and so the expectation value of F is also a functional of $\rho_o(\mathbf{r})$, i.e.

$$F[\rho_o(\mathbf{r})] = \langle \Psi | F | \Psi \rangle \tag{3.19}$$

A density that is the ground state of some external potential of a system is known as v-representable. Following from this, a v-representable energy functional $E_v[\rho_o(\mathbf{r})]$ can be defined in which the external potential $v_{\text{ext}}(\mathbf{r})$of the system is unrelated to another density $\boldsymbol{\rho}'$,

$$E_v[\rho_o(\mathbf{r})] = \int \rho'(\mathbf{r}) v_{\text{ext}}(\mathbf{r}) d\mathbf{r} + F[\rho'(\mathbf{r})]\,, \tag{3.20}$$

and the variational principle asserts,

$$\langle \Psi' | F | \Psi' \rangle + \langle \Psi' | V_{\text{ext}} | \Psi' \rangle > \langle \Psi | F | \Psi \rangle + \langle \Psi | V_{\text{ext}} | \Psi \rangle \tag{3.21}$$

where Ψ is the wave function associated with the correct $\rho_o(\mathbf{r})$. This leads to,

$$\int \rho'(\mathbf{r}) v_{\text{ext}}(\mathbf{r}) d\mathbf{r} + F[\rho'(\mathbf{r})] > \int \rho_o(\mathbf{r}) v_{\text{ext}}(\mathbf{r}) d\mathbf{r} + F[\,\rho_o(\mathbf{r})]\,, \tag{3.22}$$

and so the variational principle of the second HK theorem is obtained,

$$E_v[\rho'(\mathbf{r})] > E_v[\rho_o(\mathbf{r})] \tag{3.23}$$

Although these two theorems prove the existence of a universal functional, they do not give any idea as to the nature of the functional, or how to actually calculate the ground state density. In order to do so, the Kohn-Sham formulation comes in.

3.2.3 Khon-Sham formulation

Kohn and Sham [13] derived a coupled set of differential equations enabling the ground state density $\rho_o(\mathrm{r})$ to be found. Kohn and Sham separated $F\ [\rho_o(\mathrm{r})]$ into four distinct parts including self-interaction Hartree term (second term), so that the energy functional E becomes

$$E\ [\rho(\mathbf{r})] = T_s[\rho(\mathbf{r})] + \frac{1}{2}\iint \frac{\rho(\mathbf{r})\rho(\mathbf{r}')}{|\mathbf{r}-\mathbf{r}'|} d\mathbf{r}d\mathbf{r}' + \int \rho(\mathbf{r})V_{\text{ext}}(\mathbf{r})d\mathbf{r} + E_n$$
$$+E_{XC}[\rho(\mathbf{r})] \tag{3.24}$$

This takes its minimum at the ground state electron density $\rho_o(\mathbf{r})$. The functional consists of the corresponding parts of the Hamiltonian operator plus an additional exchange correlation term E_{XC} that accounts for quantum mechanical corrections. The latter is not exactly known, though fairly good approximations exist. In order to attain an expression for the kinetic energy, Khon and Sham introduced the electron density and the kinetic energy of a non-interacting quantum mechanical system, described by a single Slater determinant with single electron orbitals $\Psi_i(\mathbf{r})$, is

$$T_s[\rho(\mathbf{r})] = \sum_{i=1}^{N} \Psi_i^*(\mathbf{r}) \left(-\frac{1}{2}\nabla^2\right) \Psi_i(\mathbf{r}) d\mathbf{r} \tag{3.25}$$

The variation of the energy functional with respect to the orbitals $\Psi_i(\mathbf{r})$ leads to the Khon-Sham equations

$$\left[-\frac{1}{2}\nabla_i^2 + V_{\text{eff}}(\mathbf{r})\right] \Psi_i(\mathbf{r}) = E_i\, \Psi_i(\mathbf{r}) \tag{3.26}$$

which represents a Schrödinger equation for single electron orbitals $\Psi_i(\mathbf{r})$, where the ground state electron density $\rho_o(\mathrm{r})$ is calculated from the orbitals as

$$\rho_o(\mathbf{r}) = \sum_i |\Psi_i(\mathbf{r})|^2 \tag{3.27}$$

In the Khon-Sham equations the effective potential V_{eff} known as Khon-Sham potential accounts for the interactions between the electrons only in an average way through the electrostatic potential build by all electrons and the nuclei,

$$V_{\text{eff}}(\mathbf{r}) = V_{XC}(\rho, \mathbf{r}) + V_{\text{ext}}(\mathbf{r}) + \int \frac{\rho(\mathbf{r}')}{|\mathbf{r} - \mathbf{r}'|} d\mathbf{r}' \tag{3.28}$$

The set of Khon-Sham equations should be solved self-consistently as

$$V_{\text{eff}}(\mathbf{r}) = V_{\text{eff}}[\rho(\mathbf{r})] \tag{3.29}$$

The Kohn-Sham formulation thus succeeds in transforming the N-body problem into N single-body problems, each coupled via the Kohn-Sham effective potential. As V_{eff} $(\mathbf{r})$ contains the electron density; the eigenvalue problem is nonlinear and must therefore be solved iteratively, which is done in the self-consisting field algorithm outlined in Fig. 3.2.

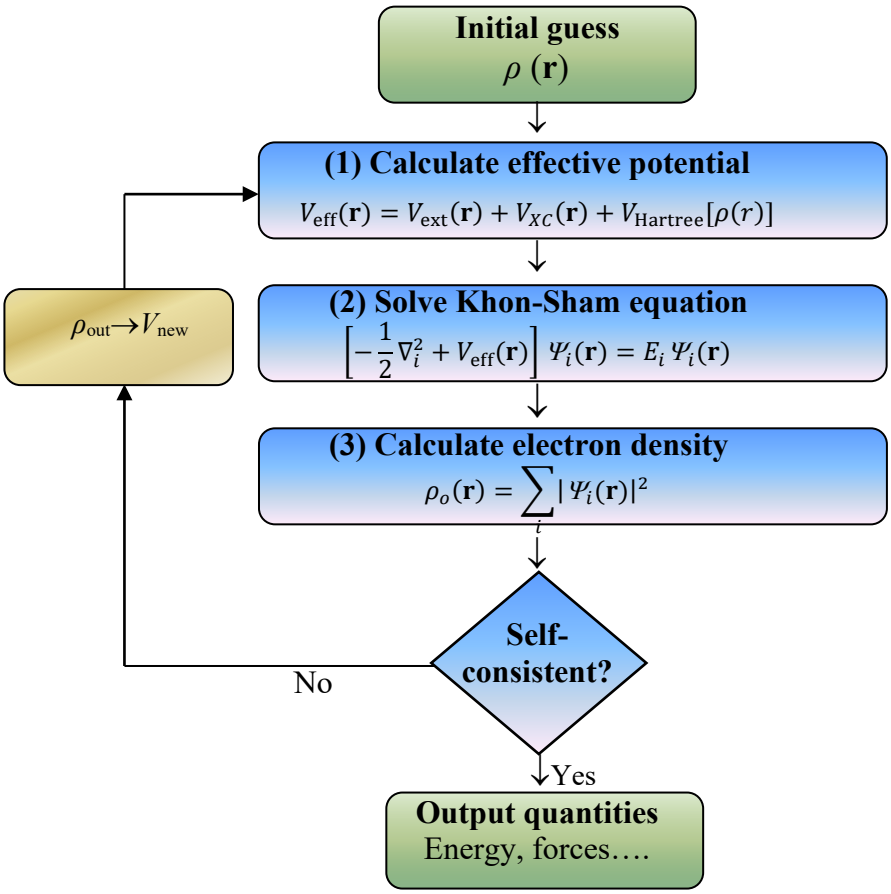

Fig. 3.2. Self-consistent field algorithm for solving the Khon-Sham equations.

The iteration scheme for the Kohn-Sham equations is summarized in the flow chart in Fig. 3.2. The most computationally intensive step is solving the Kohn-Sham equation for a given potential, step (2) in the loop. In this step, the equations are uniquely solved with a given V_{in}, for an output density, ρ_{out}.

After achieving convergence in the self-consistent loop of Fig. 3.2, subsequent iteration schemes can be used to minimize the energy further – for instance, by moving the atomic positions or adjusting the cell volume. The Kohn-Sham equations are indeed much easier to solve than the equations for many-particle interacting systems. However, the major caveat to this technique is that we do not know the form of the exchange-correlation functional. It turns out that this can be approximated reasonably well.

3.2.4 Exchange-correlation functional

The Kohn-Sham equations in 3.26 are thus far exact: no approximations have yet been made; we have simply mapped the fully interacting system onto an auxiliary non-interacting system that yields the same ground state density.

It is mentioned that the Kohn-Sham kinetic energy is not the true kinetic energy; we may use this to define formally the exchange-correlation energy as

$$E_{\text{XC}}[\rho(\mathbf{r})] = (T[\rho(\mathbf{r})] - T_{\text{s}}[\rho(\mathbf{r})]) + (V_{\text{ee}}[\rho(\mathbf{r})] - V_{\text{Hartree}}[\rho(\mathbf{r})]) \tag{3.30}$$

where T and V_{ee} are the exact kinetic and electron-electron interaction energies respectively. Physically, this term can be interpreted as containing the contributions of detailed correlation and exchange to the system energy. Basically exchange-correlation part comes from our attempt to map one N-body quantum mechanical (QM) problem onto N single-body QM problems. Simply, the exchange-correlation energy is defined as the sum of the error made in using a non-interacting kinetic energy and the error made in treating the electron-electron interaction classically. The definition above is such that it ensures that the Kohn-Sham formulation is exact. However, the actual form of E_{XC} is not known except for the free electron

gas; thus we must introduce approximate functionals based upon the electron density to describe this term. There is a zoo of approximations: Local-density approximation (LDA), Local spin-density approximation (LSDA), Generalized gradient approximation (GGA), Meta-GGA, and so on. But LDA and GGA are two common approximations (in various forms) in use frequently.

Local density approximation (LDA)

The LDA [9] ignores corrections to the exchange-correlation (XC) energy due to inhomogeneities in the electron density about **r**. It may seem surprising that this is as successful as it is given the severe nature of the approximation in use; to large extent, it appears [14] that this is due to the fact that the LDA respects the sum rule, which states that exactly one electron is excluded from the immediate vicinity of a given electron at point **r**.

Many approaches can yield local approximations to the XC energy. However, overwhelmingly successful local approximations are those that have been derived from the homogeneous electron gas (HEG) model. In this regard, LDA is generally synonymous with functionals based on the HEG approximation, which are then applied to realistic systems (molecules and solids).

In this approach a real inhomogeneous system is divided into infinitesimal volumes, and the electron density in each of the volumes is taken to be constant. Exchange-correlation energy for the density within each volume is then assumed to be the exchange-correlation energy obtained from the uniform electron gas for that density. Thus, the total exchange-correlation energy of the spin-unpolarized system can be written as

$$E_{\mathrm{XC}}^{\mathrm{LDA}}[\rho(\mathbf{r})] = \int \rho(\mathbf{r})\varepsilon_{XC}[\rho(\mathbf{r})]d\mathbf{r} \tag{3.31}$$

where ρ is the electronic density and ε_{XC} the exchange-correlation energy density, is a function of the density alone. The exchange-correlation energy is decomposed into exchange and correlation terms linearly,

$$E_{XC}^{\mathrm{LDA}} = E_X^{\mathrm{LDA}} + E_C^{\mathrm{LDA}} \tag{3.32}$$

so that separate expressions for $E_{\mathrm{X}}^{\mathrm{LDA}}$ and E_C^{LDA} are sought. The exchange term takes on a simple analytic form for the homogeneous electron gas. Only limiting expressions for the correlation density are known exactly, leading to numerous different approximations for ε_C.

Exchange functional

The exchange-energy density of a HEG is known analytically. The LDA for exchange employs this expression under the approximation that the exchange-energy in a system where the density is not homogeneous, is obtained by applying the HEG results point wise, yielding the expression

$$E_X^{\mathrm{LDA}}[\rho(\mathbf{r})] = -\frac{3}{4}\left(\frac{3}{\pi}\right)^{1/3} \int \rho(\mathbf{r})^{4/3} d\mathbf{r} \tag{3.33}$$

Correlation functional

Analytic expressions for the correlation energy of the HEG are not known except in the high- and low-density limits corresponding to infinitely-weak and infinitely-strong correlation. For a HEG with density ρ, the high-density limit of correlation energy density is

$$\varepsilon_C = A \ln(r_s) + B + r_s[C \ln(r_s) + D], \tag{3.34}$$

and the low limit

$$\varepsilon_C = \frac{1}{2}\left(\frac{g_o}{r_s} + \frac{g_1}{r_s} + \cdots\right), \tag{3.35}$$

where the Wigner-Seitz radius is related to the density as

$$\frac{4}{3}\pi r_s^3 = \frac{1}{\rho} \tag{3.36}$$

Accurate quantum Monte Carlo simulations for the energy of the HEG have been performed for several intermediate values of the density, in turn providing accurate values of the correlation energy density. The most popular LDA's to the correlation

energy density interpolate these accurate values obtained from simulation while reproducing the exactly known limiting behavior. Various approaches, using the different analytic forms for ε_c, have generated several LDA's for the correlation functional, including Vosko-Wilk-Nusair (VWN), Perdew-Zunger (PZ81), Cole-Perdew (CP), and Perdew-Wang (PW92) functionals.

Predating these, and even the formal foundations of DFT itself, is the Wigner correlation functional obtained perturbatively from the HEG model.

Local-spin-density approximation (LSDA)

The extension of density functionals to spin-polarized systems is straightforward for exchange, where the exact spin-scaling is known, but for correlation further approximations must be employed. A spin polarized system in DFT employs two spin-densities, $\rho\uparrow$ and $\rho\downarrow$ with $\rho = \rho\uparrow + \rho\downarrow$, and the form of the local-spin-density approximation (LSDA) is

$$E_{\mathrm{XC}}^{\mathrm{LSDA}}[\rho_\uparrow, \rho_\downarrow] = \int \rho(\mathbf{r})\varepsilon_{XC}[\rho_\uparrow, \rho_\downarrow]d\mathbf{r} \tag{3.37}$$

For exchange energy, the exact result is known in terms of spin-unpolarized functional

$$E_X[\rho_\uparrow, \rho_\downarrow] = \frac{1}{2}(E_X[2\rho_\uparrow] + E_X[2\rho_\downarrow]) \tag{3.38}$$

The spin-dependence of the correlation energy density is approached by introducing the relative spin-polarization:

$$\zeta(\mathbf{r}) = \frac{\rho_\uparrow(\mathrm{r}) - \rho_\downarrow(\mathbf{r})}{\rho_\uparrow(\mathbf{r}) + \rho_\downarrow(\mathbf{r})} \tag{3.39}$$

ζ = 0 corresponds to the paramagnetic spin-unpolarized situation with equal α and β spin densities whereas $\zeta = \pm 1$ corresponds to the ferromagnetic situation where one spin density vanishes. The spin correlation energy density for a given values of the total density and relative polarization, $\varepsilon_c(\rho,\varsigma)$, is constructed so to interpolate the extreme values. Several forms have been developed in conjunction with LDA correlation functionals [15,16].

Generalized gradient approximation (GGA)

The generalized gradient approximation (GGA) attempts to incorporate the effects of inhomogeneities by including the gradient of the electron density; as such it is a semi-local method. The GGA XC functional can be written as

$$E_{XC}^{GGA}[\rho_\uparrow, \rho_\downarrow] = \int f\,(\rho_\uparrow, \rho_\downarrow, \nabla\rho_\uparrow, \nabla\rho_\downarrow) d\mathbf{r}\,, \tag{3.40}$$

where f is known as the enhancement factor. Unlike the LDA, there is no unique form for the GGA, and indeed many possible variations are possible [17-20], each corresponding to a different enhancement factor. The GGA succeeds in reducing the effects of LDA over binding [21], and is significantly more successful when applied to molecules.

The GGA XC functional developed by Perdew-Burke-Ernzerhof [20] known as GGA-PBE leads to a reasonable description of a wide variety of properties of molecules and solids. It has become one of the most heavily used approximations in electronic structure calculations. However, several modifications have been proposed, all with the objective of improving the calculated values of various sets of properties. In the present work, the PBE-GGA is used.

3.3 Bloch's Theorem and Plane Wave Basis Sets

The correlated nature of the electrons within a solid is not the only obstacle to solving the Schrödinger equation for a condensed matter system: for solids, one must also bear in mind the effectively infinite number of electrons within the solid. Essentially, there are two difficulties to overcome: a wave function has to be calculated for each of the infinite number of electrons which will extend over the entire space of the solid and the basis set in which the wave function will be expressed will be infinite.

One may appeal to Bloch's theorem [22] in order to make headway in obviating this problem. Bloch's theorem uses the periodicity of a crystal to reduce the infinite number of one-electron wave functions to be calculated to simply the

number of electrons within the unit cell of the crystal (or half that number if the electronic orbitals are assumed to be doubly occupied - that is, spin degenerate).

The ions in a perfect crystal are arranged in a regular periodic way. Therefore, the external potential felt by the electrons will also be periodic - the period being the same as the length of the unit cell, **l**. That is, the external potential on an electron at **r** can be expressed as $V(\mathbf{r}) = V(\mathbf{r} + \mathbf{l})$. This is the requirement for the use of Bloch's theorem. By the use of this theorem, it is possible to express the wave function of the infinite crystal in terms of wave functions at reciprocal space vectors of a Bravais lattice.

According to Bloch's theorem the wave function of an electron within a perfectly periodic potential may be written as

$$\Psi_{j,\mathbf{k}} = u_j(\mathbf{r})e^{i\mathbf{k}.\mathbf{r}} \tag{3.41}$$

where $u_j(\mathbf{r})$ is a function that possesses the periodicity of the potential, *i.e.* $u_j(\mathbf{r} + \mathbf{l}) = u_j(\mathbf{r})$, where **l** is the length of the unit cell. In 3.41 *j* is the band index, and **k** is a wave vector confined to the first Brillouin Zone. Since $u_j(\mathbf{r})$ is a periodic function, this can be expressed by expanding it into a finite number of plane waves whose wave vectors are reciprocal lattice vectors of the crystal

$$u_j(\mathbf{r}) = \sum_{\mathbf{G}} c_{j,\mathbf{G}} e^{i\mathbf{G}.\mathbf{r}} \tag{3.42}$$

where the **G** are reciprocal lattice vectors defined through **G**.**R** = 2π*m*, with *m* is an integer, **R** is a real space lattice vector and the $c_{j,\mathbf{G}}$ are plane wave expansion coefficients. The electron wave functions may therefore be written as a linear combination of plane waves:

$$\Psi_{j,\mathbf{k}}(r) = \sum_{\mathbf{G}} c_{j,\mathbf{k}+\mathbf{G}} e^{i(\mathbf{k}+\mathbf{G}).\mathbf{r}} \tag{3.43}$$

Given that each electron occupies a state of definite **k**, the infinite number of electrons within the solid gives rise to an infinite number of k-points. At each k-

point, only a finite number of the available energy levels will be occupied. Thus one only needs to consider a finite number of electrons at an infinite number of k-points. This may seem to be replacing one infinity (number of electrons) with another one (number of k-points) to little discernible advantage. However, one does not need to consider all of these k-points; rather, since the electron wave functions will be almost identical for values of **k** that are sufficiently close, one can represent the wave functions over a region of reciprocal space by considering the wave function at a single k-point. It is therefore sufficient to consider the electronic states at a finite number of k-points in order to determine the ground state density of the solid. The net effect of Bloch's Theorem therefore has been to change the problem of an infinite number of electrons to one of considering only the number of electrons in the unit cell (or half that number, depending on whether the states are spin-degenerate or not) at a finite number of k-points chosen so as to appropriately sample the Brillouin Zone.

3.4 Kohn-Sham Equations in Plane Wave Form

Exploiting the lattice periodicity using Bloch's theorem has now led to the one-electron wave functions being expressed in terms of a Fourier expansion using plane waves as a basis set. Although plane waves are not the only possible basis set that can be used, for example, one could use atomic wave functions as a basis set, plane waves are perhaps more aesthetically appealing. More importantly, a plane wave basis set has the advantage of being mathematically simple, and is in principle complete, that is, it completely spans the Hilbert space. This is in contrast to localized basis sets. Plane waves also possess the advantage of covering all space equally, and are thus not biased to any particular region. This is particularly important when one does not have any a priori knowledge of the form of the electronic wave functions. However, it is a double-edged sword in that it results in regions devoid of electron density having equal quality of coverage as regions of high electron density. It is thus, in a sense, inefficient, and it is this that leads to the cubic scaling of plane wave DFT calculations with system size

[23,24]. Accordingly, most efforts at achieving methods that scale linearly with system size have concentrated upon localized basis sets [25-27].

In principle, the series in 3.43 should be infinite; in practice, the series should be truncated in order that it may be handled computationally. The coefficients for the plane waves have a kinetic energy $\frac{\hbar^2}{2m}|\mathbf{k}+\mathbf{G}|^2$, and plane waves with high kinetic energy typically are less important than those of low kinetic energy. One may thus introduce a kinetic energy cut-off $\boldsymbol{E_{cut}}$ in order to achieve a finite basis set. The kinetic energy cut-off is defined through

$$\boldsymbol{E_{cut}} = \frac{\hbar^2}{2m}|\mathbf{k}+\mathbf{G}|^2 \tag{3.44}$$

and thus this fixes the highest reciprocal lattice vector **G** used in the plane wave expansion, resulting in a finite basis set. Expansion of the electron wave functions in terms of plane waves allows the Kohn-Sham equations to take on the particularly simple and appealing form

$$\sum_{\mathbf{G}'}\left|\frac{1}{2}|\mathbf{k}+\mathbf{G}|^2\delta_{\mathbf{G}\mathbf{G}'} + V_{ion}(\mathbf{G}-\mathbf{G}')V_{XC}(\mathbf{G}-\mathbf{G}') + V_H(\mathbf{G}-\mathbf{G}')\right| \times$$

$$c_{i,\mathbf{k}+\mathbf{G}'} = \varepsilon_i c_{i,\mathbf{k}+\mathbf{G}}\,, \tag{3.45}$$

which may be readily shown by substitution of 3.43 into 3.26. One can see that the reciprocal space representation of the kinetic energy is diagonal, whilst the potentials are described in terms of Fourier components. In principle, this secular equation could be solved by simply diagonalising the Hamiltonian matrix $\boldsymbol{H_{\mathbf{k}+\mathbf{G},\mathbf{k}+\mathbf{G}'}}$ whose matrix elements are given by the terms in brackets above. However, the size of the matrix is determined by the choice of cut-off energy$\boldsymbol{E_{cut}}$, and for systems containing valence and core electrons will be intractably large.

3.5 k-point Sampling

It has been already discussed how Bloch's theorem allows one to only consider the electrons within the unit cell at an infinite number of k-points within the first Brillouin zone. As alluded to, it is possible to use only a finite number of k-points if these are chosen so as to appropriately sample the reciprocal space.

Electronic states are allowed only at a set of k-points determined by the boundary conditions that apply to the bulk solid. The infinite number of electrons in periodic solid is accounted for by an infinite number of k-points. The occupied states at each k-point contribute to the electronic potential, so that in principle an infinite number of calculations are needed. However, the electronic wave functions at k-points that are very close together will be almost identical. This suggests the DFT expressions contain a sum over k-points (or, equivalently, an integral over the Brillouin zone) can be efficiently evaluated using a numerical scheme that performs summation over a small number of special points in the Brillouin zone. In addition, symmetry considerations suggest that only k-points within the irreducible segment of the Brillouin zone should be taken into account. A number of prescriptions exist for generating such points and corresponding weights to be used in the summation [14,28]. Using these methods, one can obtain an accurate approximation of the electronic potential and the total energy of an insulator by calculating electronic states at a very small number of k-points. The calculations for metallic systems require a more dense set of k-points to determine the Fermi level accurately.

The magnitude of any error in the total energy due to limited k-point sampling can always be reduced by using a denser set of k-points; in much the same way as the convergence with respect to the number of basis set functions is achieved. It is important to achieve high convergence with respect to the k-point sampling when the energies of two systems with different symmetries are compared, for example if one is looking at the relative stabilities of a FCC and an HCP structure. There is no cancellation of errors in this case and both energies have to be absolutely converged.

One of the most popular schemes for generating k-points was proposed by Monkhorst and Pack [29]. This scheme, which was later modified to include hexagonal systems [30], produces a uniform grid of k-points along the three axes in reciprocal space. The Monkhorst-Pack grid is defined by three integers, q_i where i = 1,2,3, which specify the number of divisions along each of the axes. These integers generate a sequence of numbers according to the following:

$$u_r=(2r-q_i-1)/2q_i \tag{3.46}$$

where r varies from 1 to q_i.

The Monkhorst-Pack grid is obtained from these sequences by:

$$\mathbf{k}_{prs}= u_p\mathbf{b}_1 + u_r\mathbf{b}_2 + u_s\mathbf{b}_3 \tag{3.47}$$

This set of q_1, q_2, q_3 distinct points is further symmetrized and weights are assigned according to the number of symmetry images of a given point in the symmetrized set. It is possible to add a constant shift to all of the points in the set before symmetrization. This operation, when applied to hexagonal symmetry systems, results in a slightly modified recipe for the points along the a and b axes:

$$u_p=(p-1)/q_i \tag{3.48}$$

where p varies from 1 to q_i.

3.6 Pseudopotential

Although the Kohn-Sham equations have been shown to be tractable when plane waves are used to expand the electron wave functions, an all-electron calculation including both core and valence electrons, along with the full Coulombic potential of the nuclei would still be prohibitively expensive using a plane wave basis set. This is because the tightly bound core orbitals, and the highly oscillatory nature of the valence electrons, demand that a high value of E_{cut} and hence number of plane waves be used in order to accurately describe the electronic wave functions [14]. However, it is possible to partition the electrons between core and valence states; such a partition is possible because the majority of physical properties of solids

depend upon the valence electrons; in contrast, the core electrons are almost environment independent. It is for this reason that the pseudopotential approximation [31-33] is introduced: the core electrons and ionic potential are removed and replaced with a pseudopotential that acts on a set of pseudo wave functions; this is illustrated schematically in Fig. 3.3. This potential can be represented with only a small number of Fourier coefficients. Pseudo wave-functions ideally should have no nodes inside the core regions and thus they only require a small basis set. It is now well known that the combination of the power of plane wave technology and the pseudopotential concept is extremely useful for the description of chemical bonding [28].

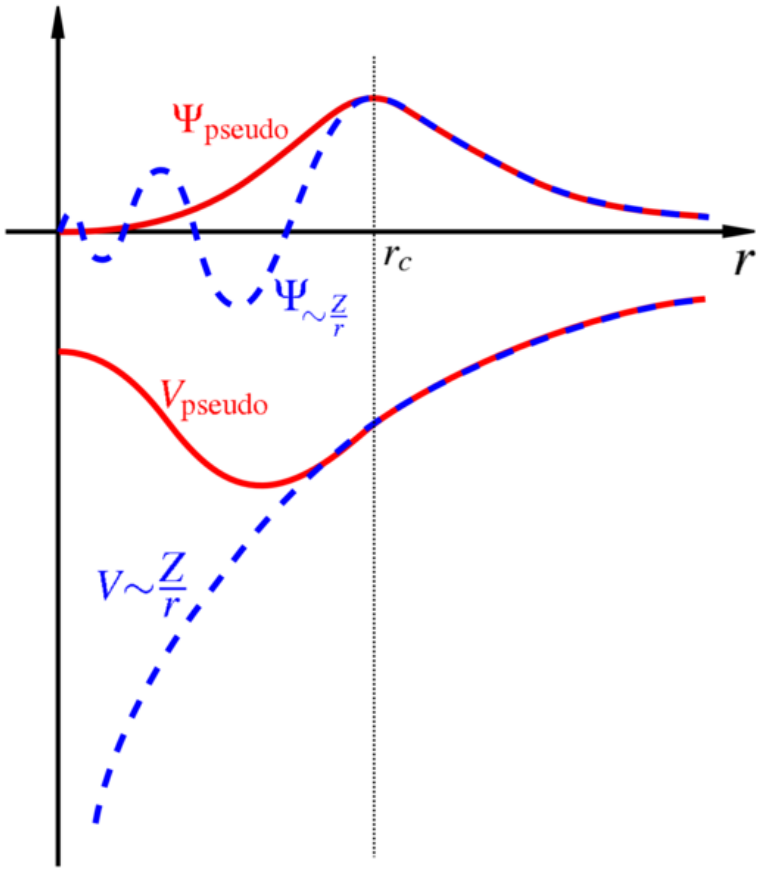

Fig. 3.3. Schematic representation of the all-electron and pseudized wavefunctions and potentials.

Traditionally, pseudopotentials are constructed so as to reproduce faithfully the scattering properties of the full ionic potential. The phase shift produced by the ionic core is different for each angular momentum component (*s*, *p*, *d*, etc.) of the valence wave function. Thus, the scattering from the pseudopotential must be angular momentum dependent. The most general form for pseudopotential is:

$$V_{NL} = \sum |lm\rangle V_l \langle lm| \qquad 3.49)$$

where $|lm\rangle$ are the spherical harmonics and V_l is the pseudopotential for angular momentum l. A pseudopotential that uses the same potential in each angular momentum channel is called a local pseudopotential. Local pseudopotentials are computationally much more efficient than a nonlocal ones, however, only a few elements can be described accurately using local pseudopotentials.

An important concept in the pseudopotential applications is the degree of hardness of pseudopotential. A pseudopotential is considered soft when it requires a small number of Fourier components for its accurate representation and hard otherwise. Early development of accurate norm-conserving pseudopotentials quickly showed that the potentials for transition metals and for first row elements (O, C, N, etc.) turn out to be extremely hard [34,35]. Various schemes have been suggested to improve convergence properties of norm-conserving pseudopotentials [36]. Norm-conserving potentials in CASTEP are generated using the kinetic energy optimization scheme developed by Lin et al., [37] and Lee [38]. A more radical approach was suggested by Vanderbilt [39], which involves relaxing the norm conservation requirement in order to generate much softer pseudopotentials.

Norm-conserving and ultrasoft are the two most common forms of pseudopotential used in modern plane-wave electronic structure codes. They allow a basis-set with a significantly lower cut-off (the frequency of the highest Fourier mode) to be used to describe the electron wave functions and so allow proper numerical convergence with reasonable computing resources. An alternative would be to augment the basis set around nuclei with atomic-like functions, as is done in LAPW. First-

principles pseudopotentials are usually non-local, meaning that different angular momentum states feel different effective potentials.

Norm-conserving pseudopotential

The development of the first-principles norm-conserving pseudopotentials by Kleinman and Bylander [40] has paved the way to accurate calculations of solid-state properties. Kleinman-Bylander pseudopotentials can be expressed formally as

$$V_{KB} = V_{loc} + \sum \frac{|\psi_{lm}\delta V_l\rangle\langle\delta V_l\psi_{lm}|}{\langle\psi_{lm}|\delta V_l|\psi_{lm}\rangle} \tag{4.50}$$

where V_{loc} is an arbitrary local potential, ψ_{lm} are the pseudo-atom wave functions, and δV_l is defined through

$$\delta V_l = V_{l,non-local} - V_{local} \tag{4.51}$$

where $V_{l,non-local}$ is the the l angular momentum component of a non-local pseudopotential. Writing the pseudopotential in this form allows the calculation to scale linearly with the size of the basis set.

Ultrasoft pseudopotentials

In 1990, Vanderbilt [39] proposed a new and radical method for generating much softer pseudopotentials by relaxing the norm-conservation constraint. In this scheme the pseudo-wave-functions are allowed to be as soft as possible within the core region, so that the cutoff energy can be reduced dramatically. For this reason they are usually called ultrasoft pseudopotentials (USP). Technically, this is achieved by introducing a generalized orthonormality condition. The electron density given by the squared moduli of the wave functions has to be augmented in the core region in order to recover the full electronic charge. The electron density is thus subdivided into (i) a smooth part that extends throughout the unit cell, and (ii) a hard part localized in the core regions. The augmented part appears in the density only, not in the wave functions. This differs from methods like LAPW, where a similar approach is applied to wave functions.

Ultrasoft potentials have another advantage besides being much softer than norm-conserving potentials (NCP). The USP generation algorithm guarantees good scattering properties over a pre-specified energy range, which results in much better transferability and accuracy of pseudopotentials. The USP usually also treats "shallow" core states as valence by including multiple sets of occupied states in each angular momentum channel. This also adds to high accuracy and transferability of the potentials, although at a price of computational efficiency. Ultrasoft pseudopotential constructed by Vanderbilt can be expressed as

$$V_{USP} = V_{loc}(r) + \sum_{l,m} D_{lm} |\beta_l\rangle \langle\beta_m| \tag{5.52}$$

Charge density with ultrasoft pseudopotential is defined to be

$$\rho(\mathbf{r}) = \sum_{n,k} \phi_{nk}^*(\mathbf{r})\phi_{nk}(\mathbf{r}) + \sum_{lm} P_{lm} Q_{lm}(\mathbf{r}) \tag{5.53}$$

where

$$D_{lm} = B_{lm} + \varepsilon_m Q_{lm} \tag{5.54}$$

$$P_{lm} = \sum_{n,k} \langle\beta_l|\, \phi_{nk}\rangle\langle\phi_{nk}|\beta_m\rangle \tag{5.55}$$

$$Q_{lm}(\mathbf{r}) = \psi_l^*(\mathbf{r})\psi_m(\mathbf{r}) - \phi_l^*(\mathbf{r})\phi_m(\mathbf{r}) \tag{5.56}$$

Vanderbilt ultrasoft pseudopotentials have a separable form well suited for plane wave's solid-state calculations, and show promise for application to first-row and transition metal systems.

References

[1] E. Schrödinger, "*Quantization as an eigenvalue problem*", Annalen der Physik **79** (1926) 489.

[2] M. Born and R. Oppenheimer, "*The quantum theory of molecules*", Annalen der Physik **84** (1927) 457.

[3] D.R. Hartree, "*The Wave Mechanics of an Atom with a Non-coulomb Central Field: Part I, Theory and Methods*", Math. Proc.Cam. Philos. Soc. **24** (1928) 89.

[4] V. Fock, "*Näherungsmethode zur Lösung des quantenmechanischen Mehrkörperproblems*", Zeitschrift für Physik **61** (1930) 126.

[5] J.C. Slater, "*A Simplification of the Hartree-Fock Method*", Phys. Rev. **81** (1951) 358.

[6] L.H. Thomas, "*Calculation of atomic fields*", Math. Proc. Camb. Phil. Soc. **23** (1927) 542.

[7] E. Fermi, "*Eine statistische Methode zur Bestimmung einiger Eigen-schaften des Atoms und ihre Anwendung auf die Theorie des periodi-schen Systems der Elemente*", Zeitschrift für Physik **48** (1928) 73.

[8] P.A.M. Dirac, "*Note on Exchange Phenomena in the Thomas Atom*", Math. Proc. Cam. Philos. Soc. **26** (1930) 376.

[9] R.O. Jones and O. Gunnarsson, "*The density functional formalism, its applications and prospects*", *Rev. Mod. Phys.*, **61**(1989) 689.

[10] G.D. Mahan, "*Many-Particle Physics",* Plenum Press, New York, 1990.

[11] R.G. Parr and W. Yang, "*Density Functional Theory of Atoms and Molecules*", Oxford University Press, New York, 1989.

[12] P. Hohenberg and W. Kohn, "*Inhomogeneous electron gas*", Phys. Rev. **136** (1964) B864.

[13] W. Kohn and L.J. Sham, "*Self-consistent equations including exchange and correlation effects*", Phys. Rev. **140** (1965) A1133.

[14] M.C. Payne, M.P. Teter, D.C. Allan, T.A. Arias, and J.D. Joannopoulos, "*Iterative minimization techniques for ab initio total-energy calculations: molecular dynamics and conjugate gradients*", Rev. Mod. Phys. **64** (1992) 1045.

[15] S.H. Vosko, L. Wilk and M. Nusair, "*Accurate spin-dependent electron liquid correlation energies for local spin density calculations: a critical analysis*", Can. J. Phys. **58** (1980) 1200.

[16] U. von Barth, L. Hedin, "*A local exchange-correlation potential for the spin polarized case*". J. Phys. C: Solid State Phys. **5** (1972) 1629.

[17] J. P. Perdew and Y. Wang, "*Pair-distribution function and its coupling-constant average for the spin-polarized electron gas*", Phys. Rev. B **46** (1992) 12947.

[18] A.D. Becke, "*Density-functional exchange-energy approximation with correct asymptotic behavior*", Phys. Rev. A **38** (1988) 3098.

[19] J.P. Perdew, J.A. Chevary, S.H. Vosko, K.A. Jackson, M.R. Pederson, D.J. Singh, and C. Fiolhais, "*Atoms, molecules, solids, and surfaces: Applications of the generalized gradient approximation for exchange and correlation*", Phys. Rev. B **46** (1992) 6671.

[20] J.P. Perdew, K. Burke, and M. Ernzerhof, "*Generalized Gradient Approximation Made Simple*", Phys. Rev. Lett. **77** (1996) 3865.

[21] P.P. Rushton, "*Towards a Non-local Description of Exchange and Corrlation*", PhD Thesis, University of Durham (2002).

[22] F. Bloch, "*Über die Quantenmechanik der Elektronen in Kristallgittern*", Zeitschrift für Physik **52** (1929) 555.

[23] M.D. Segall, P.J.D. Lindan, M.J. Probert, C.J. Pickard, P.J. Hasnip, S.J. Clark and M.C. Payne, "*First-principles simulation: ideas, illustrations and the CASTEP code*", J. Phys.: Cond. Matt. **14** 2717 (2002).

[24] M.D. Segall, "*Applications of ab initio atomistic simulations to biology*", J. Phys.: Condens. Matter 14 (2002) 2957.

[25] J.M. Soler, E. Artacho, J.D. Gale, A. García, J. Junquera, P. Ordejón and D. Sánchez -Portal, "*The SIESTA method for ab initio order-N materials simulation*", J. Phys.: Condens. Matter 14 (2002) 2745.

[26] S. Goedecker, "*Linear scaling electronic structure methods*", Rev. Mod. Phys. 71 (1999) 1085.

[27] D.R. Bowler, T. Miyazaki and M.J. Gillan, "*Recent progress in linear scaling ab initio electronic structure techniques*", J. Phys.: Condens. Matter **14** (2002) 2781.

[28] G.P. Srivastava, D. Weaire, "*The theory of the cohesive energies of solids*", Adv. Phys. **26** (1987) 463.

[29] H.J. Monkhorst and J.D. Pack, "*Special points for Brillouin-zone integrations*", Phys. Rev. B **13** (1976) 5188.

[30] H.J. Monkhorst, and J.D. Pack, "*Special points for Brillouin-zone integrations - a reply*", Phys. Rev. B **16** (1977) 1748.

[31] J.C. Phillips, "*Energy-Band Interpolation Scheme Based on a Pseudopotential*", Phys. Rev. **112** (1958) 685.

[32] J.C. Phillips and L. Kleinman, "*New Method for Calculating Wave Functions in Crystals and Molecules*", Phys. Rev. **116** (1959) 287.

[33] M.L. Cohen and V. Heine, "*The Fitting of Pseudopotentials to Experimental Data and Their Subsequent Application*", Solid State Physics **24** (1970) 37.

[34] G. Kerker, "*Non-singular atomic pseudopotentials for solid state applications*", J. Phys. C **13** (1980) L189.

[35] G.B. Bachelet, D.R. Hamann, and M. Schluter, "*Pseudopotentials that work: From H to Pu*", Phys. Rev. B **26** (1982) 4199.

[36] N. Troullier, J.L. Martins, "*Efficient pseudopotentials for plane-wave calculations*", Phys. Rev. B **43** (1991) 1993.

[37] J.S. Lin, A. Qteish, M.C. Payne, and V. Heine, "*Optimized and transferable nonlocal separable ab initio pseudopotentials*", Phys. Rev. B **47** (1993) 4174.

[38] M.H. Lee, PhD Thesis, Cambridge University (1996).

[39] D. Vanderbilt, "*Soft self-consistent pseudopotentials in a generalized eigenvalue formalism*", Phys. Rev. B, **41** (1990) 7892.

[40] L. Kleinman and D.M. Bylander, "*Efficacious Form for Model Pseudopotentials*", Phys. Rev. Lett. **48**, 1425 (1982).

4. Theory of Investigated Properties

The purpose of the present chapter is to provide an overview of the theory used to investigate the different properties of superconducting MAX phases Nb_2AsC, Nb_2InC, Mo_2GaC, and Ti_2GeC. In the present work, the goal is fixed to calculate the ground state crystal energy and from this the equilibrium lattice parameters, unit cell volume, bulk modulus, elastic constants, band structure, total and partial density of states are evaluated. Theoretical Vickers hardness and Fermi surface are determined to add the information about the bonding nature of four 211MAX superconducting phases. The optical properties (such as dielectric function, refractive index, extinction coefficient, absorption spectrum, energy loss function, reflectivity and photoconductivity) and thermodynamic properties (such as bulk modulus, Debye temperature, specific heats and volumetric thermal expansion coefficient) are also calculated. The discussions of the theory of above mentioned properties are the including subjects of this chapter.

4.1 Ground State Energy

The CASTEP Geometry Optimization task allows one to refine the geometry of a 3D periodic system to obtain a stable structure or polymorph. This is done by performing an iterative process in which the coordinates of the atoms and possibly the cell parameters are adjusted so that the total energy of the structure is minimized. This minimized total energy is the ground state energy of the system.

In the field of computational chemistry, energy minimization (also called energy optimization or geometry optimization) is the process of finding an arrangement in space of a collection of atoms where, according to some computational model of chemical bonding, the net inter-atomic force on each atom is acceptably close to zero and the position on the potential energy surface is a stationary point. The collection of atoms might be a single molecule, an ion, a condensed phase, a transition state or even a collection of any of these. The computational model of chemical bonding might, for example, be quantum mechanics.

The geometry of a set of atoms can be described by a vector of the atoms' positions. This could be the set of Cartesian coordinates of the atoms or, when considering molecules, might be so called internal coordinates formed from a set of bond lengths, bond angles and dihedral angles.

Given a set of atoms and a vector, **r**, describing the atoms' positions, one can introduce the concept of the energy as a function of the positions, $E(\mathbf{r})$. Geometry optimization is then a mathematical optimization problem, in which it is desired to find the value of **r** for which $E(\mathbf{r})$ is at a local minimum, that is, the derivative of the energy with respect to the position of the atoms, $\partial E/\partial \mathbf{r}$, is the zero vector and the second derivative matrix of the system, $\partial\partial E/\partial r_i \partial r_j$, also known as the Hessian matrix, which describes the curvature of the potential energy surface at **r**, has all positive eigenvalues (is positive definite).

The computational model that provides an approximate $E(\mathbf{r})$ could be based on quantum mechanics or force fields. Using this computational model and an initial guess (or Ansatz) of the correct geometry, an iterative optimization procedure is followed, for example:

1. calculate the force on each atom (that is, $-\partial E/\partial \mathbf{r}$)
2. if the force is less than some threshold, finish
3. otherwise, move the atoms by some computed step $\Delta\mathbf{r}$ that is predicted to reduce the force
4. repeat from the start

4.2 Elastic Properties

Elastic properties of a solid are important because they relate to the various fundamental solid-state properties such as interatomic potentials, equation of state, and phonon spectra. Elastic properties are also linked thermodynamically to the specific heat, thermal expansion, Debye temperature, melting point, and Grüneisen parameter. Elastic properties of materials are also closely associated with the shear moduli along the slip planes of mobile dislocations, since these

dislocations can dissociate into partials with a spacing determined by the balance between the fault energy and the repulsive elastic force. The elastic constants determine the response of the crystal to external forces, as characterized by bulk modulus, shear modulus, Young's modulus, and Poisson's ratio, and obviously play an important part in determining the strength of the materials. Values of elastic constants provide valuable information about the bonding characteristic between adjacent atomic planes and the anisotropic character of the bonding and structural stability. It has also been noticed that there is a correlation between the elastic constants and the melting temperature of a solid. Elastic properties are classified into two types. These are discussed in below:

4.2.1 Single Crystal Elastic Constants

The elastic constants of a material describe its response to an applied stress or, conversely, the stress required to maintain a given deformation. Both stress and strain have three tensile and three shear components, giving six components in total. The linear elastic constants form a 6 × 6 symmetric matrix, having 27 different components, such that $\sigma_i = C_{ij}\,\varepsilon_j$ for small stresses, σ, and strains, ε [1]. Any symmetry present in the structure may make some of these components equal and others may be fixed at zero. Thus, a hexagonal crystal like MAX phases has only six different symmetry elements (C_{11}, C_{12}, C_{13}, C_{33}, C_{44} and C_{66}), and only five of them are independent since $C_{66} = (C_{11} - C_{12})/2$. Properties such as the bulk modulus (response to anisotropic compression), Poisson ratio, Lame constants, and so forth may be computed from the values of C_{ij}.

Methods to determine the elastic constants from first principles usually involve setting either the stress or the strain to a finite value, re-optimizing any free parameters and calculating the other property (the strain or stress, respectively). The finite strain technique has been successfully used to study the elastic properties of a range of materials including metallic systems. This is the method implemented in CASTEP.

The elastic constants are determined by a Taylor expansion of the total energy of the system $E(V,\delta)$, with respect to a small strain δ of the lattice of volume V. The Bravais lattice for hexagonal crystal structure is spanned by three vectors ($\sqrt{3}a/2$, -a/2, 0), (0, 0, 0), and (0, 0, c). In matrix form the Bravais lattice vectors are expressed as:

$$R = \begin{pmatrix} \sqrt{3}a/2 & -a/2 & 0 \\ 0 & a & 0 \\ 0 & 0 & c \end{pmatrix} \tag{4.1}$$

We express the energy of the strained system by means of a Taylor expansion in the distortion parameters [2]:

$$E(V,\delta) = E(V_0,0) + V_0\left[\sum_i \tau_i\xi_i\delta_i + \frac{1}{2}\sum_{ij} C_{ij}\delta_i\xi_i\delta_j\xi_j\right], \tag{4.2}$$

where $E(V_0,0)$ is the energy of the unstrained system with equilibrium volume V_0, τ_i is an element in the stress tensor, and ξ_i is a factor to take care of Voigt index. The linear terms vanish if the strain causes no changes in the volume of the crystal. Otherwise, τ_i is related to the strain on the crystal. Since there are five independent elastic constants for hexagonal crystal, we need five deferent strains (distortions) to determine these. The first distortion is written as:

$$D_1 = \begin{pmatrix} 1+\delta & 0 & 0 \\ 0 & 1+\delta & 0 \\ 0 & 0 & 1 \end{pmatrix} \tag{4.3}$$

This changes the size of the basal plane, maintaining the z-axis constant. The symmetry of the strained lattice is therefore still hexagonal and the energy for this distortion can be obtained as:

$$E(V,\delta) = E(V_0,0) + V_0[(\tau_1+\tau_2)\delta + (C_{11}+C_{12})\delta^2] \tag{4.4}$$

The second type of distortion elongates the cell along x-axis and compresses along the y-axis while conserving the volume and leads to monoclinic symmetry:

$$D_2 = \begin{pmatrix} 1+\delta & 0 & 0 \\ 0 & 1-\delta & 0 \\ 0 & 0 & 1 \end{pmatrix} \tag{4.5}$$

The energy for this distortion can be expressed as:

$$E(V,\delta) = E(V_0,0) + V_0[(\tau_1 - \tau_2)\delta + (C_{11} - C_{12})\delta^2] \tag{4.6}$$

The third distortion stretches or compresses the z-axis while keeping the other axis unchanged. The volume changes but the symmetry is preserved. The distortion is as follows:

$$D_3 = \begin{pmatrix} 1 & 0 & 0 \\ 0 & 1 & 0 \\ 0 & 0 & 1+\delta \end{pmatrix} \tag{4.7}$$

The elastic constant can be obtained from the energy relation

$$E(V,\delta) = E(V_0,0) + V_0[\tau_3\delta + \frac{1}{2}C_{33}\delta^2] \tag{4.8}$$

In the forth distortion, the c/a ratio is assumed to be constant under a small strain, gives compression or expansion to the system. The symmetry is conserved but the volume changes. The deformation is written as:

$$D_4 = \begin{pmatrix} 1+\delta & 0 & 0 \\ 0 & 1+\delta & 0 \\ 0 & 0 & 1+\delta \end{pmatrix} \tag{4.9}$$

The strain energy associated with this distortion is

$$E(V,\delta) = E(V_0,0) + V_0[(\tau_1 + \tau_2 + \tau_3)\delta + \frac{1}{2}(2C_{11} + 2C_{12} + 4C_{13} + C_{33})\delta^2] \tag{4.10}$$

Finally, the fifth one is the volume conserving triclinic distortion and can be written as:

$$D_5 = \begin{pmatrix} 1 & 0 & \delta \\ 0 & 1 & 0 \\ \delta & 0 & 1 \end{pmatrix} \tag{4.11}$$

The energy corresponding to this distortion can be written as:

$$E(V,\delta) = E(V_0,0) + V_0[\tau_5\delta + 2C_{44}\delta^2] \tag{4.12}$$

The relations (4.4), (4.6), (4.8), (4.10), and (4.12) give the five independent elastic constants C_{11}, C_{12}, C_{13}, C_{33}, and C_{44}, respectively.

4.2.2 Elastic properties of polycrystalline aggregate

The theoretical polycrystalline elastic properties for hexagonal crystal can be calculated from the set of five independent elastic constants.

The bulk modulus (B) and shear modulus (G) of polycrystalline aggregates are calculated from individual elastic constants, C_{ij}, by the well-known Voigt [3] and the Reuss [4] approximations that are frequently used in averaging the single-crystal elastic constants for polycrystalline behavior. Voigt assumes the uniform strain throughout a polycrystalline aggregate and Reuss assumes the uniform stress. The bulk modulus B_V and shear modulus G_V in the Voigt approximation for the hexagonal lattice are expressed as:

$$B_V = \frac{1}{9}[2(C_{11}+C_{12}) + 4C_{13} + C_{33}] \tag{4.13}$$

$$G_V = \frac{1}{30}(C_{11}+C_{12}+2C_{33}-4C_{13}+12C_{44}+12C_{66}) \tag{4.14}$$

In the Reuss approximation, the bulk modulus B_R and the shear modulus G_R are defined as:

$$B_R = \frac{(C_{11}+C_{12})C_{33}-2C_{13}^2}{C_{11}+C_{12}+2C_{33}-4C_{13}} \tag{4.15}$$

$$G_R = \frac{5C_{44}C_{66}[(C_{11}+C_{12})C_{33}-2C_{13}^2]}{2[3B_VC_{44}C_{66}+\{(C_{11}+C_{12})C_{33}-2C_{13}^2\}(C_{44}+C_{66})]} \tag{4.16}$$

It is evident that the Voigt and Reuss assumptions are true only when the aggregate concerned is made of isotropic crystals, but for an aggregate made of anisotropic crystals their assumptions become immediately invalid. Hill [5] has shown that

for an aggregate of anisotropic crystals the Voigt and Reuss assumptions result in theoretical maximum and minimum values of the isotropic elastic moduli of the polycrystalline aggregate, respectively, and suggested that the actual effective moduli of anisotropic polycrystalline crystals could be approximated by the arithmetic mean of the two values. According to Hill approximation, the bulk modulus B and shear modulus G are given by:

$$B = \frac{1}{2}(B_R + B_V) \quad \text{and} \quad G = \frac{1}{2}(G_R + G_V) \tag{4.17}$$

Again, the calculated bulk modulus B and shear modulus G allow us to estimate the Young's modulus Y and Poisson's ratio ν by the following relations [6]:

$$Y = \frac{9BG}{3B+G} \quad \text{and} \quad \nu = \frac{3B-2G}{2(3B+G)} \tag{4.18}$$

The accuracy of DFT elastic constants is typically within 10% or less of experiment. This allows us to predict elastic constants for new materials or for materials where experimental data do not exist; to predict elastic properties under pressure or to resolve discrepancies between contradictory experimental results.

4.3 Electronic properties

4.3.1 Band structure

The electrons of a single isolated atom occupy atomic orbitals, which form a discrete set of energy levels. If multiple atoms are brought together into a molecule, their atomic orbitals will combine to form molecular orbitals each with a different energy. In other words, n atomic orbitals will combine to form n molecular orbitals. As more and more atoms are brought together, the molecular orbitals extend larger and larger, and the energy levels of the molecule will become increasingly dense. Eventually, the collection of atoms forms a giant molecule, or in other words, a solid. For this giant molecule, the energy levels are so close that they can be considered to form a continuum known as energy bands,

allowed bands, or simply bands that an electron within the solid may have. The bands have different widths, with the widths depending upon the degree of overlap in the atomic orbitals from which they arise. Two adjacent bands may simply not be wide enough to fully cover the range of energy. So, a gap is found between two adjacent bands. This gap is called band gaps or forbidden bands. Band gaps are essentially leftover ranges of energy not covered by any band, a result of the finite widths of the energy bands. The full picture of energy bands and band gaps of a solid is known as electronic band structure or simply band structure.

In fact, in solid-state physics, the band structure describes those ranges of energy that an electron within the solid may have, and ranges of energy that it may not have. In view of quantum mechanics, it is due to the diffraction of the quantum mechanical electron waves in the periodic crystal lattice. Band theory derives these bands and band gaps by examining the allowed quantum mechanical wave functions for an electron in a large, periodic lattice of atoms or molecules or solids.

Band structure calculations take advantage of the periodic nature of a crystal lattice, exploiting its symmetry. The single-electron Schrödinger equation is solved for an electron in a lattice-periodic potential, giving Bloch waves as solutions:

$$\psi_{n\mathbf{k}}(\mathbf{r}) = e^{i\mathbf{k}.\mathbf{r}} u_{n\mathbf{k}}(\mathrm{r}), \tag{4.19}$$

where **k** is called the wave vector. For each value of **k**, there are multiple solutions to the Schrödinger equation labeled by n, the band index, which simply numbers the energy bands. Each of these energy levels evolves smoothly with changes in **k**, forming a smooth band of states. For each band we can define a function $E_n(\mathbf{k})$, which is the dispersion relation for electrons in that band. The wave vector takes on any value inside the Brillouin zone, which is a polyhedron in wave vector space that is related to the crystal's lattice. Wave vectors outside the Brillouin zone simply correspond to states that are physically identical those states within the Brillouin zone. Special high symmetry points in the Brillouin zone are assigned labels Γ, H, K, Γ, M, L for hexagonal 211 MAX phases.

It is difficult to visualize the shape of a band as a function of wave vector, as it would require a plot in four-dimensional space, E vs. k_x, k_y,k_z. In scientific literature it is common to see band structure plots which show the values of $E_n(\mathbf{k})$ for values of $\mathbf{k}$ along straight lines connecting symmetry points. Another method for visualizing band structure is to plot a constant-energy isosurface in wave vector space, showing all of the states with energy equal to a particular value. The isosurface of states with energy equal to the Fermi level is known as the Fermi surface.

A solid has an infinite number of allowed bands, just as an atom has infinitely many energy levels. However, most of the bands simply have too high energy, and are usually disregarded under ordinary circumstances [7]. Conversely, there are very low energy bands associated with the core orbitals (such as 1s electrons). These low-energy *core band*s are also usually disregarded since they remain filled with electrons at all times, and are therefore inert [8]. Likewise, materials have several band gaps throughout their band structure. The most important bands and band gaps-those relevant for electronics and optoelectronics-are those with energies near the Fermi level. The bands and band gaps near the Fermi level are given special names, depending on the material:

- In a semiconductor or band insulator, the Fermi level is surrounded by a band gap. The closest band above the band gap is called the conduction band, and the closest band beneath the band gap is called the valence band. The name "valence band" was coined by the analogy to the chemistry, since in many semiconductors the valence band is built out of the valence orbitals.

- In a metal or semimetal, the Fermi level is inside of one or more allowed bands. In semimetals the bands are usually referred to as "conduction band" or "valence band" depending on whether the charge transport is more electron-like or hole-like, by analogy to semiconductors. In many metals, however, the bands are neither electron-like nor hole-like, and often just called "valence band" as they are made of valence orbitals. The band gaps in a metal's band structure are not important for low energy physics, since they are too far from the Fermi level.

Energy band gaps can be classified using the wave vectors of the states surrounding the band gap:

- Direct band gap: the lowest-energy state above the band gap has the same **k** as the highest-energy state beneath the band gap.
- Indirect band gap: the closest states above and beneath the band gap do not have the same **k** value.

4.3.2 Density of states

In quantum mechanical (QM) systems, waves, or wave-like particles can occupy modes or states with wavelengths and propagation directions dictated by the system. Often only specific states are permitted. In some systems, the interatomic spacing and the atomic charge of the material allows only electrons of the certain wavelengths to exist. In other systems, the crystalline structure of the material allows waves to propagate in one direction, while suppressing wave propagation in another direction. Thus it can happen that many states are possible at a specific wavelength, and therefore at this associated energy, while no states are available at other energy levels: this distribution is characterized by the density of states (DOS). Depending on the QM system the density of the states can be calculated for electrons, photons, or phonons, and can be given as a function of either energy or the wave vector k.

In solid-state and condensed matter physics, the electron density of states of a system describes the number of states per interval of energy at each energy level that are available to be occupied by electrons. A high DOS at a specific energy level means that there are many states available for occupation. A DOS of zero means that no states can be occupied at that energy level. In general a DOS is an average over the space and time domains occupied by the system

The density of states (DOS) for a given band n, $N_n(E)$, is defined as:

$$N_n(E) = \int \frac{d\mathbf{K}}{4\pi^3} \delta(E - E_n(\mathbf{K})), \tag{4.20}$$

where $E_n(\mathbf{k})$ describes the dispersion of the given band and the integral is determined over the Brillouin zone. An alternative representation of the density of states is based on the fact that $N_n(E)dE$ is proportional to the number of allowed wave vectors in the nth band in the energy range E to $(E + dE)$.

The total density of states, $N(E)$, is obtained by summation over all bands:

$$N(E) = \sum N_n(E) = \sum \int \frac{d\mathbf{K}}{4\pi^3} \delta(E - E_n(\mathbf{K})) \tag{4.21}$$

The integral of $N(E)$ from minus infinity to the Fermi level gives the total number of electrons in the unit cell.

$$N_{uc} = \int_{-\infty}^{E_F} N(E)dE \tag{4.22}$$

In a spin-polarized system, separate DOS for electrons with spin up and spin down can be introduced. Their sum produces the total DOS and their difference is referred to as the spin density of states.

DOS is often used for quick visual analysis of the electronic structure. Characteristics such as the width of the valence band, the energy gap in insulators and the number and intensity of the main features are helpful in qualitatively interpreting the experimental spectroscopic data. DOS analysis can also help to understand the changes in electronic structure caused by, for example, external pressure.

There are a variety of numerical techniques for evaluating the DOS. CASTEP use a simplified linear interpolation scheme developed by Ackland [9]. This method is based on linear interpolation in parallelepipeds formed by the points of Monkhorst-Pack set, followed by the histogram sampling of the resultant set of band energies.

Partial and local density of states

Partial density of states (PDOS) and local density of states (LDOS) represent useful semi-qualitative tools for analyzing electronic structure. LDOS shows which atoms in the system contribute electronic states to various parts of the energy spectrum.

PDOS further qualifies these results by resolving the contributions according to the angular momentum of the states. It is often useful to know whether the main peaks in the DOS are of *s*, *p*, or *d* character. LDOS and PDOS analyses give a qualitative handle on the nature of electron hybridization in the system, on the origin of the main features in X-ray photoelectron spectroscopy and optical spectra, etc.

PDOS calculations are based on Mulliken population analysis, which allows the contribution from each energy band to a given atomic orbital to be calculated. The summation of these contributions over all bands produces a weighted DOS. CASTEP allow one to select the type of weighting required. It is possible, for example, to generate LDOS by adding together all the contributions due to orbitals on a given atom.

PDOS analysis formalism is not valid for high energy states in the conduction band: PDOS representation will usually decay to zero at about 20 eV above the Fermi level. This is related to the fact that expansion of essentially free electron states in terms of a limited number of atomic-like basis functions is impossible to carry out with any degree of accuracy. Only the valence band and lower part of the conduction band are meaningful in the PDOS plot.

The calculation itself can be carried out using either Gaussian smearing or linear interpolation, similar to the total DOS calculation. In this case, the latter method includes the interpolation of the weights as well as the electronic energies.

4.3.3 Fermi surface

Fermi surfaces are abstract boundaries, useful for predicting the thermal, electrical, magnetic, and optical properties of metals, semi-metals, and doped semiconductors. The shape of the Fermi surface is derived from the periodicity and symmetry of the crystalline lattice and from the occupation of electronic energy bands. The existence of a Fermi surface is a direct consequence of the Pauli Exclusion Principle, which allows a maximum of one electron per quantum state.

In the one-particle approximation Fermi surface can be considered as an energy isosurface, E (k) = E_F (Fermi energy), in reciprocal space. Because the Fermi surface is an infinite periodic object it is conventionally represented as being clipped by the Brillouin zone.

The Fermi surface problem is the counterpart of the band gap problem for metals. The highest occupied energy in the density functional Khon-Sham equations can easily be shown to be the energy for adding an electron to a metal and is thus the chemical potential. The problem is whether the Fermi surface given by the eigen energies of the Khon-Sham equations is the same as the true Fermi surface. The true Fermi surface can be constructed from the one-particle Green's function which gives the quasi-particle energies. The LDA-like approximation for the Green's function [10] yields the same Fermi as Khon-Sham equations.

By the Pauli exclusion principle, no two particles can be in the same state. Therefore, in the state of lowest energy, the particles fill up all energy levels below E_F, which is equivalent to saying that E_F is the energy level below which there are exactly N states.

In momentum space, these particles fill up a sphere of radius P_F, the surface of which is called the Fermi surface [11].

The linear response of a metal to an electric, magnetic or thermal gradient is determined by the shape of the Fermi surface, because currents are due to changes in the occupancy of states near the Fermi energy. Free-electron Fermi surfaces are spheres of radius

$$k_F = \frac{\sqrt{2mE_F}}{\hbar}, \tag{4.23}$$

determined by the valence electron concentration where $\hbar$ is the reduced Planck's constant. A material whose Fermi level falls in a gap between bands is an insulator or semiconductor depending on the size of the band gap. When a material's Fermi level falls in a band gap, there is no Fermi surface.

4.4 Mulliken bond population and theoretical hardness

Mulliken charges and bond populations are calculated according to the formalism described by Segall et al. [12,13]. In Mulliken analysis [14] the charge associated with a given atom, A, is determined by:

$$Q(A) = \sum_{\mathbf{K}} w_{\mathbf{K}} \sum_{\mu}^{onA} \sum_{\nu} P_{\mu\nu}(\mathbf{K}) S_{\nu\mu}(\mathbf{K}) \tag{4.24}$$

and the overlap population between two atoms, A and B, is:

$$P^{\mu}(AB) = \sum_{\mathbf{K}} w_{\mathbf{K}} \sum_{\mu}^{onA} \sum_{\nu}^{onB} 2P_{\mu\nu}(\mathbf{K}) S_{\nu\mu}(\mathbf{K}) \tag{4.25}$$

Mulliken bond populations provide a deep understanding about the bonding nature in crystals and the first-key step of calculating the theoretical Vickers hardness. To estimate accurately the values of Vickers hardness of metallic crystals, the already established empirical formula is as follows [15,16]:

$$H_V = \left[\prod_{\mu} \left\{ 740 \left(P^{\mu} - P^{\mu'} \right) \left(v_b^{\mu} \right)^{-5/3} \right\}^{n^{\mu}} \right]^{1/\sum n^{\mu}}, \tag{4.26}$$

where P^{μ} is the Mulliken bond overlap population, v_b^{μ} is the bond volume, and n^{μ} is the number of μ-type bond and $P^{\mu'}$ is the metallic population.

4.5 Optical properties

By “optical properties” is meant a material’s response to exposure to electro-magnetic radiation and, in particular to visible light. When radiations are exposed to electromagnetic radiation, it is sometimes important to be able to predict and after their responses. This is possible when we are familiar with their optical properties and understand the mechanisms responsible for their optical behaviors. This section will discuss some of the basic theories and concepts relating to the nature of electromagnetic radiation and its possible interactions with solid materials.

To extract all optical properties, the frequency dependent dielectric function is a key optical quantity, $\varepsilon(\omega) = \varepsilon_1(\omega) + i\varepsilon_2(\omega)$, which keeps up a close relation to the electronic band structure. On the basis of the momentum matrix elements between the occupied and the unoccupied electronic states, the imaginary part $\varepsilon_2(\omega)$ of the dielectric function can be expressed as:

$$\varepsilon_2(\omega) = \frac{2e^2\pi}{\Omega\varepsilon_0} \sum_{k,v,c} |\langle \psi_k^c | \boldsymbol{u} \cdot \boldsymbol{r} | \psi_k^v \rangle|^2 \, \delta(E_k^c - E_k^v - E) \tag{4.27}$$

where ω is the frequency of light, e is the electronic charge, $\boldsymbol{u}$ is the vector defining the polarization of the incident electric field, and ψ_k^c and ψ_k^v are the conduction and valence band wave functions at k, respectively. From the imaginary part $\varepsilon_2(\omega)$, the real part $\varepsilon_1(\omega)$ of the dielectric function is derived through the Kramers-Kronig relations:

$$\varepsilon_1(\omega) = 1 + \frac{2}{\pi} P \int_0^\infty \frac{\omega' \varepsilon_2(\omega') d\omega'}{(\omega'^2 - \omega^2)} \tag{4.28}$$

where P represents the principal integral.

The remaining optical properties, such as refractive index, absorption spectrum, loss-function, reflectivity and photoconductivity (real part) are derived from $\varepsilon(\omega)$, $\varepsilon_1(\omega)$, and $\varepsilon_2(\omega)$. For the metallic compounds both inter-band and intra-band transitions contribute to dielectric function. As the investigated material is metallic, which is evident from our calculated band structure, a Drude term [17,18] with unscreened plasma frequency 5 eV and damping 0.05 eV has been be used. Its effect is to enhance the low energy part of the spectrum.

The refractive index, $n(\omega)$, and the extinction coefficient, $k(\omega)$, are evaluated in terms of the real as well as imaginary parts of the complex dielectric function as follows:

$$n(\omega) = \frac{1}{\sqrt{2}} \left[\sqrt{\{\varepsilon_1(\omega)\}^2 + \{\varepsilon_2(\omega)\}^2} + \varepsilon_1(\omega) \right]^{1/2} \tag{4.29}$$

$$k(\omega) = \frac{1}{\sqrt{2}}\left[\sqrt{\{\varepsilon_1(\omega)\}^2 + \{\varepsilon_2(\omega)\}^2} - \varepsilon_1(\omega)\right]^{1/2} \tag{4.30}$$

Expressions for the absorption coefficient $\alpha(\omega)$, energy loss function $L(\omega)$, and the real part of optical conductivity $\sigma(\omega)$ are given as:

$$\alpha(\omega) = \sqrt{2}\omega\left[\sqrt{\{\varepsilon_1(\omega)\}^2 + \{\varepsilon_2(\omega)\}^2} - \varepsilon_1(\omega)\right]^{1/2} \tag{4.31}$$

$$L(\omega) = \varepsilon_2(\omega)/[\{\varepsilon_1(\omega)\}^2 + \{\varepsilon_2(\omega)\}^2] \tag{4.32}$$

$$\sigma(\omega) = \frac{\omega\varepsilon_2}{4\pi} \tag{4.33}$$

The reflectivity $R(\omega)$ follows directly from Fresnel's formula if the crystal surface is oriented parallel to the optical axis and is given by

$$R(\omega) = \left|\frac{\sqrt{\varepsilon(\omega)} - 1}{\sqrt{\varepsilon(\omega)} + 1}\right|^2, \tag{4.34}$$

4.6 Thermodynamic Properties

The DFT-based quasi-harmonic Debye model [19], in which the phononic effect is considered, is applied to investigate the thermodynamic properties of solids. According to standard thermodynamics, if the system is held at a fixed T and suffers a constant and hydrostatic pressure P, the equilibrium state is one that minimizes the non-equilibrium Gibbs energy of the crystal phase [20],

$$G^*(\mathbf{x}; P, T) = E(\mathbf{x}) + PV(\mathbf{x}) + A_{vib}(\mathbf{x}; T), \tag{4.35}$$

with respect to all internal configuration parameters. These parameters, gathered in the configuration vector **x**, include all the relevant geometric information for the given crystal structure. On the right-hand side of the Eq. (4.35), $E(\mathbf{x})$ is the total energy of the crystal. The second term, PV, corresponds to the constant hydrostatic pressure condition. Finally, the third term, A_{vib}, is the vibrational Helmholtz free energy including the contributions of the lattice vibration on the

internal energy and entropy change. The rigorous statistical calculation of A_{vib} depends on the knowledge of the exact vibrational levels is obtained by the quasi-harmonic approximation [20],

$$A_{vib}(x;T) = \int_0^{\infty} \left[\frac{1}{2}\hbar\omega + kT\ln\left(1 - e^{-\hbar\omega/kT}\right)\right] \mathrm{g}(\mathbf{x};\omega)\mathrm{d}\omega, \tag{4.36}$$

where g(x;ω) is the phonon or vibrational density of states. Applying the static condition Eq. (4.35) can be changed as the following form:

$$G^*(V;P,T) = E(\mathrm{V}) + PV + A_{vib}(\theta_D(V);T), \tag{4.37}$$

Now, the Debye model of the phonon density of states allows us to write the vibrational Helmholtz free energy as [21,22]

$$A_{vib}(\theta_D,T) = nkT\left[\frac{9\theta_{\mathrm{D}}}{8T} + 3\ln(1 - e^{-\theta_D/T}) - D(\theta_D/T)\right], \tag{4.38}$$

where θ_D is the Debye temperature, n is the number of atoms per formula unit, and $D(\theta_D/\mathrm{T})$ is the Debye integral, which is defined as

$$D(\theta_D/T) = \frac{3}{(\theta_D/T)^3}\int_0^{\theta_D/T} \frac{x^3}{e^x - 1}dx \tag{4.39}$$

For an isotropic solid with Poisson ratio σ, the characteristic Debye temperature θ_D can be expressed as

$$\theta_D = \frac{\hbar}{k}\left[6\pi^2 V^{1/2} n\right]^{1/3} f(\sigma)\sqrt{\frac{B_S}{M}}, \tag{4.40}$$

where M is the molecular mass per formula unit and B_S is the adiabatic bulk modulus that can be computed as

$$B_S \approx B(V) = V\left(\frac{d^2E(V)}{dV^2}\right) \tag{4.41}$$

and the $f(\sigma)$ is defined as

$$f(\sigma) = \left\{3\left[2\left(\frac{2}{3}\frac{1+\sigma}{1-2\sigma}\right)^{3/2} + \left(\frac{1}{3}\frac{1+\sigma}{1-\sigma}\right)^{3/2}\right]^{-1}\right\}^{1/3} \tag{4.42}$$

Therefore, for the given pressure P and temperature T with respect to the volume V, the non-equilibrium Gibbs function merely depends on $V(P,T)$ and can be solved as

$$\left(\frac{\partial G^*(V;P,T)}{\partial V}\right)_{P,T} = 0 \tag{4.43}$$

By solving Eq. (4.43), the thermal equation of state (EOS) $V(P,T)$ can be obtained. Then the isothermal bulk modulus B_T, the constant- volume heat capacity C_V, the constant-pressure heat capacity C_P, which account for the lattice contribution, and volumetric thermal expansion α can be derived as

$$B_T(P,T) = V\left(\frac{\partial^2 G^*(V;P,T)}{\partial V^2}\right)_{P,T} \tag{4.44}$$

$$C_V = 3nk\left[4D\left(\frac{\theta_D}{T}\right) - \frac{3\theta_D/T}{e^{\theta_D/T}-1}\right] \tag{4.45}$$

$$C_P = C_V(1+\alpha\gamma T) \tag{4.46}$$

$$\alpha_V = \frac{\gamma C_V}{B_T V} \tag{4.47}$$

where γ is the Grüneisen parameter, which is defined as

$$\gamma = -\frac{d\ln\theta_D(V)}{d\ln V} \tag{4.48}$$

To obtain the values of all the thermodynamic properties defined above, the non-equilibrium Gibbs function G^* and the energy E would be predetermined.

References

[1] N.W. Ashcroft, N.D. Mermin, "*Solid State Physics*", Saunders College: Philadelphia (1976).

[2] L. Fast, J.M. Wills, B. Johansson, and O. Eriksson, "*Elastic constants of hexagonal transition metals: Theory*", Phys. Rev. B **51** (1995) 17431.

[3] W. Voigt, "*Lehrbuch der Kristallphysik*", Taubner, Leipzig, 1928.

[4] A. Reuss, "*Berechnung der Fließgrenze von Mischkristallen auf Grund der Plastizitätsbedingung für Einkristalle*", Z. Angew. Math. Mech. **9** (1929) 49.

[5] R. Hill, "*The Elastic Behaviour of a Crystalline Aggregate*", Proc. Phys. Soc. A **65** (1952) 349.

[6] E. Schreiber, O.L. Anderson, and N. Soga, "*Elastic Constants and Their Measurements*", McGraw-Hill, New York, 1973.

[7] R. Stern, J. Perry, and D. Boudreaux, "*Low-Energy Electron-Diffraction Dispersion Surfaces and Band Structure in Three-Dimensional Mixed Laue and Bragg Reflections*", Rev. Mod. Phys. **41** (1969) 275.

[8] IUPAC, "*Compendium of Chemical Terminology*", 2nd ed. (the "Gold Book") (1997). Online corrected version: (2006).

[9] G.J. Ackland, "*Embrittlement and the Bistable Crystal Structure of Zirconium Hydride*", Phys. Rev. Lett. **80** (1998) 2233.

[10] L.J. Sham, W. Khon, "*One-particle properties of an inhomogeneous interacting electron gas*", Phys. Rev. **145** (1966) 561.

[11] K. Huang, "*Statistical Mechanics*", (2000), p-244.

[12] M.D. Segall, R. Shah,. C.J. Pickard, M.C. Payne, "*Population analysis in plane wave electronic structure calculations*", Mol. Phys. **89** (1996) 571.

[13] M.D. Segall, R. Shah,. C.J. Pickard, M.C. Payne, "*Population analysis of plane-wave electronic structure calculations of bulk materials*", Phys. Rev. B **54** (1996) 16317.

[14] R.S. Mulliken, "*Electronic Population Analysis on LCAO-MO Molecular Wave Functions*", J. Chem. Phys. **23** (1955) 1833.

[15] F. M. Gao, "*Theoretical model of intrinsic hardness*", Phys. Rev. B **73** (2006) 132104.

[16] H.Y. Gou, L. Hou, J.W. Zhang, and F.M. Gao, "*Pressured-induced incompressibility of ReC and effect of metallic bonding on its hardness*", Appl. Phys. Lett. **92** (2008) 24190.

[17] S. Li, R. Ahuja, M.W. Barsoum, P. Jena, and B. Johansson, "*Optical properties of Ti_3SiC_2 and Ti_4AlN_3*," Appl. Phys. Lett. **92** (2008) 221907.

[18] R. Saniz, L.H. Ye, T. Shishidou, and A. Freeman, "*Structural, electronic, and optical properties of $NiAl_3$: First-principles calculations*", J Phys. Rev. **B 74** (2006) 014209.

[19] M.A. Blanco, E. Francisco, and V. Luana, "*GIBBS: isothermal-isobaric thermodynamics of solids from energy curves using a quasi-harmonic Debye model*", Comp. Phys. Comm. **158** (2004) 57.

[20] A.A. Maradudin, E.W. Montroll, G.H. Weiss, I.P. Ipatova, "*Theory of Lattice Dynamics in the harmonic Approximation*", Academic Press, 1971.

[21] M. Flórez, J.M. Recio, E. Francisco, M.A. Blanco, and A.M. Pendás, "*First-principles study of the rocksalt-cesium chloride relative phase stability in alkali halides*", Phys. Rev. B **66** (2002) 144112.

[22] M.A. Blanco, A.M. Pendás, and E. Francisco, "*Thermodynamical properties of solids from microscopic theory: Applications to MgF_2 and Al_2O_3*", J. Mol. Struct. (Theochem) **368** (1996) 245.

5. Computational tools

The aim of this chapter is to provide an overview of the different computational tools used in present investigation. We have carried out the first-principles calculations of structural, elastic, electronic and optical properties of some superconducting MAX phases using CASTEP code. The thermodynamic properties are investigated by implementation of Gibbs program along with the third-order Birch-Murnaghan equation of state (EOS). The salient features of these tools are given from next section.

5.1 Cambridge serial total energy package (CASTEP)

Cambridge serial total energy package abbreviated as CASTEP [1] is a state-of-the-art quantum mechanics-based program designed specifically for solid-state materials science. CASTEP employs the density functional theory plane-wave pseudopotential method, which allows us to perform first-principles quantum mechanics calculations that explore the properties of crystals and surfaces in materials such as semiconductors, ceramics, metals, minerals, and zeolites.

Typical applications involve studies of surface chemistry, structural properties, band structure, density of states, and optical properties. CASTEP can also be used to study the spatial distribution of the charge density and wave functions of a system. In addition, one can use CASTEP to calculate the full tensor of second-order elastic constants and related mechanical properties of a crystal (Poisson ratio, Lame constants, bulk modulus). The transition-state searching tools in CASTEP enable us to study chemical reactions in either the gas phase or on the surface of a material using linear synchronous transit/quadratic synchronous transit technology. These tools can also be used to investigate bulk and surface diffusion processes. CASTEP can also be used effectively to study the properties of both point defects (vacancies, interstitials, and substitutional impurities) and extended defects (for example the grain boundaries and the dislocations) in semiconductors and other materials.

Furthermore, the vibrational properties of solids (phonon dispersion, total and projected density of phonon states, thermodynamic properties) can be calculated with the CASTEP using either the linear response methodology or the finite displacements technique. The results can be used in various ways, for instance, to investigate the vibrational properties of adsorbents on surfaces, to interpret the experimental neutron spectroscopy data or the vibrational spectra, to study the phase stability at the high temperatures and pressures, etc. The linear response method can also be used to calculate the response of a material to an applied electric field - polarizability for molecules and dielectric permittivity in solids - and to predict IR spectra. Again, CASTEP can be used to calculate the properties required to analyze the results of the solid-state NMR experiments, i.e., chemical shifts and electric field gradients on atoms of interest.

The CASTEP STM analysis tool allows one to model scanning tunneling microscopy images at different bias voltages in order to solve the surface structures based on the experimental STM images.

5.2 Gibbs program

Given the energy of a solid (E) as a function of the molecular volume (V), the Gibbs program [2] uses a quasi-harmonic Debye model to generate the Debye temperature $\Theta(V)$, obtains the non-equilibrium Gibbs function $G^*(V; p, T)$, and minimizes G^* to derive the thermal equation of state (EOS) $V(p, T)$ and the chemical potential $G(p, T)$ of the corresponding phase. The other macroscopic properties are also derived as a function of p and T from standard thermodynamic relations. The program focuses on obtaining as much thermodynamical information as possible from a minimum set of (E, V) data, making it suitable to analyze the output of costly electronic structure calculations, adding thermal effects at a low cost for computation. Any of three analytical EOS widely used in the literature can be fitted to the $p-V$ (p, T) data, giving an alternative set of isothermal bulk moduli and their pressure derivatives that can be fed to the Debye model machinery.

5.3 Equation of States

On the theoretical side, the determination of the equation of state (EOS) and the chemical potential from first principles are two of the main objectives of the Physics and Chemistry of crystals. The EOS and the chemical potential are two of the key thermodynamic properties of a solid. The EOS of a given crystalline phase determines its behavior with respect to changes in the macroscopic variables, mainly pressure, *P* and temperature, *T*. Three EOS are incorporated in gibbs program to determine the thermodynamic properties of solids: the Vinet et al. EOS [3], the Birch–Murnaghan EOS [4,5], and the spinodal EOS [6]. In the present study, the third-order Birch-Murnaghan EOS is used to carry out the thermodynamic properties calculation.

Expressions for the third-order Birch-Murnaghan EOS

The Birch–Murnaghan isothermal equation of state, published in 1947 by Francis Birch [4], is a relationship between the volume of a body and the pressure to which it is subjected. This equation is named after Albert Francis Birch and Francis Dominic Murnaghan. Birch proposed this equation in a publication in 1947, based on the work of the Murnaghan published in 1944 [5]. The third-order Birch–Murnaghan isothermal equation of state is given by:

$$P(V) = \frac{3B_0}{2}\left[\left(\frac{V_0}{V}\right)^{7/3} - \left(\frac{V_0}{V}\right)^{5/3}\right]\left[1 + \frac{3}{4}(B_0' - 4)\left\{\left(\frac{V_0}{V}\right)^{2/3} - 1\right\}\right], \tag{5.1}$$

where P is the pressure, V_0 is the reference volume, V is the deformed volume, B_0 is the bulk modulus, and B'_0 is the derivative of the bulk modulus with respect to pressure. The bulk modulus and its derivative are usually obtained from fits to experimental data and are defined as

$$B_0 = -V\left(\frac{\partial P}{\partial V}\right)_{P=0} \quad \text{and} \quad B_0' = \left(\frac{\partial B}{\partial V}\right)_{P=0} \tag{5.2}$$

The internal energy, $E(V)$, is found by integration of the pressure:

$$E(V) = E_0 + \frac{9V_0B_0}{16}\left\{\left[\left(\frac{V_0}{V}\right)^{2/3} - 1\right]^3 B_0' + \left[\left(\frac{V_0}{V}\right)^{2/3} - 1\right]^2\left[6 - 4\left(\frac{V_0}{V}\right)^{2/3}\right]\right\} \tag{5.3}$$

References

[1] M. Segall, M. Probert, C. Pickard, P. Hasnip, S. Clark, K. Refson, J.R. Yates, and M. Payne, "*First principles methods using CASTEP*", Zeitschrift fuer Kristallographie **220** (2005) 567.

[2] M.A. Blanco, E. Francisco, and V. Luaña, "*GIBBS: isothermal-isobaric thermodynamics of solids from energy curves using a quasi-harmonic Debye model*", Comput. Phys. Commu. **158** (2004) 57.

[3] P. Vinet, J.H. Rose, J. Ferrante, J.R. Smith, "*Universal features of the equation of state of solids*", J. Phys. Condens. Matter. **1** (1989) 1941.

[4] F.D. Murnaghan, "*The Compressibility of Media under Extreme Pressures*", Proceedings of the National Academy of Sciences of the United States of America **30** (1944) 244.

[5] F. Birch, "*Finite Elastic Strain of Cubic Crystals*", Physical Review **71** (1947) 809.

[6] V. García Baonza, M. Cáceres, J. Núñez, "*Universal compressibility behavior of dense phases*", Phys. Rev. B **51** (1995) 28.

6. Results and discussions

In the present study, the first-principles calculations have been performed by using the pseudopotential plane-wave approach based on the density functional theory [1] implemented in the CASTEP (Cambridge Serial Total Energy Package) code [2]. The exchange-correlation potential is evaluated by using the generalized gradient approximation (GGA) with the functional developed by Perdew-Burke-Ernzerhof [3] known as the PBE scheme. Vanderbilt-type ultrasoft pseudopotentials [4] are employed to describe the electron-ion interactions. The energy cutoff of the plane-wave basis set is chosen as 500 eV to determine the number of plane waves in the expansion. For the Brillouin zone integration, the Monkhorst-Pack scheme [5] is used to produce a uniform grid of k-points along the three axes in reciprocal space and a 16 × 16 × 4 special k-points are taken to achieve geometry optimization for Nb_2AsC and Mo_2GaC, 10 × 10 × 2 for Nb_2InC, and 12 × 12 × 2 for Ti_2GeC. The Broyden-Fletcher-Goldfarb-Shanno (BFGS) minimization technique [6] is used to search the ground state of crystal and convergence tolerance is set to energy change below 5×10^{-6} eV/atom, force less than 0.01 eV/Å, stress less than 0.02 GPa, and change in atomic displacement less than 5×10^{-4} Å. To obtain the smooth shapes of the Fermi surfaces, we used 32 × 32 × 6, 35 × 35 × 9, 32 × 32 × 6, and 38 × 38 × 8 k-point mesh for Mo_2GaC, Nb_2AsC, Nb_2InC, and Ti_2GeC, respectively. To calculate the elastic constants, CASTEP uses the finite strain theory. In this approach, the elastic constants are determined from the first principles calculations by applying a set of given homogeneous deformations with a finite value and then by calculating the resultant stress with respect to the optimizing internal atomic coordinates.

The quasi-harmonic Debye model [7] implemented in the Gibbs program [7] is employed to determine the thermodynamic properties at ambient and elevated temperatures and pressures. In this investigation, we have used energy-volume data calculated from the third-order Birch-Murnahgan equation of state [8] using the zero temperature and zero pressure equilibrium values of energy, volume, and bulk modulus obtained through DFT calculations.

6.1 Structural properties

The MAX phases crystallize in the hexagonal structure with space group $P6_3/mmc$ (No. 194) and have eight atoms with two formula units in each unit cell. The structure is defined by two lattice constants a and c and the internal parameter z_M. The calculated lattice constants, internal free parameters, hexagonal ratios, and unit cell volumes for the four superconducting MAX phases Mo_2GaC, Nb_2AsC, Nb_2InC, and Ti_2GeC, as determined from geometry at zero pressure, are listed in Table 6.1a along with available theoretical [9-20] and experimental [21-28] values for comparison. Our results are in reasonable agreement with both theoretical and experimental values. The calculated lattice constants a and c for Mo_2GaC deviate from measured ones within 1.79 and 0.02%, respectively. For Nb_2AsC, the change from experimental values is 0.21 and 0.66%, whereas for Nb_2InC it is 0.44 and 1.09%, respectively. On the other hand, the lattice constants a and c of Ti_2GeC deviate not more than 0.48 and 0.25%, respectively. The calculated internal free parameter z_M for Mo_2GaC, Nb_2AsC, Nb_2InC, and Ti_2GeC is consistent with the values obtained in experiments and other first-principles calculations. The deviation from the experimental value of c/a for the four MAX superconducting phases is found to be 1.78, 0.42, 0.64, and 0.11%, respectively. The unit cell volume obtained in present investigation deviates from the experimental values for Mo_2GaC, Nb_2AsC, Nb_2InC, and Ti_2GeC within 3.63, 1.10, 2.15, and 1.20%, respectively.

To study the pressure effect on structural properties of these MAX compounds, the equilibrium geometries of Mo_2GaC, Nb_2AsC, Nb_2InC, and Ti_2GeC were investigated at the fixed values of applied hydrostatic pressure in the 0 – 50 GPa range with a step of 5 GPa, where at each pressure a complete optimization for the structural parameters was performed. In the present study, it is observed that no phase transition is occurred in these compounds within the pressure range. Indeed, it has been reported for Nb_2AsC [23] and the isostructural 211 MAX phases: Zr_2InC, Ti_2AlN, Ti_2AlC, Ti_2SC, V_2AlC, Cr_2AlC, Nb_2AlC, and Ta_2AlC that there is no phase transformation up to pressure ≈ 50 GPa [29-32]. The structural parameters calculated at different pressures for the four superconducting phases

are presented in Table 6.1b. The behavior of the lattice constants *a* and *c*, internal parameter z_M, hexagonal ratio *c*/*a* and unit cell volume *V* as a function of pressure is demonstrated in Figs. 6.1(a) – 6.1(e). It is observed that both lattice constants and unit cell volume decrease almost linearly with the increase of pressure. On the other hand, the hexagonal ratio increases gradually with increasing pressure, which implies that the lattice constant *a* decreases with a faster rate than *c*. Thus, the compressibility along c-axis is lower than that along the a-axis. This situation is reversed for $Ti_3Si_{0.5}Ge_{0.5}C_2$ [33], Ti_3SiC_2 [34], and Zr_2InC [29], where the compressibility along c-axis is higher than that along the a-axis. Interestingly, the internal parameter also increases in the same condition for all the phases. The relatively high z_M value for Nb_2AsC, the highest ever reported for a MAX phase, recall that the high z_M values enhance the M-A bonds at the expense of the M-X bonds. The MAX compound Nb_2AsC also combines relatively low *c* parameter with relatively high *a* parameter shown Tables 6.1a and Tables 6.1b. This result is consistent with the previous reports on S-, P-, and As-containing MAX phases [21]. Indeed, these three types of compounds are different from the rest of MAX phases. This observation implies that the Nb–As bonds in Nb_2AsC must be quite resistant to compression along the *c* axis [23].

In Figs. 6.1(f) – 6.1(h), we exhibit the normalized lattice constants a/a_o and c/c_o as well as the normalized volume V/V_o (where a_o, c_o, and V_o are the zero pressure equilibrium lattice constants and unit cell volume) together with the available theoretical and experimental values as a function of pressure. It is seen that, when pressure increases from 0 to 50 GPa, a decrease of a/a_o is found to be 7.28, 6.59, 6.80, and 7.16% for Mo_2GaC, Nb_2AsC, Nb_2InC, and Ti_2GeC, respectively, whereas for c/c_o it is 2.37, 3.37, 5.47, and 5.48%, respectively. The amount of decrease of normalized volume for the four phases is obtained as 16.09, 15.50, 17.88, and 18.51%, respectively. The phasewise relative change in structural properties a/a_o, c/c_o, and V/V_o are shown again in Figs. 6.1(i) – 6.1(*l*). The equation of states calculation is shown in Figs. 6.1(m) – 6.1(p).

Table 6.1a: Calculated lattice constants a_o and c_o (in Å), hexagonal ratio c_o/a_o, internal parameter z_M, unit cell volume V_o (in Å^3), bulk modulus (in GPa) and its pressure derivatives at zero pressure for superconducting MAX phases Mo_2GaC, Nb_2AsC, Nb_2InC, and Ti_2GeC using PBE-GGA with CASTEP code.

Phases	a_o	c_o	c_o/a_o	z_M	V_o	B	B'
Mo_2GaC- Present	3.064	13.178	4.301	0.0880	107.2	189.2	5.26
LDA-VASP [9]	3.068	13.153	4.287	0.0889	108.4	248.6	
PW91 GGA-VASP [10]	3.084	13.16	4.267		104.7	190.0	
PBE-GGA-WIENK2k [11]	3.042	13.064	4.195	0.0893	103.4	250.6	
PBE-GGA-VASP [12]	3.071	13.147	4.281		107.3	191.5	
Expt. [21]	3.01	13.18	4.379		103.4		
Nb_2AsC-Present	3.324	11.979	3.603	0.0945	114.6	207.7	4.72
LDA-VASP [9]	3.344	12.048	3.603	0.0944	116.7	234.3	
PW91-GGA-VASP [10]	3.339	12	3.594		115.6		
Calc. & Expt. [13]	3.3235	11.9036	3.582		113.9	209.0*	
Expt. [21]	3.31	11.9	3.595		112.9		
Expt. [22]	3.317	11.90	3.588	0.0980	113.4		
Expt. [23]	3.327	11.917	3.582	0.0955	114.2	224.0	4.00
Nb_2InC- Present	3.186	14.526	4.559	0.0820	127.9	154.7	4.80
LDA-VASP [9]	3.193	14.495	4.539	0.0819	128.0	182.4	
PW91-GGA-VASP [10]	3.196	14.47	4.528		128.0	182.4	
LDA-CASTEP [14]	3.137	14.280	4.552	0.0830	121.7	195.6	
PW91-GGA-CASTEP [15]	3.185	14.546	4.567	0.0822	127.8	156.4	
GGA-CASTEP [16]	3.189	14.470	4.538	0.0827	127.4	157.3	4.66
LDA-CASTEP [16]	3.144	14.242	4.530	0.0815	121.9	182.8	4.06
Expt. [21]	3.17	14.73	4.647		128.2		
Expt. [24]	3.172	14.37	4.530		125.2		
Ti_2GeC-Present	3.085	12.961	4.202	0.0891	106.8	158.6	4.10
LDA-CASTEP [17]	3.054	12.891	4.221	0.0903	104.2	160.0	4.36
LDA-CASTEP [18]	3.047	12.776	4.193	0.0915	102.7	173.0	3.86
GGA-WIEN2k [19]	3.09	13.04	4.220	0.0885	107.8	163.0	
PBE-GGA-CASTEP [20]	3.101	13.159	4.244		109.6		
Expt. [25]	3.079	12.930	4.199	0.0860	106.2		
Expt. [26]	3.07	12.93	4.212		105.5		
Expt. [27]	3.078	12.934	4.202		106.1	211.0	3.90
Expt. [28]	3.081	12.929	4.197	0.0953	106.3		

*Calculated

Table 6.1b: Calculated lattice parameters (a and c), hexagonal ratio (c/a) internal parameter (z_M) and unit cell volume (V) at different pressure.

Phases	Pressure	a (Å)	c (Å)	a/c	z_M	V (Å^3)
Mo_2GaC	0	3.085	12.961	4.201	0.0891	106.815
	5	3.053	12.843	4.207	0.0899	103.683
	10	3.025	12.745	4.213	0.0905	100.985
	15	2.999	12.662	4.222	0.0910	98.609
	20	2.975	12.590	4.232	0.0915	96.483
	25	2.953	12.524	4.241	0.0919	94.552
	30	2.932	12.463	4.251	0.0923	92.802
	35	2.913	12.406	4.259	0.0927	91.186
	40	2.896	12.352	4.265	0.0929	89.704
	45	2.880	12.301	4.271	0.0932	88.329
	50	2.864	12.251	4.278	0.0934	87.047
Nb_2AsC	0	3.324	11.979	3.604	0.0945	114.638
	5	3.292	11.927	3.623	0.0950	111.925
	10	3.265	11.870	3.636	0.0954	109.611
	15	3.241	11.819	3.647	0.0958	107.537
	20	3.219	11.771	3.657	0.0961	105.641
	25	3.199	11.728	3.666	0.0964	103.972
	30	3.179	11.695	3.679	0.0966	102.342
	35	3.159	11.666	3.693	0.0969	100.813
	40	3.141	11.635	3.704	0.0971	99.388
	45	3.125	11.601	3.712	0.0973	98.112
	50	3.109	11.575	3.723	0.0974	96.871
Nb_2InC	0	3.192	14.498	4.542	0.0817	127.913
	5	3.164	14.353	4.536	0.0826	124.456
	10	3.134	14.247	4.546	0.0834	121.199
	15	3.107	14.157	4.556	0.0841	118.388
	20	3.084	14.074	4.564	0.0847	115.902
	25	3.062	13.998	4.572	0.0852	113.681
	30	3.043	13.929	4.577	0.0856	111.667
	35	3.024	13.865	4.585	0.0860	109.821
	40	3.007	13.807	4.592	0.0864	108.118
	45	2.991	13.754	4.598	0.0867	106.530
	50	2.975	13.705	4.607	0.0870	105.036
Ti_2GeC	0	3.085	12.961	4.201	0.0891	106.815
	5	3.053	12.843	4.207	0.0899	103.683
	10	3.025	12.745	4.213	0.0905	100.985
	15	2.999	12.662	4.222	0.0910	98.609
	20	2.975	12.590	4.232	0.0915	96.483
	25	2.953	12.524	4.241	0.0919	94.552
	30	2.932	12.463	4.251	0.0923	92.802
	35	2.913	12.406	4.259	0.0927	91.186
	40	2.896	12.352	4.265	0.0929	89.704
	45	2.880	12.301	4.271	0.0932	88.329
	50	2.864	12.251	4.278	0.0934	87.047

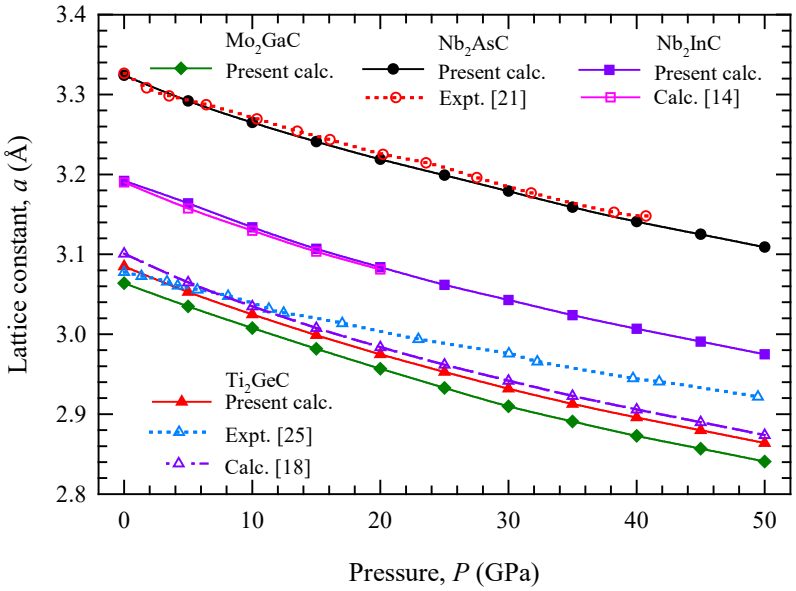

Fig. 6.1(a). Pressure dependence of lattice constant *a* for superconducting MAX phases Mo_2GaC, Nb_2AsC, Nb_2InC, and Ti_2GeC.

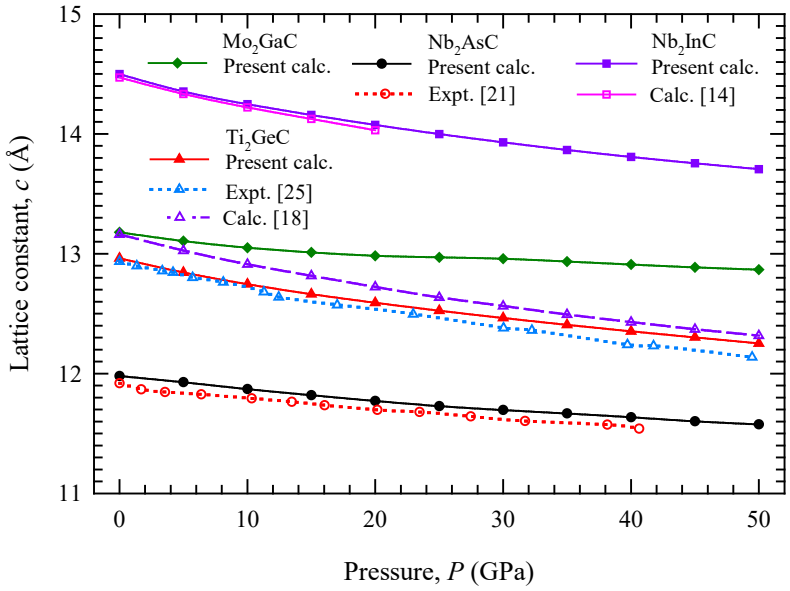

Fig. 6.1(b). Pressure dependence of lattice constant *c* for superconducting MAX phases Mo_2GaC, Nb_2AsC, Nb_2InC, and Ti_2GeC.

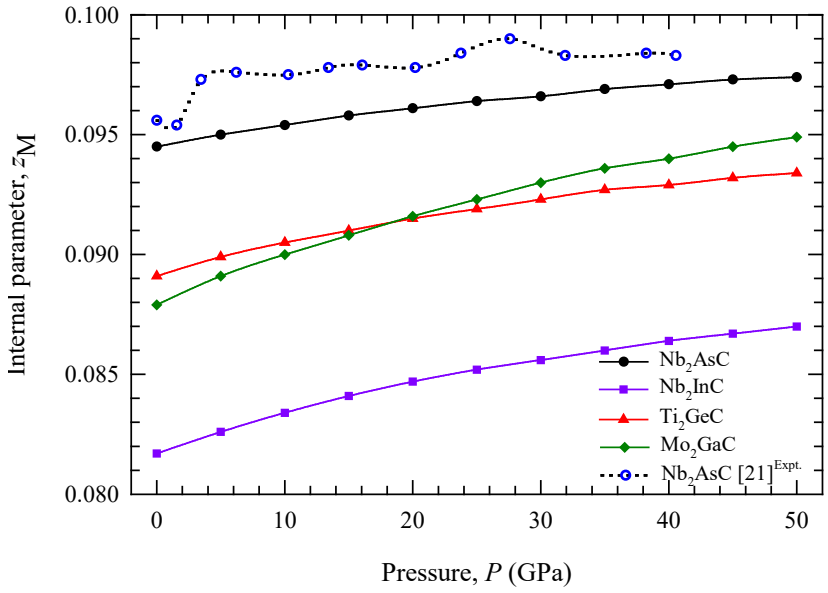

Fig. 6.1(c). Pressure dependence of internal parameter z_M for superconducting MAX phases Mo_2GaC, Nb_2AsC, Nb_2InC, and Ti_2GeC.

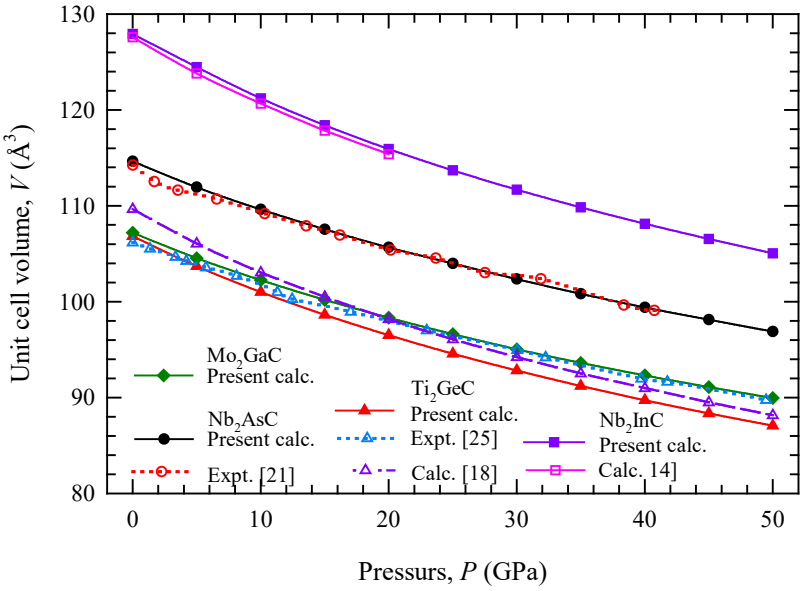

Fig. 6.1(d). Pressure dependence of unit cell volume V for superconducting MAX phases Mo_2GaC, Nb_2AsC, Nb_2InC, and Ti_2GeC.

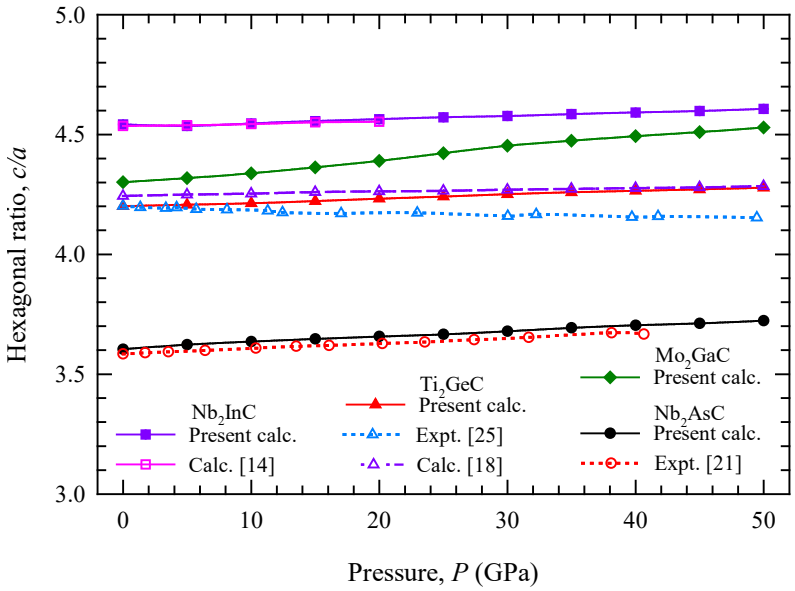

Fig. 6.1(e). Pressure dependence of hexagonal ratio c/a for superconducting MAX phases Mo_2GaC, Nb_2AsC, Nb_2InC, and Ti_2GeC.

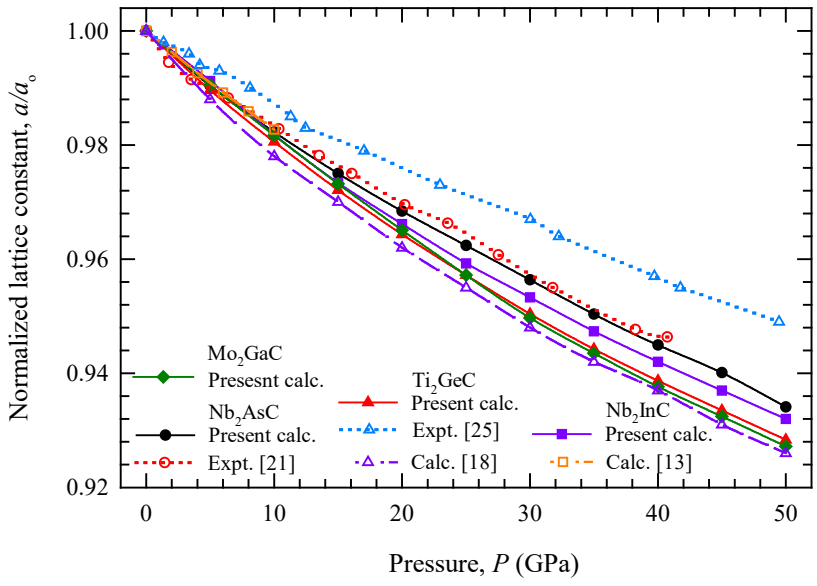

Fig. 6.1(f). Pressure dependence of normalized lattice constant a/a_o for four superconducting MAX phases Mo_2GaC, Nb_2AsC, Nb_2InC, and Ti_2GeC.

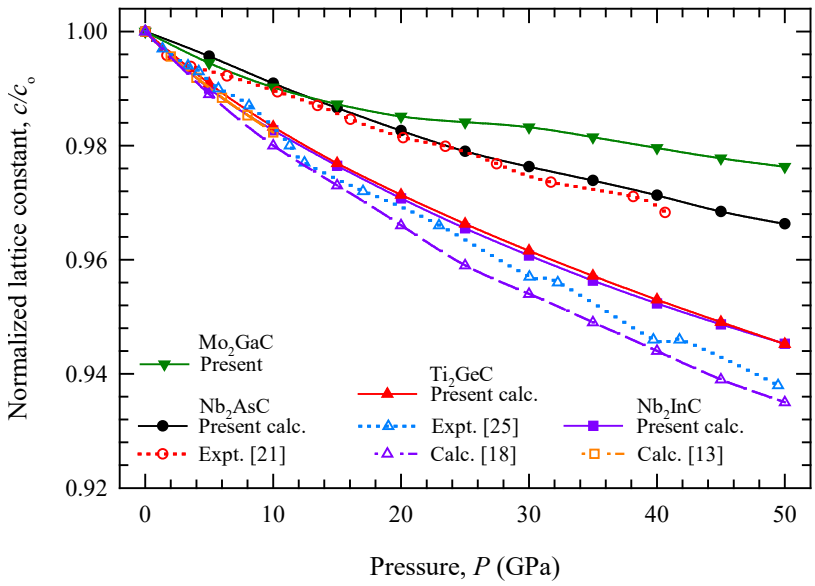

Fig. 6.1(g). Pressure dependence of normalized lattice constant c/c_o for four superconducting MAX phases Mo_2GaC, Nb_2AsC, Nb_2InC, and Ti_2GeC.

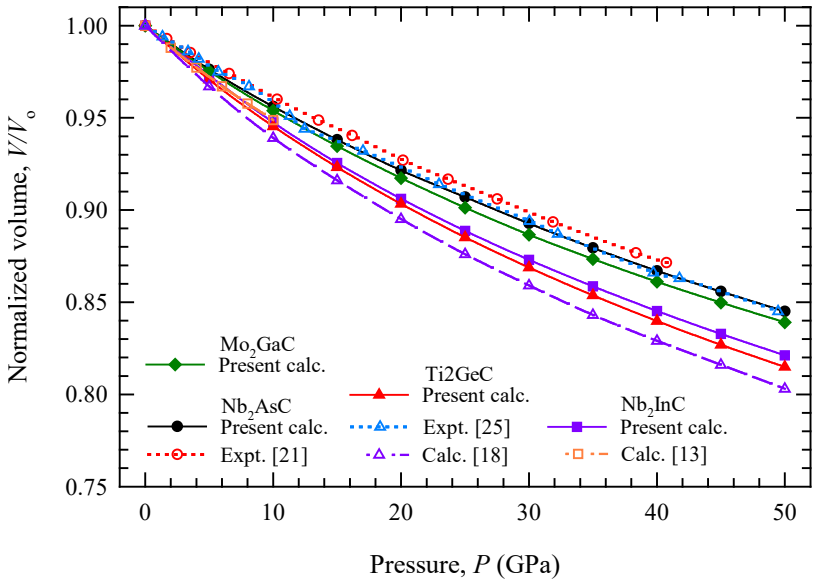

Fig. 6.1(h). Pressure dependence of normalized unit cell volume V/V_o for four superconducting MAX phases Mo_2GaC, Nb_2AsC, Nb_2InC, and Ti_2GeC.

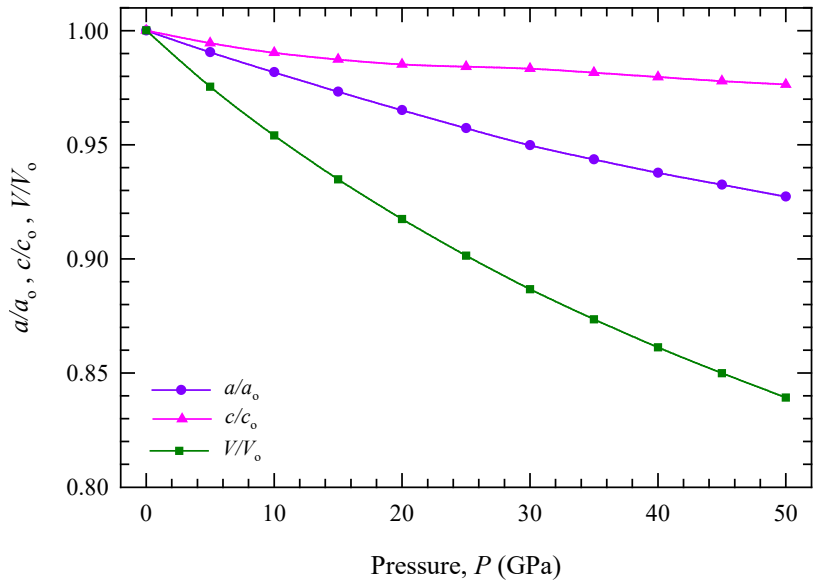

Fig. 6.1(i). Pressure dependence of normalized lattice constants a/a_o and c/c_o and unit cell volume V/V_o for MAX phase Mo_2GaC.

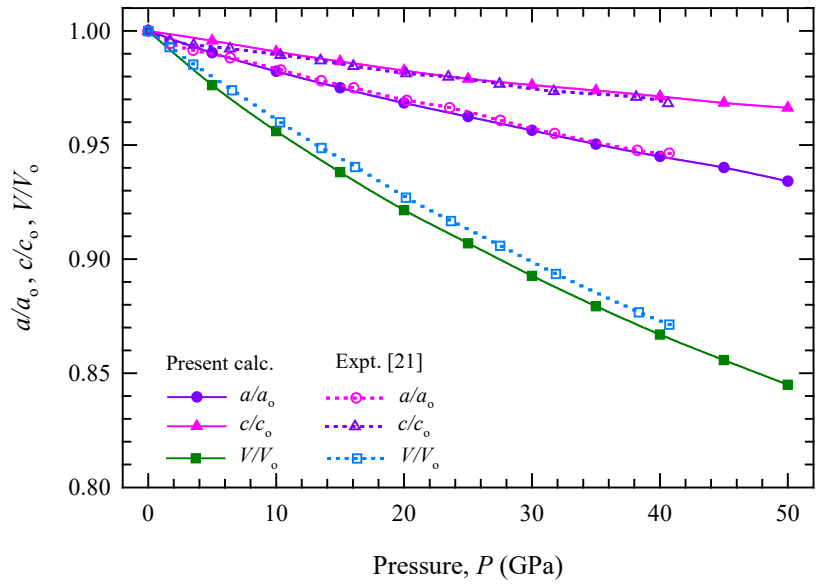

Fig. 6.1(j). Pressure dependence of normalized lattice constants a/a_o and c/c_o and unit cell volume V/V_o for MAX phase Nb_2AsC.

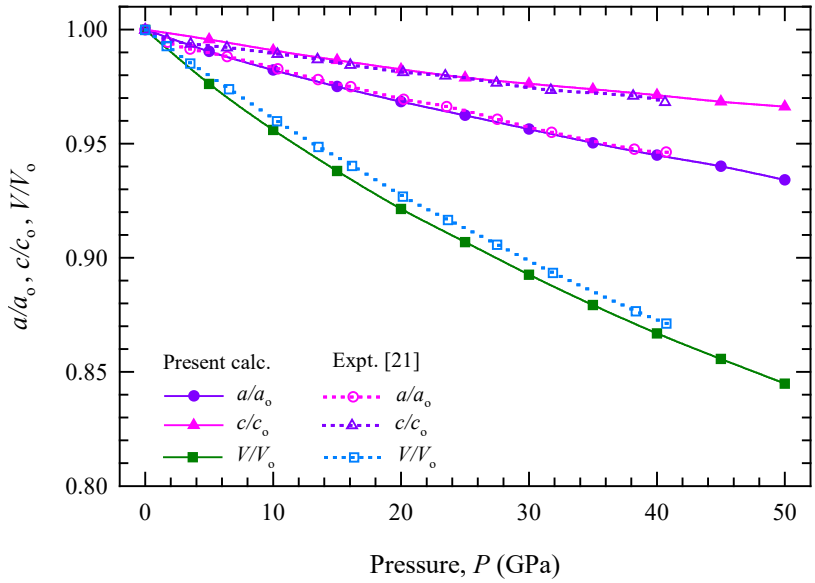

Fig. 6.1(k). Pressure dependence of normalized lattice constants a/a_o and c/c_o and unit cell volume V/V_o for MAX phase Nb_2InC.

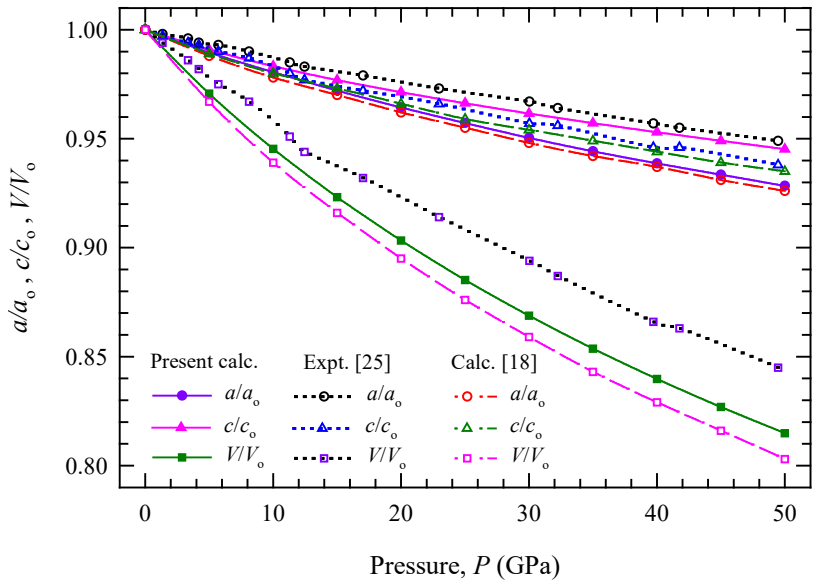

Fig. 6.1(*l*). Pressure dependence of normalized lattice constants a/a_o and c/c_o and unit cell volume V/V_o for MAX phase Ti_2GeC.

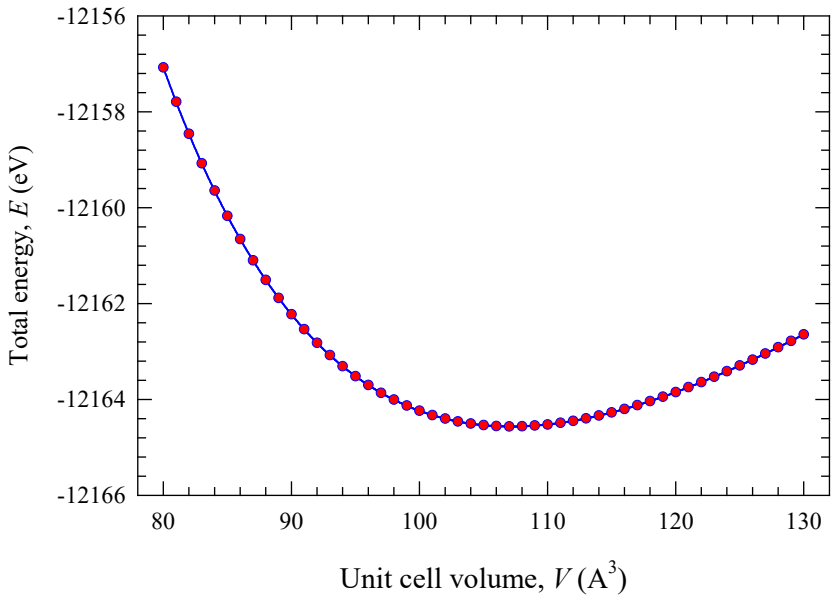

Fig. 6.1(m). Total energy as a function of unit cell volume for superconducting MAX phase Mo_2GaC.

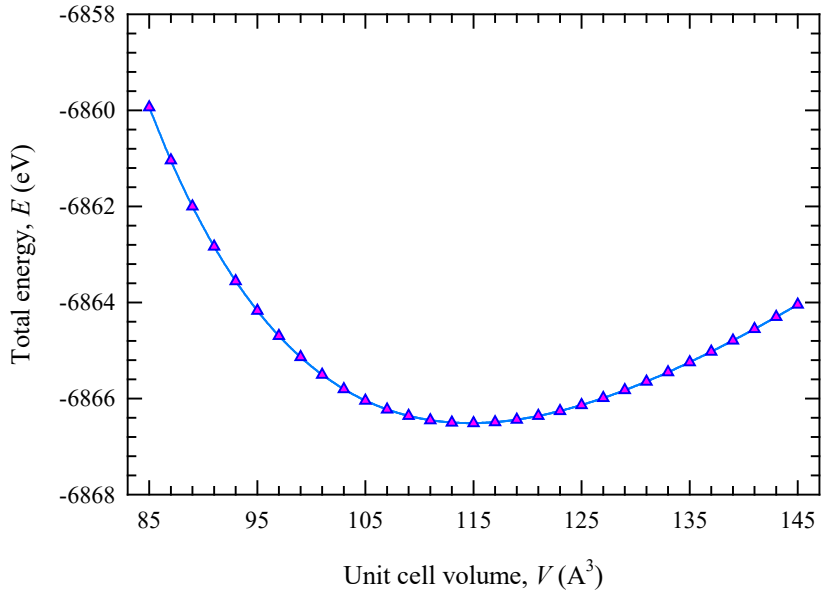

Fig. 6.1(n). Total energy as a function of unit cell volume for superconducting MAX phase Nb_2AsC.

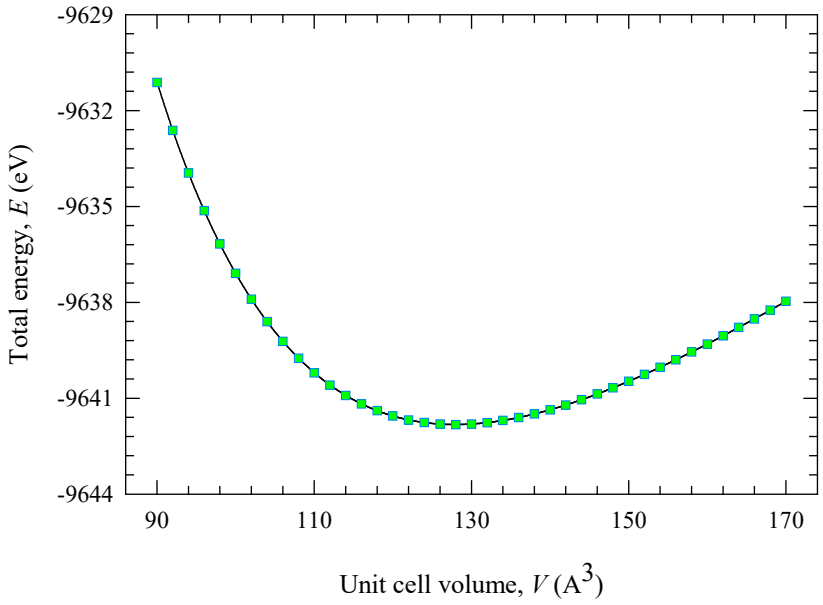

Fig. 6.1(o). Total energy as a function of unit cell volume for superconducting MAX phase Nb_2InC.

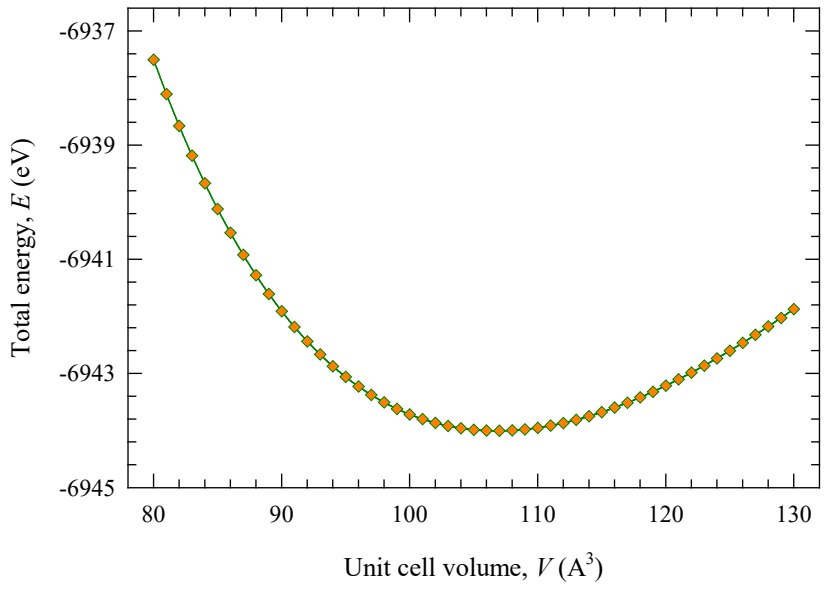

Fig. 6.1(p). Total energy as a function of unit cell volume for superconducting MAX phase Ti_2GeC.

6.2 Elastic properties

Elastic properties of solids are closely related to many fundamental solid state properties, such as equation of states, specific heat, thermal expansion, Debye temperature, Gruneisen parameter, and melting point. From elastic constants, one can obtain valuable information about the bonding characteristics between adjacent atomic planes, the anisotropic character of the bonding, and the structural stability. As polycrystalline material every MAX compound can be treated as an aggregate of single crystals at random orientation. Both single crystal elastic constants and elastic properties of polycrystalline aggregate will be discussed in the next sections for the selected four superconducting MAX phases.

6.2.1 Single crystal elastic constants

Single crystal elastic constants of the selected superconducting MAX phases Mo_2GaC, Nb_2AsC, Nb_2InC and Ti_2GeC are evaluated at 0 K temperature and 0 GPa pressure from first-principles calculations. As hexagonal crystal all MAX phases have six different elastic constants C_{11}, C_{12}, C_{13}, C_{33}, C_{44} and C_{66}, and only five of them are independent because $C_{66} = (C_{11} - C_{12})/2$. In Table 6.2.1a, the calculated elastic constants at zero pressure are listed along with available other theoretical results for comparison. It is seen that our results are consistent with the previous reported values [9-18,20]. The elastic anisotropy of a crystal is the orientation dependence of the elastic moduli or sound velocities. A proper description of such an anisotropic behavior has an important implication in engineering science as well as in crystal physics. To quantify the elastic anisotropy of the studied MAX compounds with the hexagonal structure, we have evaluated the shear anisotropic factor defined by $A = 4C_{44}/(C_{11} + C_{33} - 2C_{13})$. This factor is used as a measure of the degree of elastic anisotropy for the $\{1\ 0\ \bar{1}\ 0\}$ shear planes between the $\langle 0\ 1\ \bar{1}\ 1\rangle$ and $\langle 0\ 1\ \bar{1}\ 0\rangle$ directions that is identical to the shear anisotropy factor for the $\{0\ 1\ \bar{1}\ 0\}$ shear planes between $\langle 1\ 0\ \bar{1}\ 1\rangle$ and $\langle 0\ 0\ 0\ 1\rangle$ directions. The calculated shear anisotropic factors are presented in Table 6.2.1a along with other results. For an isotropic crystal, A must be equal to unity and that any value of A either smaller or

greater than unity indicates elastic anisotropy. The magnitude of the deviation from unity is a measure of the degree of elastic anisotropy possessed by the crystal. According to the present as well as the previous results (excepting that obtained in literature [9] for Nb_2InC phase) Nb_2InC and Ti_2GeC possess small anisotropy for the shear planes described above. This small anisotropy indicates that the in-plane and out-of-plane inter-atomic interactions in these nanolaminates differ slightly. Other two phases achieve comparatively more elastic anisotropy since they exhibit the maximal deviation from unity. Yet another elastic anisotropy parameter defined by the ratio between linear compressibility coefficients along the c and a axis for the hexagonal crystal is $k_c/k_a = (C_{11} + C_{12} - 2C_{13})/(C_{33} - C_{13})$. The unit value of this parameter implies that the compressibility along both directions is same i.e., the crystal is isotropic. Any value less (greater) than unity indicates the compressibility along the c axis is smaller (larger) than that along the a-axis. Our results agree well with other values [9-13,16,18,20] excepting that found in calculations for Nb_2InC [14,15] and Ti_2GeC [17] and reveal that the compressibility along the c axis is slightly less than that along the a axis for all the four phases. This factor also indicates that studied four compounds are characterized by a small anisotropy.

The calculated elastic constants at different pressures are listed in Table 6.2.1b. Figures 6.2(a) – 6.2(t) represent the monotonous increase of the five independent elastic constants C_{ij} with pressure up to 50 GPa along with the earlier theoretical results [15,16,18,21] for comparison. It is worth mentioning that certain pressure dependent elastic constants of Nb_2AsC show (e.g., Fig. 6.2.1 (g)) non-monotonic behavior. To check the results, we have repeated the calculations for these cases with different cut-off parameters and different optimization criteria. But, the non-monotonic behavior persists in every case. Experimentally, Nb_2AsC was found to be structurally stable within the pressure range 0 – 41 GPa [23]. Moreover, it has been reported for some isostructural 211 MAX phases that there is no phase transformation up to ≈ 50 GPa [29-32]. Therefore, this non-monotonic behavior is probably not related to any possible tendency towards structural instability. Further study is required to explain this interesting behavior.

For the phases Mo_2GaC and Nb_2AsC there is not found any data on elastic constants in the literature for comparison. The present results for the phase Nb_2InC are very close to an earlier study [16]. The results from previous study [15] are somewhat greater than those found in both present and early work [16] excepting C_{13}. There are available two calculated results [18,21] for the compound Ti_2GeC. The value obtained in the present calculations for the elastic constants, C_{11}, C_{12}, and C_{13} of Ti_2GeC agrees well with the results found in literature [18]. Moreover, the elastic constants C_{33} and C_{44} of the present study show almost average of the both early calculations [18,21].

For the MAX phases with the hexagonal crystal structure, the mechanical stability under the isotropic pressure is verified from the following well-established Born criteria [35]:

$C_{11} > 0$, $C_{33} > 0$, $C_{44} > 0$, $(C_{11} - C_{12}) > 0$, and $(C_{11} + C_{12})\, C_{33} > 2C_{13}^2$.

The calculated elastic constants at different pressures shown in Table 6.2.1b and Figs. 6.2.1(a) – 6.2.1(t) are positive and satisfy the all above conditions. Even within the pressure range 5 – 25 GPa, in which some elastic constants of Nb_2AsC showing the non-monotonic behavior, the Born mechanical stability criteria are fully valid. These suggest that the four superconducting 211 MAX phases are mechanically stable under the applied pressure and predicts that there is no a phase transition under the pressure range from 0 to 50 GPa.

It is observed that, when pressure increases from 0 to 50 GPa, a increase of C_{11} is found to be 70, 78, 95, and 78% for Mo_2GaC, Nb_2AsC, Nb_2InC, and Ti_2GeC, respectively, whereas for C_{12} the respective figures are 221, 110, 220, and 232%. The rate of increase for C_{13} is seen to be 143, 133, 180, and 178%, respectively. The elastic constant C_{33} for the four superconducting MAX phases increases by 99, 66, 155, and 94%, whereas C_{44} increases by 94, 83, 92, and 91%, respectively. It can be seen that the elastic constants C_{12} and C_{13} are more sensitive to pressure than other three constants.

Table 6.2.1a: Calculated elastic constants* C_{ij} (in GPa) as well as the shear anisotropic factors A and k_c/k_a at 0 K temperature and 0 GPa pressure for four superconducting MAX phases Mo_2GaC, Nb_2AsC, Nb_2InC, and Ti_2GeC using PBE-GGA with CASTEP code.

Phases	C_{11}	C_{12}	C_{13}	C_{33}	C_{44}	A	k_c/k_a
Mo_2GaC - Present	301	91	157	303	126	1.74	0.53
LDA-VASP [9]	306	105	169	311	102	1.46	0.52
PW91-GGA-VASP [10]	294	98	160	289	127	1.93	0.56
PBE-GGA-WIENK2k [11]	306	101	169	303	102	1.50	0.52
PBE-GGA-VASP [12]	312	94	164	314	128	1.72	0.52
Nb_2AsC - Present	334	113	159	346	168	1.86	0.69
LDA-VASP [9]	325	114	161	326	150	1.83	0.71
PW91-GGA-VASP [10]	327	108	155	347	162	1.78	0.65
Calc. [13]	334	104	169	331	167	2.04	0.62
Nb_2InC - Present	283	70	107	259	105	1.28	0.91
LDA-VASP [9]	291	77	118	289	57	0.66	0.78
PW91-GGA-VASP [10]	291	76	108	267	102	1.19	0.95
LDA-CASTEP [14]	363	103	131	306	148	1.45	1.17
PW91-GGA-CASTEP [15]	303	76	99	256	100	1.11	1.15
GGA-CASTEP [16]	287	74	107	265	104	1.23	0.93
LDA-CASTEP [16]	329	90	128	298	119	1.27	0.96
Ti_2GeC - Present	301	72	94	307	131	1.25	0.87
LDA-CASTEP [17]	279	99	95	283	125	1.34	1.00
LDA-CASTEP [18]	309	84	105	321	143	1.35	0.85
PBE-GGA-CASTEP [20]	281	81	99	294	122	1.25	0.84

.*All elastic constants are shown in round figures.

Table 6.2.1b: Calculated single crystal elastic properties C_{ij} (in GPa), and anisotropy factors A and k_c/k_a at different pressure for superconducting four MAX phases.

Phases	Pressure	C_{11}	C_{12}	C_{13}	C_{33}	C_{44}	A	k_c/k_a
Mo_2GaC	0	301	91	157	303	126	1.7379	0.5342
	5	333	109	182	339	141	1.8312	0.4968
	10	358	116	210	375	160	2.0447	0.3273
	15	382	127	235	403	180	2.2857	0.2321
	20	407	148	263	430	186	2.3923	0.1737
	25	423	160	289	460	198	2.5967	0.0292
	30	445	188	304	495	201	2.4217	0.1309
	35	477	216	320	531	211	2.2935	0.2512
	40	489	255	334	557	223	2.3598	0.3408
	45	506	273	356	583	233	2.4721	0.2952
	50	511	292	381	604	244	2.7649	0.1839
Nb_2AsC	0	334	113	159	346	168	1.8564	0.6898
	5	353	127	190	377	184	2.1029	0.5348
	10	363	161	208	391	200	2.3669	0.5902
	15	398	161	229	411	215	2.4501	0.5549
	20	399	209	251	425	227	2.8199	0.6092
	25	429	204	272	449	241	2.8862	0.5028
	30	488	188	295	475	254	2.7239	0.4778
	35	518	199	301	467	268	2.7990	0.6928
	40	547	210	326	501	283	2.8586	0.6000
	45	571	223	355	547	296	2.9020	0.4375
	50	593	237	371	573	307	2.8962	0.4356
Nb_2InC	0	283	70	107	259	105	1.2805	0.9145
	5	306	89	132	294	112	1.3333	0.8086
	10	336	102	153	331	123	1.3629	0.7416
	15	370	120	171	366	134	1.3604	0.7590
	20	414	128	191	403	149	1.3701	0.7547
	25	447	144	207	432	159	1.3677	0.7867
	30	476	157	226	463	169	1.3881	0.7637
	35	501	171	246	489	177	1.4217	0.7407
	40	524	184	264	513	183	1.4381	0.7229
	45	545	198	283	536	191	1.4835	0.6996
	50	553	224	300	558	202	1.5812	0.6860
Ti_2GeC	0	301	72	94	307	131	1.2476	0.8685
	5	327	86	114	331	143	1.3302	0.8525
	10	352	98	137	361	159	1.4487	0.7857
	15	373	112	158	386	170	1.5350	0.7412
	20	385	132	179	412	183	1.6674	0.6824
	25	409	150	196	437	195	1.7181	0.6929
	30	433	167	209	465	207	1.7250	0.7109
	35	459	184	222	499	218	1.6965	0.7184
	40	485	202	233	531	228	1.6582	0.7416
	45	509	221	247	564	239	1.6511	0.7445
	50	537	239	261	596	250	1.6367	0.7582

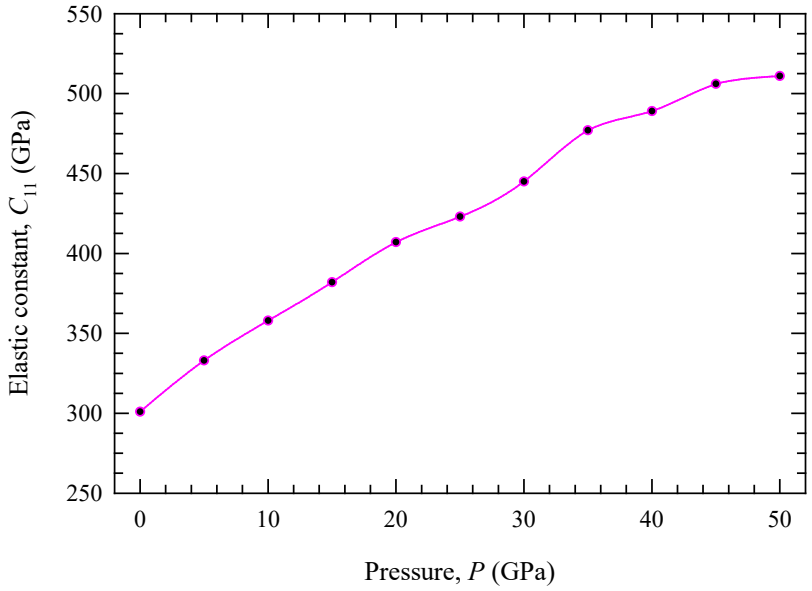

Fig. 6.2.1(a). Pressure dependence of elastic constant C_{11} of superconducting MAX phase Mo_2GaC.

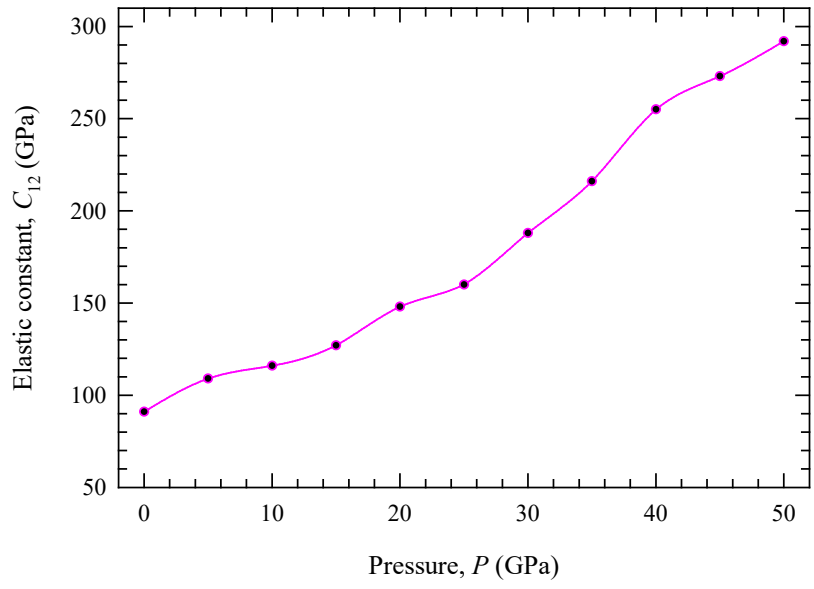

Fig. 6.2.1(b). Pressure dependence of elastic constant C_{12} of superconducting MAX phase Mo_2GaC.

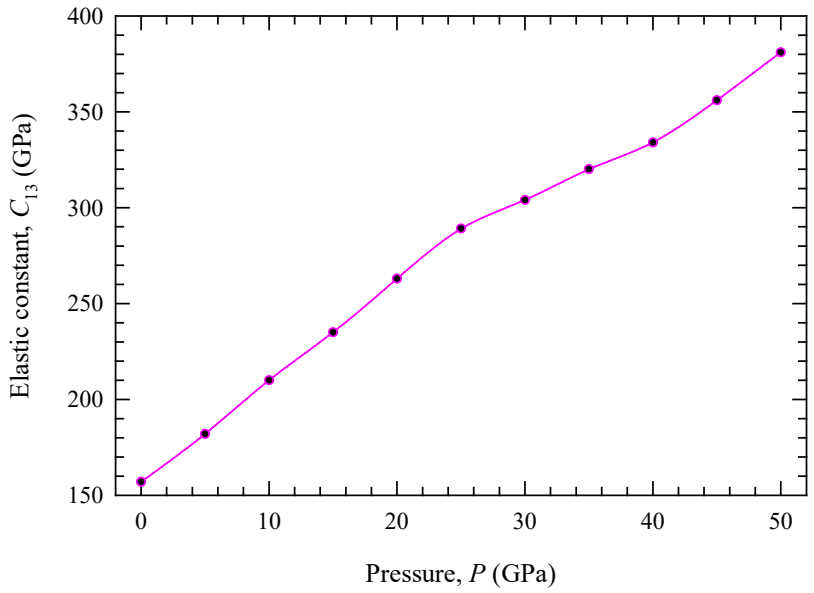

Fig. 6.2.1(c). Pressure dependence of elastic constant C_{13} of superconducting MAX phase Mo_2GaC.

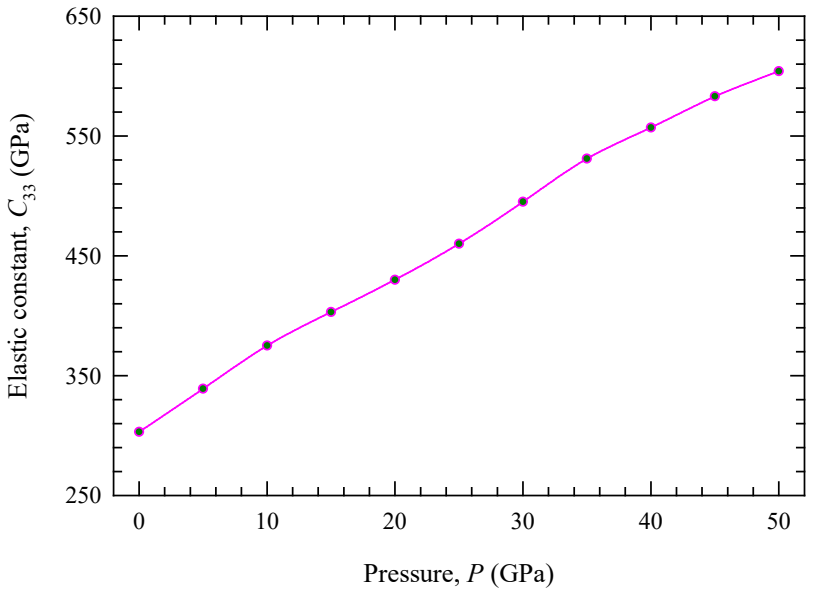

Fig. 6.2.1(d). Pressure dependence of elastic constant C_{33} of superconducting MAX phase Mo_2GaC.

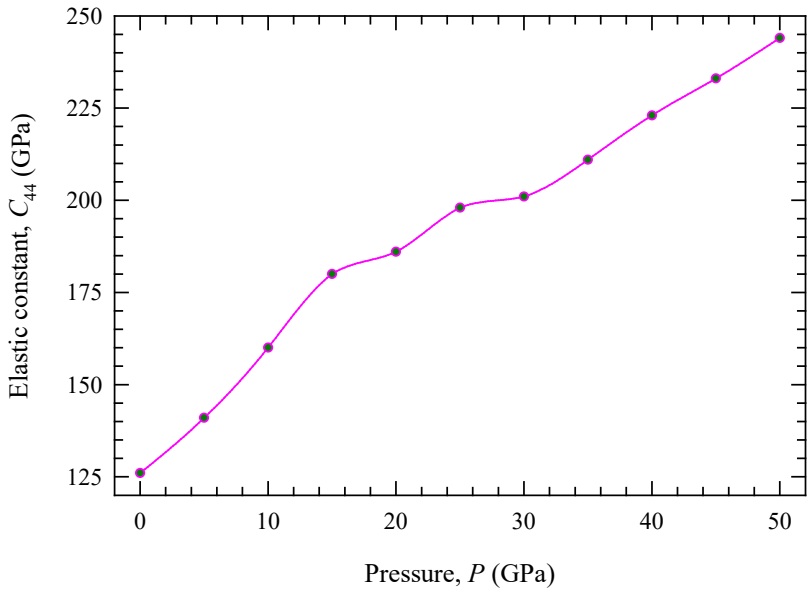

Fig. 6.2.1(e). Pressure dependence of elastic constant C_{44} of superconducting MAX phase Mo_2GaC.

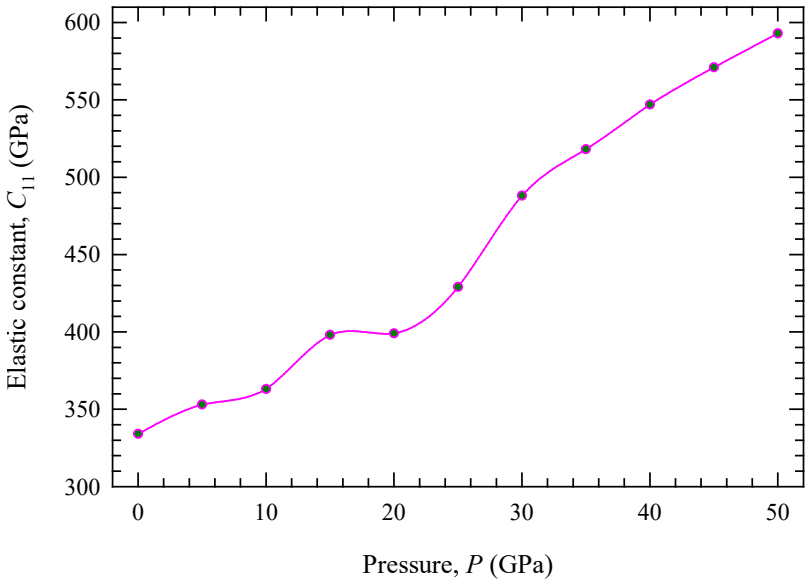

Fig. 6.2.1(f). Pressure dependence of elastic constant C_{11} of superconducting MAX phase Nb_2AsC.

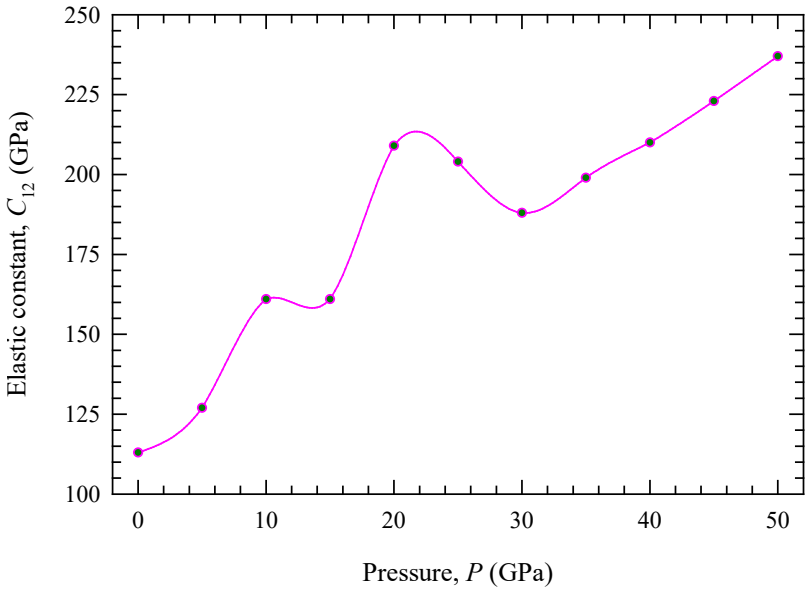

Fig. 6.2.1(g). Pressure dependence of elastic constant C_{12} of superconducting MAX phase Nb_2AsC.

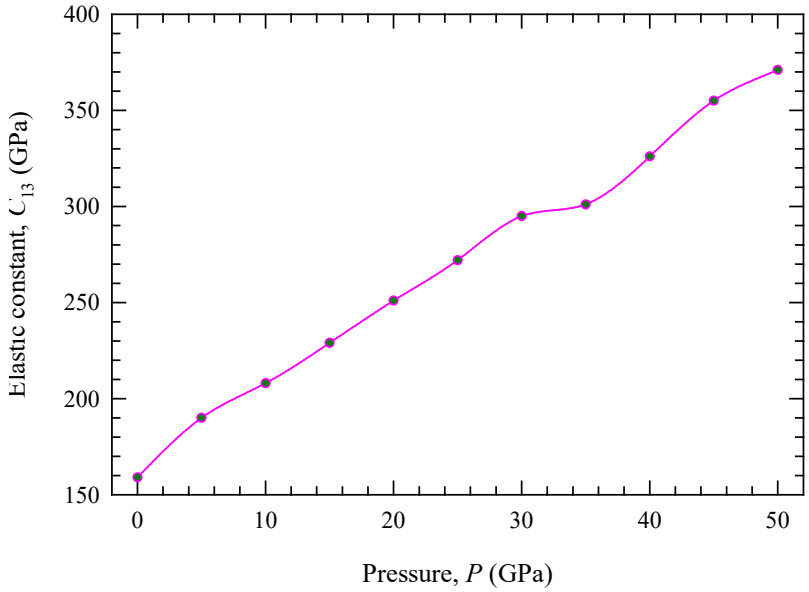

Fig. 6.2.1(h). Pressure dependence of elastic constant C_{13} of superconducting MAX phase Nb_2AsC.

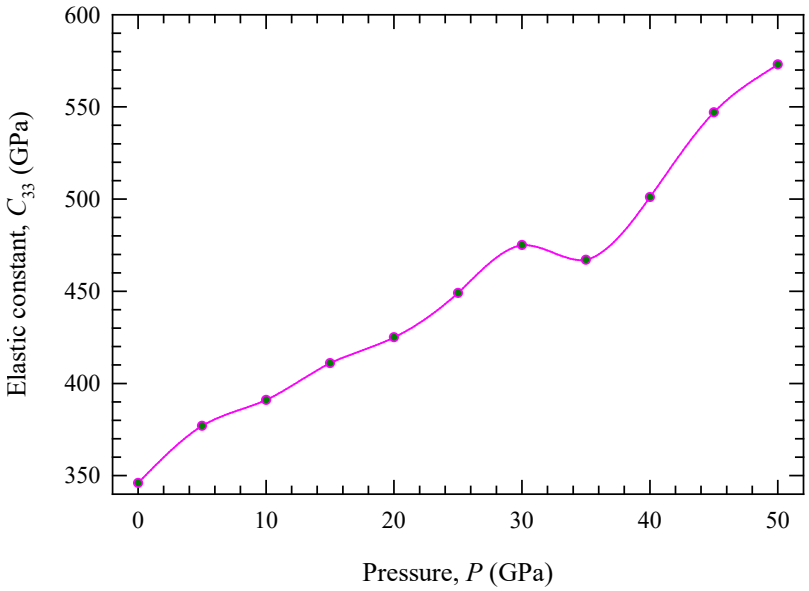

Fig. 6.2.1(i). Pressure dependence of elastic constant C_{33} of superconducting MAX phase Nb_2AsC.

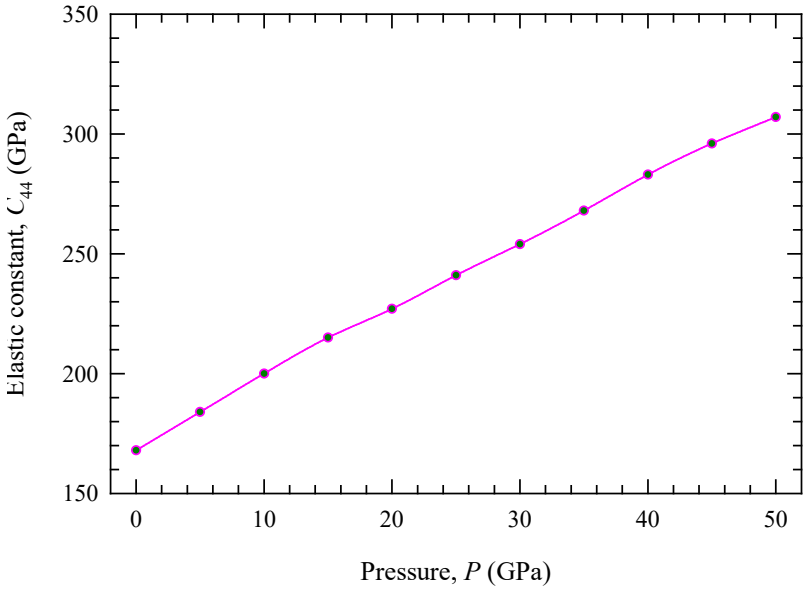

Fig. 6.2.1(j). Pressure dependence of elastic constant C_{44} of superconducting MAX phase Nb_2AsC.

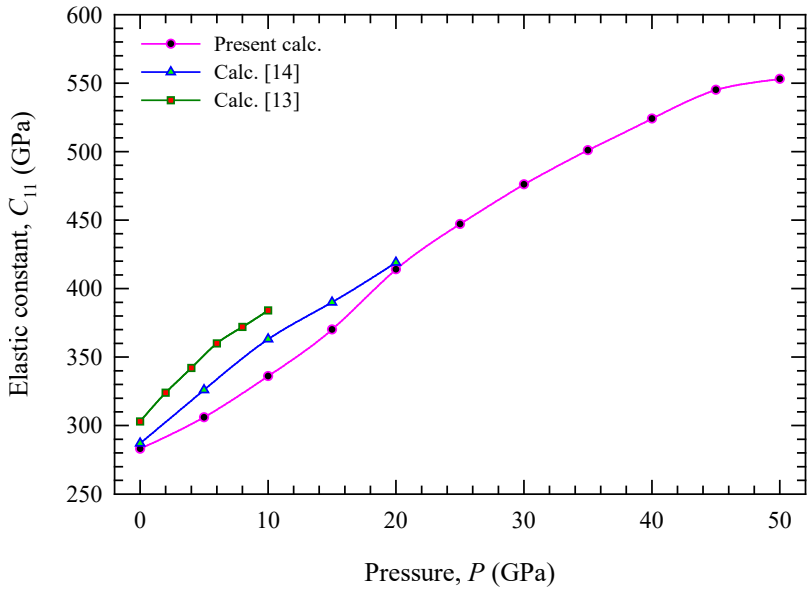

Fig. 6.2.1(k). Pressure dependence of elastic constant C_{11} of superconducting MAX phase Nb_2InC.

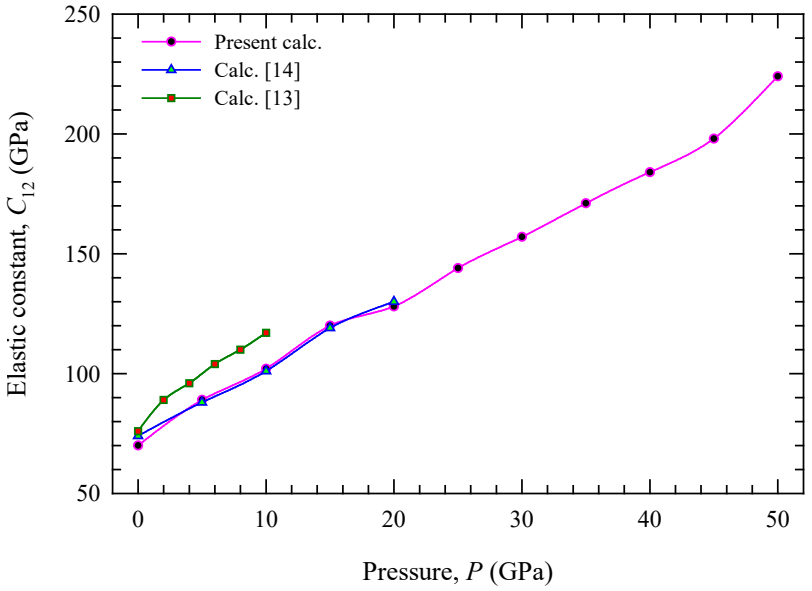

Fig. 6.2.1(*l*). Pressure dependence of elastic constant C_{12} of superconducting MAX phase Nb_2InC.

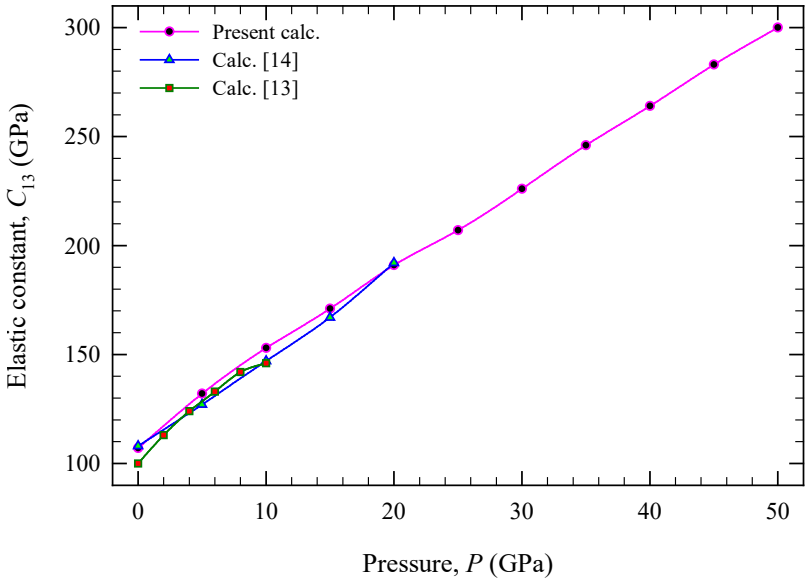

Fig. 6.2.1(m). Pressure dependence of elastic constant C_{13} of superconducting MAX phase Nb_2InC.

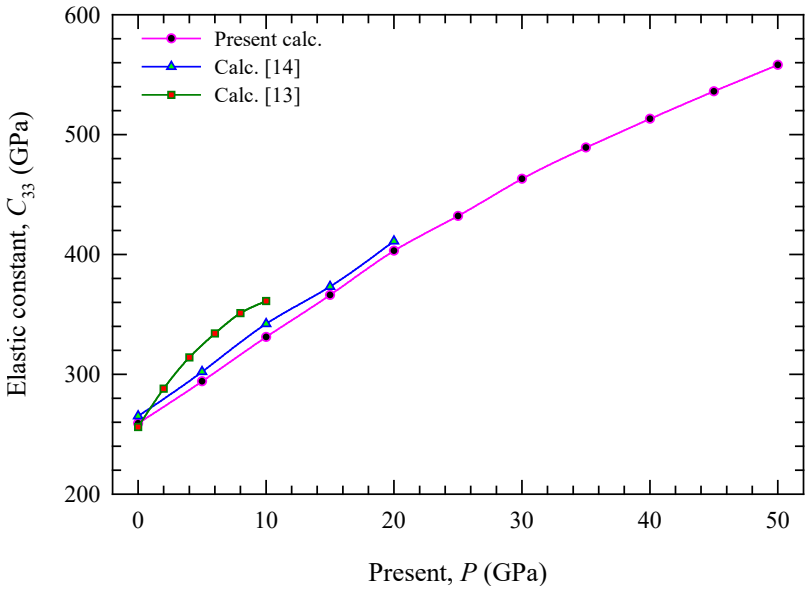

Fig. 6.2.1(n). Pressure dependence of elastic constant C_{33} of superconducting MAX phase Nb_2InC.

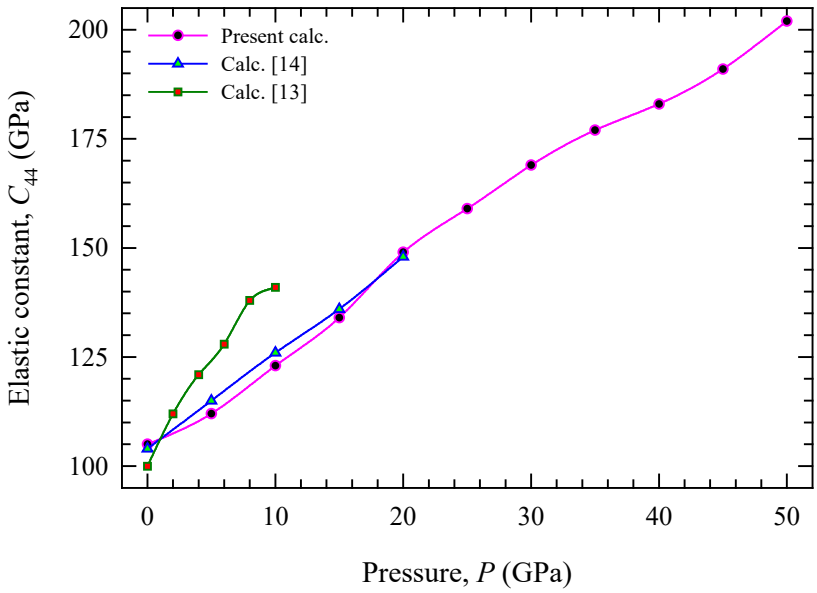

Fig. 6.2.1(o). Pressure dependence of elastic constant C_{44} of superconducting MAX phase Nb_2InC.

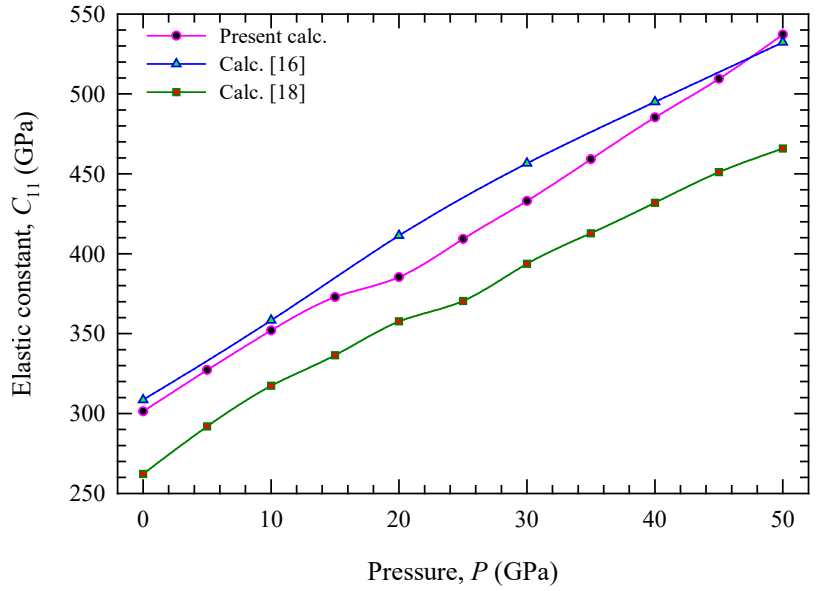

Fig. 6.2.1(p). Pressure dependence of elastic constant C_{11} of superconducting MAX phase Ti_2GeC.

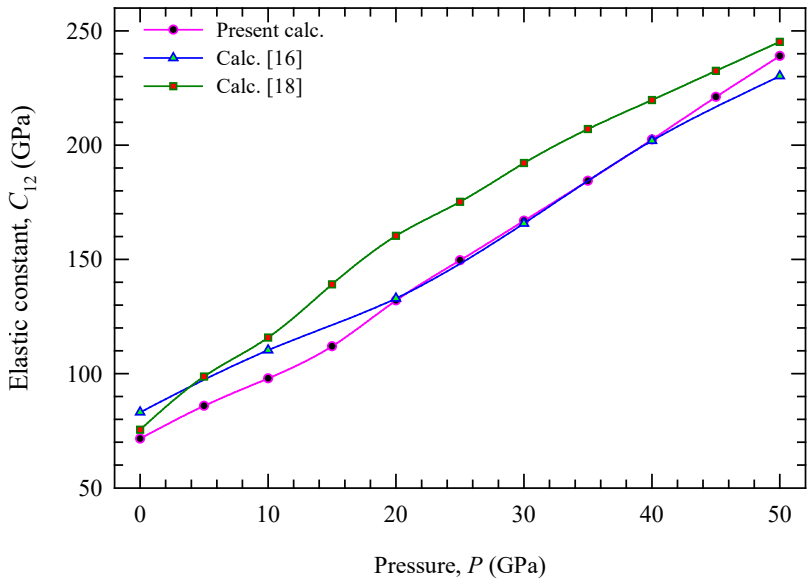

Fig. 6.2.1(q). Pressure dependence of elastic constant C_{12} of superconducting MAX phase Ti_2GeC.

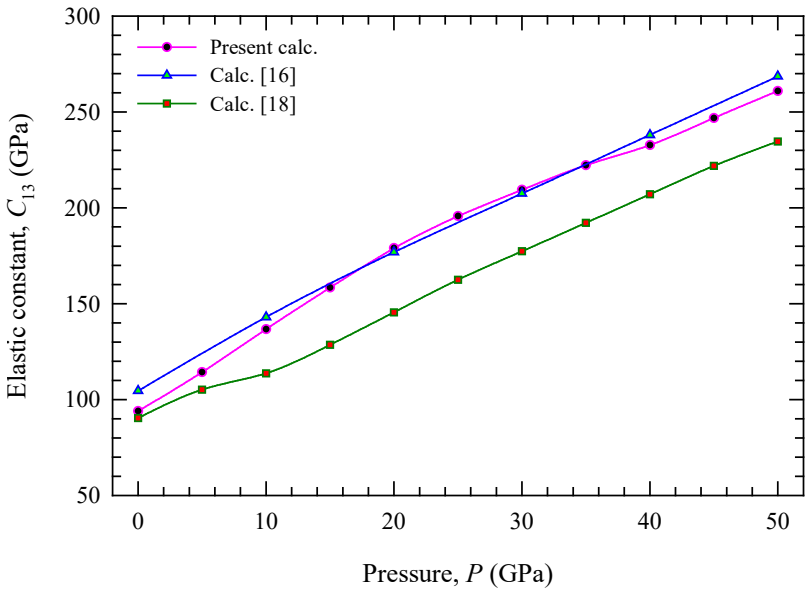

Fig. 6.2.1(r). Pressure dependence of elastic constant C_{13} of superconducting MAX phase Ti_2GeC.

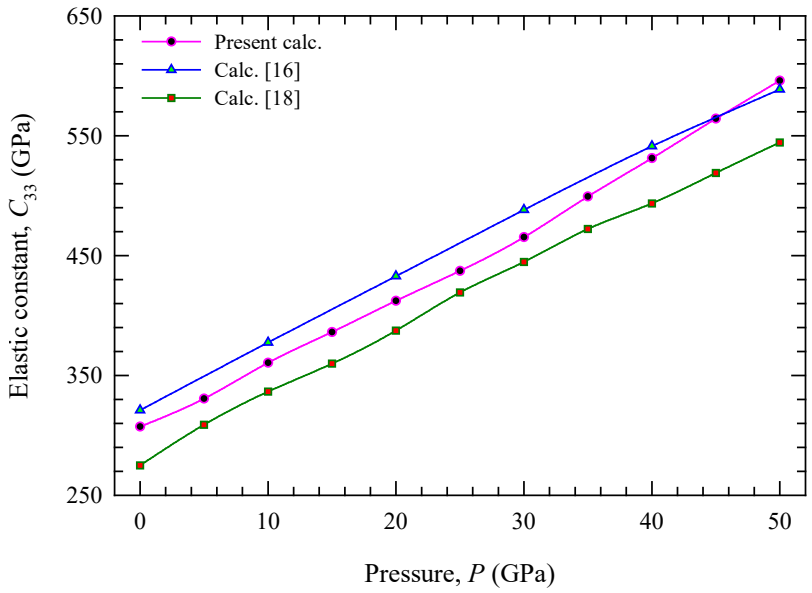

Fig. 6.2.1(s). Pressure dependence of elastic constant C_{33} of superconducting MAX phase Ti_2GeC.

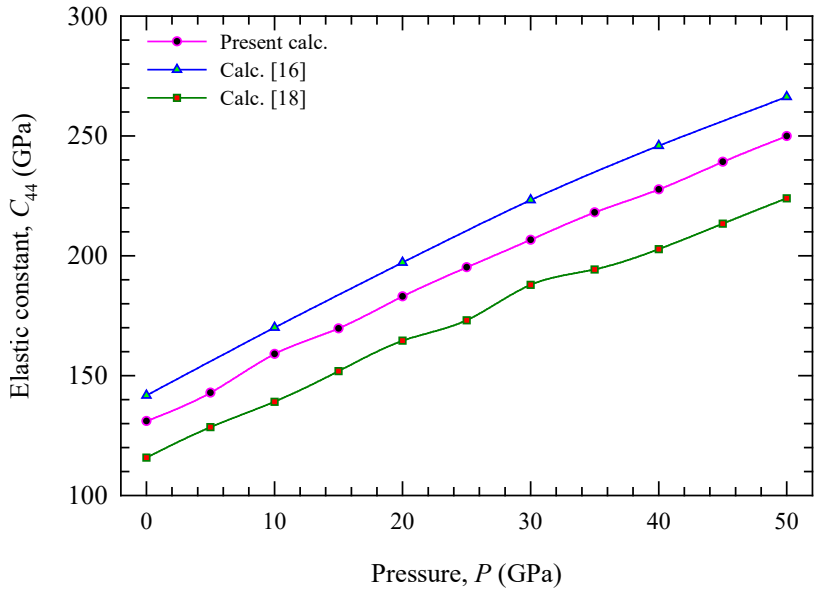

Fig. 6.2.1(t). Pressure dependence of elastic constant C_{44} of superconducting MAX phase Ti_2GeC.

6.2.2 Elastic properties of polycrystalline aggregate

We have estimated the bulk modulus B and shear modulus G of polycrystalline aggregates from the individual elastic constants C_{ij}, by the well-known Voigt [36] and Reuss [37] approximations combined with the Hill [38] suggestion. We also calculated the Young's modulus Y and the Poisson's ratio ν. All these properties are presented in Table 5.2.2a together with other results [9-18,19]. Our results are in reasonable agreement with these values. Bulk and shear moduli are still the most important parameters for estimating the material hardness. The materials with high bulk modulus represent their incompressibility and with high shear modulus restrict deformation. Among the studied four superconducting MAX phases, Nb_2AsC has the largest average bulk modulus (205 GPa), indicating that it is the most difficult to compress among these compounds, followed by Mo_2GaC (194 GPa), Nb_2AsC (168 GPa), and Ti_2GeC (162 GPa). As we know, shear modulus shows a better correlation with hardness than with bulk modulus. From Table 5.2.2a, it can be seen that Nb_2AsC has the largest average shear modulus (120 GPa), suggesting that it can withstanding shear strain to the largest extent. The Young's modulus defined by the ratio of stress to strain measures the stiffness of the solids. The materials having high Young's modulus represent them as stiff materials. As a result, Nb_2AsC is stiffer than the other three MAX phases.

According to the Pugh's criteria [39], a material should be brittle if its $G/B > 0.5$, otherwise it should be ductile. Hence, the four superconducting phases under study should behave in a brittle manner. According to Frantsevich rule [40], a material should be brittle if its Poisson's ratio is less than 0.33, otherwise it should be ductile. In our case, this value is smaller than 0.33. So, Mo_2GaC, Nb_2Asc, Nb_2InC, and Ti_2GeC possess the property of brittleness. Therefore, we can conclude that the studied four nanolaminates are brittle in nature according to both indicators. In fact, the brittleness is the general trend of MAX phases [41,42]. The relatively low values of Poisson's ratios for hard materials in general exhibit the high degree of directional covalent bonding. As seen from Table 5.2.2a, the small Poisson's ratios of four nanolaminates indicate their high degree of directional covalent bonding.

The pressure effect on elastic properties of polycrystalline aggregate has also been studied and presented in Table 6.2.2b and Figs. 6.2.2(a) – 6.2.2(h). It is seen that all the moduli increase monotonically with increasing of pressure. Figs. 6.2.2(e) – 6.2.2(h) show the effect of applied pressure on the Pugh's and Poisson's ratios. The G/B ratios decrease with increasing of pressure, which implies the gradual decrease of brittleness of the four compounds. Moreover, the G/B value is equal to ~0.5 at P = 10 GPa for Mo_2GaC, at P = 20 GPa for Nb_2AsC, and at P = 35 GPa for Nb_2InC and thus the transition from brittle to ductile occurs at the respective pressures. Only the phase Ti_2GeC remains brittle within the entire pressure range. According to Frantsevich rule only Mo_2GaC switches from brittle to ductile nature.

Table 6.2.2a: Calculated Bulk moduli (B_V, B_R, B in GPa), shear moduli (G_V, G_R, G in GPa), Young's modulus (Y in GPa), Pugh's ratio G/B, and Poisson's ratio ν in comparison with available data for the four superconducting MAX phases.

Phases	B_V	B_R	B	G_V	G_R	G	Y	G/B	ν
Mo_2GaC-Present	190.6	187.8	189	104.6	97.3	101	257	0.534	0.274
LDA-VSP [9]	201.0	198.0	200	92.9	88.4	91	236	0.455	0.303
PW 91-GGA-VASP [10]	191.3	188.6	190	101.6	93.2	97	250	0.513	0.281
PBE-GGA-WIEN2k [11]	199.1	196.4	198	93.0	87.3	90	235	0.456	0.302
PBE-GGA-VASP [12]	198.0	195.0	197	107.4	99.8	104	265	0.528	0.276
Nb_2AsC-Present	208.4	206.8	208	128.3	119.0	124	309	0.596	0.252
PW 91-GGA-VASP [10]	205.3	204.2	205	117.1	109.2	113	287	0.554	0.267
PBE-GGA-WIEN2k [11]	204.1	202.2	203	125.6	117.6	122	304	0.599	0.250
Calc. [13]	209.2	207.2	208	126.9	114.5	121	304	0.582	0.257
Nb_2InC-Present	154.6	154.5	155	99.2	97.2	98	243	0.636	0.238
PW 91-GGA-VASP [10]	166.3	165.6	166	81.4	75.2	78	203	0.472	0.296
PBE-GGA-WIEN2k [11]	159.2	159.2	159	99.4	98.0	99	246	0.620	0.243
LDA-CASTEP [14]	195.8	195.4	196	129.7	125.8	128	315	0.653	0.232
PW 91-GGA-CASTEP [15]	156.7	156.4	157	101.9	100.5	101	250	0.646	0.234
GGA-CASTEP [16]	157.2	157.2	157	99.6	98.1	99	245	0.629	0.240
LDA-CASTEP [16]	183.1	183.1	183	112.2	110.0	111	277	0.607	0.248
Ti_2GeC-Present	158.8	158.5	159	118.7	117.6	118	284	0.745	0.202
LDA-CASTEP [17]	157.6	157.6	158	104.8	102.3	104	255	0.657	0.231
LDA-CASTEP [18]	169.8	169.4	170	122.7	120.4	122	294	0.717	0.211
PBE-GGA-CASTEP [20]	157.0	156.6	159	107.0	105.6	106	260	0.678	0.223

Table 6.2.2b: Calculated Bulk moduli (B_V, B_R, B in GPa), shear moduli (G_V, G_R, G in GPa), Young's modulus (Y in GPa), Pugh's ratio G/B, and Poisson's ratio ν at different pressures.

Phases	Pressure	B_V	B_R	B	G_V	G_R	G	Y	G/B	ν
Mo_2GaC	0	190.6	187.8	189	104.6	97.3	101	257	0.534	0.274
	5	216.8	213.3	215	114.2	104.9	110	281	0.510	0.282
	10	240.3	233.0	237	125.0	110.5	118	303	0.500	0.287
	15	262.0	252.2	257	135.4	115.0	125	323	0.487	0.291
	20	287.9	276.0	282	138.2	115.1	127	331	0.449	0.305
	25	308.9	291.2	300	143.3	114.6	129	338	0.430	0.312
	30	330.8	315.8	323	145.2	122.1	134	352	0.413	0.318
	35	354.9	343.2	349	152.6	132.2	142	376	0.408	0.320
	40	375.8	366.6	371	153.6	132.2	143	380	0.385	0.329
	45	396.3	385.4	391	157.1	132.8	145	387	0.371	0.335
	50	414.6	399.4	407	157.5	127.3	142	383	0.350	0.343
Nb_2AsC	0	208.4	207.0	208	128.2	119.0	124	309	0.595	0.252
	5	233.0	229.5	231	134.6	120.7	128	323	0.552	0.267
	10	252.3	249.7	251	136.2	117.4	127	326	0.505	0.284
	15	271.7	268.5	270	148.9	127.4	138	354	0.512	0.281
	20	293.9	291.6	293	143.9	115.8	130	339	0.444	0.307
	25	311.4	307.6	310	156.2	125.7	141	367	0.455	0.302
	30	334.1	329.7	332	176.5	143.5	160	414	0.482	0.292
	35	345.0	343.7	344	185.9	149.4	168	433	0.487	0.291
	40	368.8	366.4	368	195.8	155.2	176	454	0.477	0.294
	45	395.0	389.5	392	203.6	160.0	182	472	0.463	0.299
	50	413.0	407.1	410	210.4	166.0	188	490	0.459	0.301
Nb_2InC	0	154.6	154.5	155	99.2	97.2	98	243	0.636	0.238
	5	178.9	178.4	179	103.5	101.2	102	258	0.573	0.260
	10	202.4	201.4	202	112.1	109.2	111	281	0.548	0.268
	15	225.5	224.6	225	121.6	118.7	120	306	0.534	0.273
	20	249.9	248.9	249	136.3	132.6	134	342	0.539	0.272
	25	271.1	270.3	271	145.0	141.3	143	365	0.529	0.275
	30	292.6	291.5	292	153.2	148.8	151	386	0.517	0.280
	35	312.8	311.5	312	159.1	154.2	157	403	0.502	0.285
	40	331.8	330.2	331	163.9	158.4	161	416	0.487	0.291
	45	350.7	348.8	350	168.6	162.3	165	429	0.473	0.296
	50	375.6	370.5	373	174.8	170.0	172	448	0.462	0.300
Ti_2GeC	0	158.8	158.5	159	118.7	117.6	118	284	0.745	0.202
	5	179.3	179.0	179	126.0	124.0	125	304	0.698	0.217
	10	200.8	200.0	200	135.2	131.6	133	328	0.666	0.228
	15	221.0	219.7	220	140.8	135.9	138	343	0.628	0.240
	20	240.3	238.3	239	144.7	137.4	141	354	0.590	0.254
	25	259.7	257.8	259	151.7	143.1	147	372	0.570	0.261
	30	278.0	276.2	277	159.0	149.6	154	390	0.557	0.265
	35	297.2	295.4	296	167.3	157.5	162	412	0.548	0.268
	40	315.2	313.7	315	174.9	165.1	170	432	0.541	0.271
	45	334.7	333.0	334	182.4	171.5	177	451	0.530	0.275
	50	354.6	353.1	354	190.4	179.0	185	472	0.522	0.278

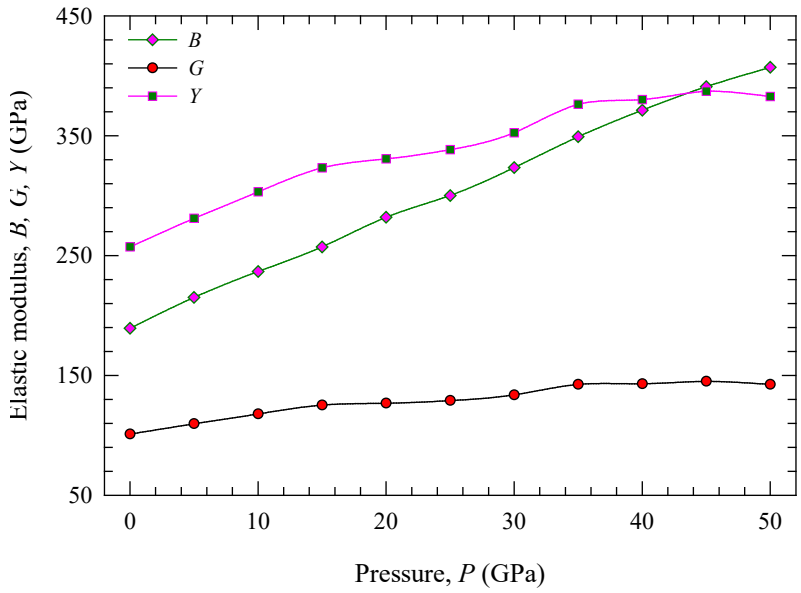

Fig. 6.22(a) Bulk, shear and Young's modulus of Mo_2GaC as a function of pressure.

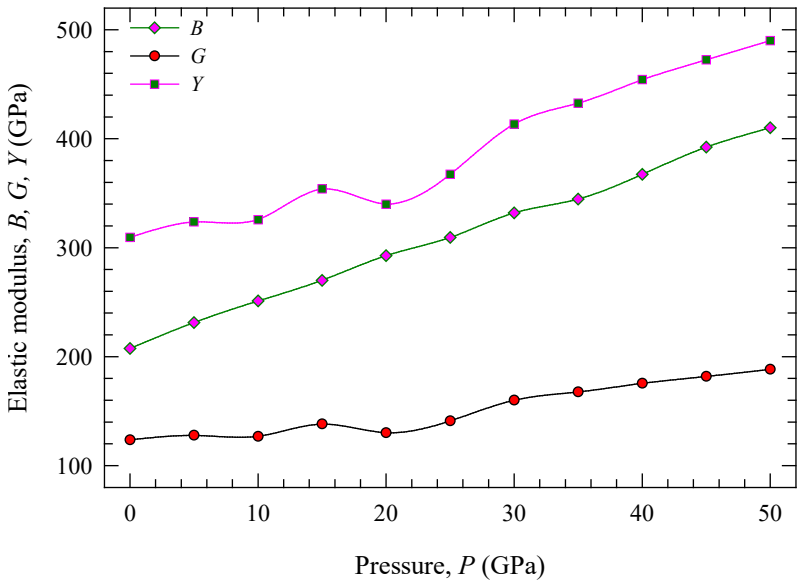

Fig. 6.22(b) Bulk, shear and Young's modulus of Nb_2AsC as a function of pressure.

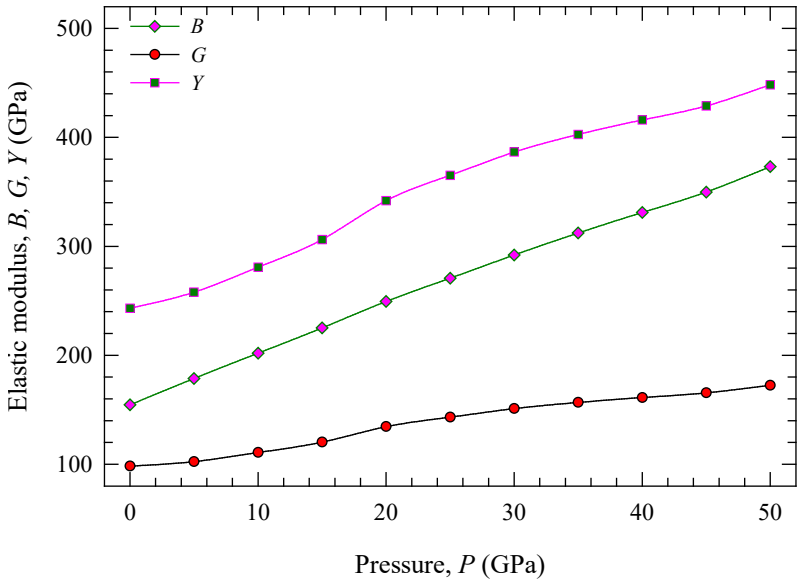

Fig. 6.22(c) Bulk, shear and Young's modulus of Nb_2InC as a function of pressure.

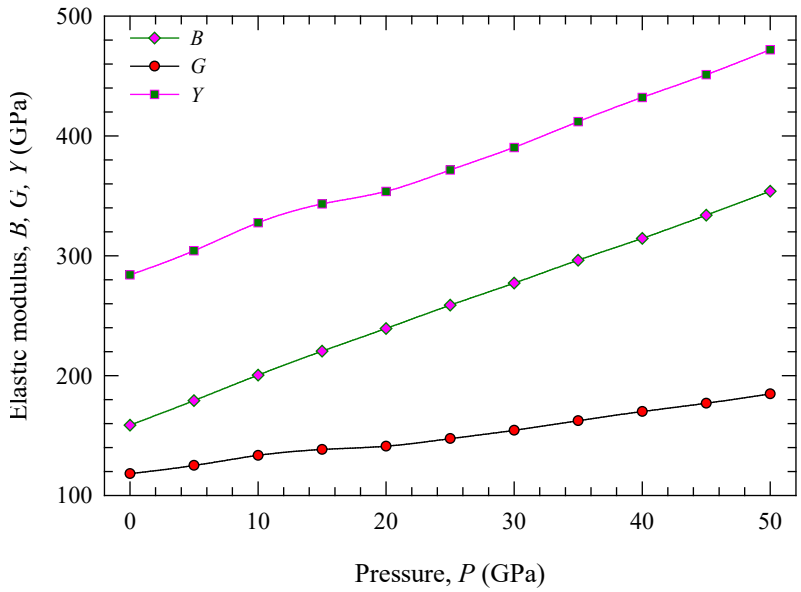

Fig. 6.22(d) Bulk, shear and Young's modulus of Ti_2GeC as a function of pressure.

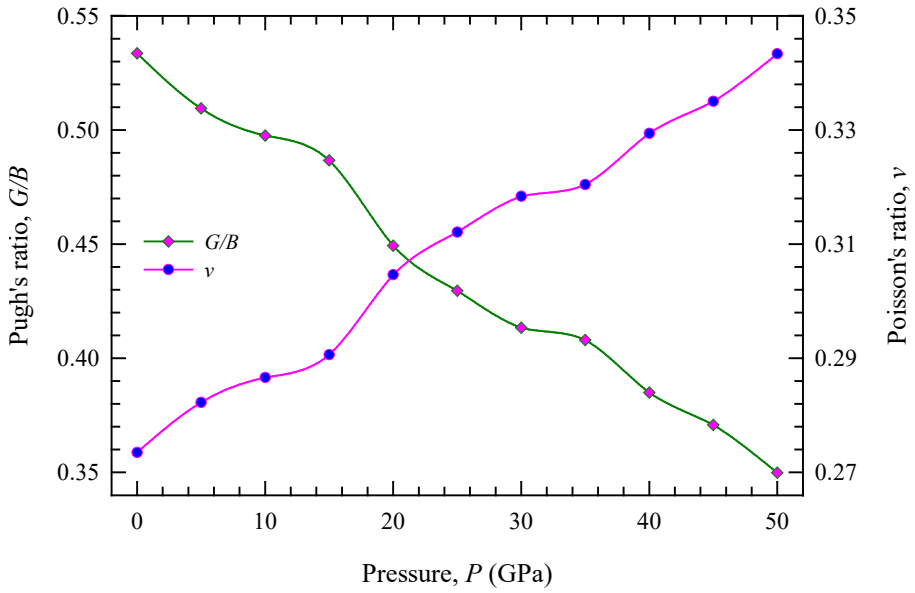

Fig. 6.22(e) Pugh's and Poisson's ratios of Mo_2GaC as a function of pressure.

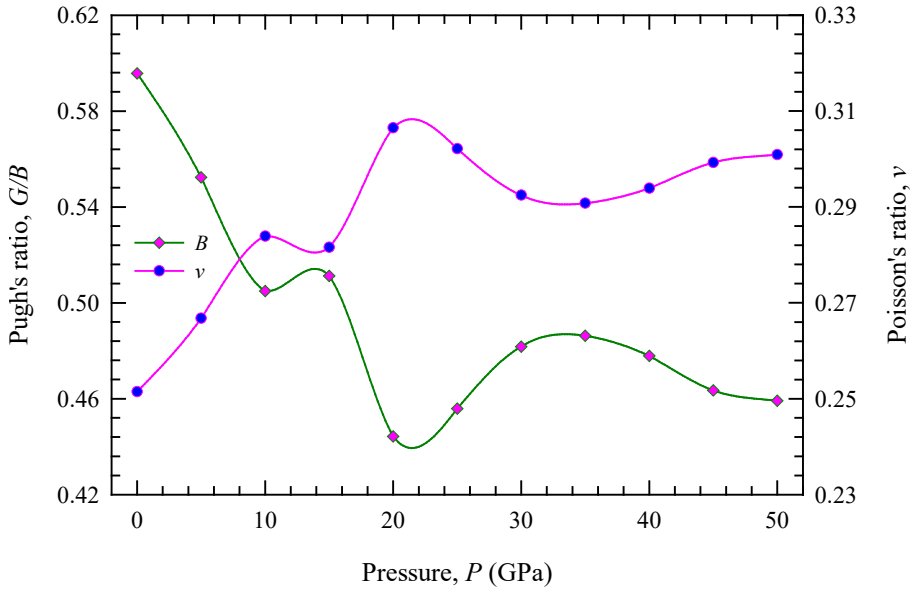

Fig. 6.22(f) Pugh's and Poisson's ratios of Nb_2AsC as a function of pressure.

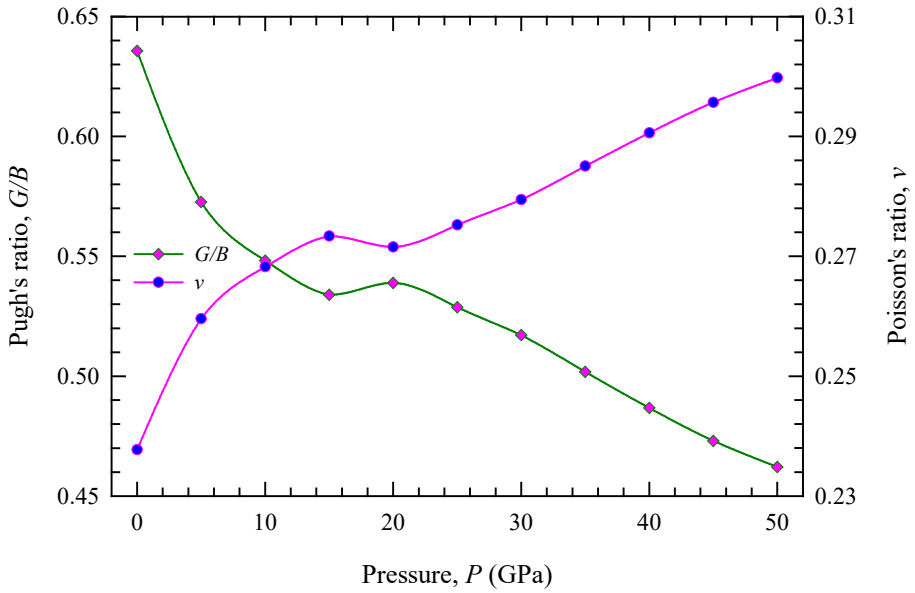

Fig. 6.22(g) Pugh's and Poisson's ratios of Nb_2InC as a function of pressure.

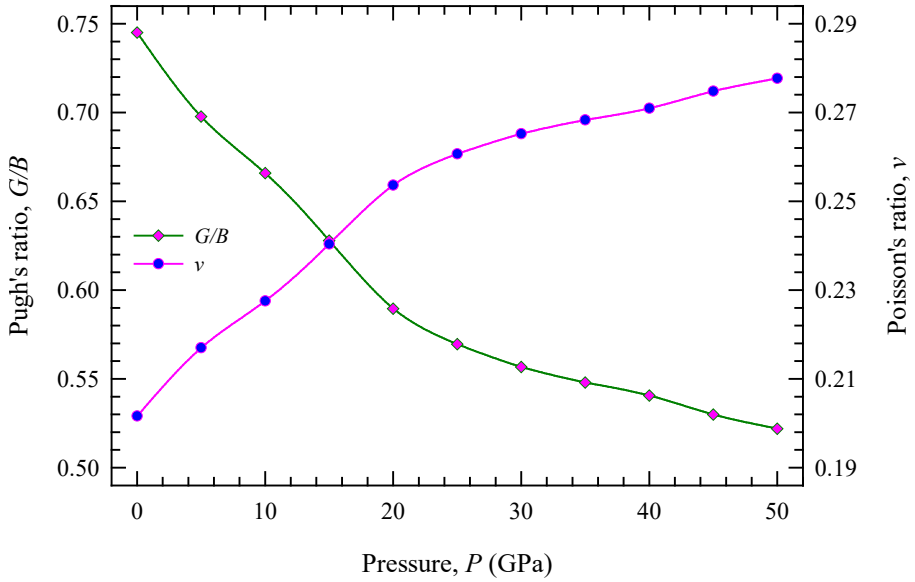

Fig. 6.22(h) Pugh's and Poisson's ratios of Ti_2GeC as a function of pressure.

6.3. Electronic properties

Electronic properties calculations not only predict physical and chemical properties of the materials, but they also provide good insight into the experimentalists to synthesize novel materials for various applications. In the present study, we discuss our results pertaining to electronic properties of the four superconducting MAX phases Mo_2GaC, Nb_2AsC, Nb_2InC, and Ti_2GeC through energy band structure, density of states, and Fermi surfaces. Since there is no precise experimental DOSs at the Fermi level available for the presently investigated materials, we have calculated the same using the plane-wave pseudopotential method based on the density functional theory implemented in the CASTEP code.

6.3.1 Band structures

The electronic band structure of a material is the key link between its crystal structure and physical properties. Electronic band structure has been successfully used to explain many physical properties of solids, such as electrical resistivity, electronic transport properties and optical absorption, and forms the foundation of the understanding of all solid-state devices such as transistors, solar cells, etc. The calculated band structures for the four superconducting MAX phases Mo_2GaC, Nb_2AsC, Nb_2InC, and Ti_2GeC along the high symmetry directions in the first Brillouin zone are illustrated in Figs. 6.3.1(a) – 6.3.1(d) in the energy range from –15 to 6 eV. The Fermi levels are set to 0 eV. There are many valence bands crossing the Fermi level (E_F) and overlapping with conduction bands, which indicates the metallic conductivity of the four compounds. Moreover, the energy bands around the Fermi level mainly from the M d states, suggesting that the M d states dominate the conductivity of Mo_2GaC, Nb_2AsC, Nb_2InC, and Ti_2GeC. The energy band structures of the four MAX phases exhibit anisotropic characters, indicating their anisotropic properties, such as optical and mechanical properties. The band structures show both the hole-like and electron-like character of the crossing bands, resulting in the multiband system dominated by M d character.

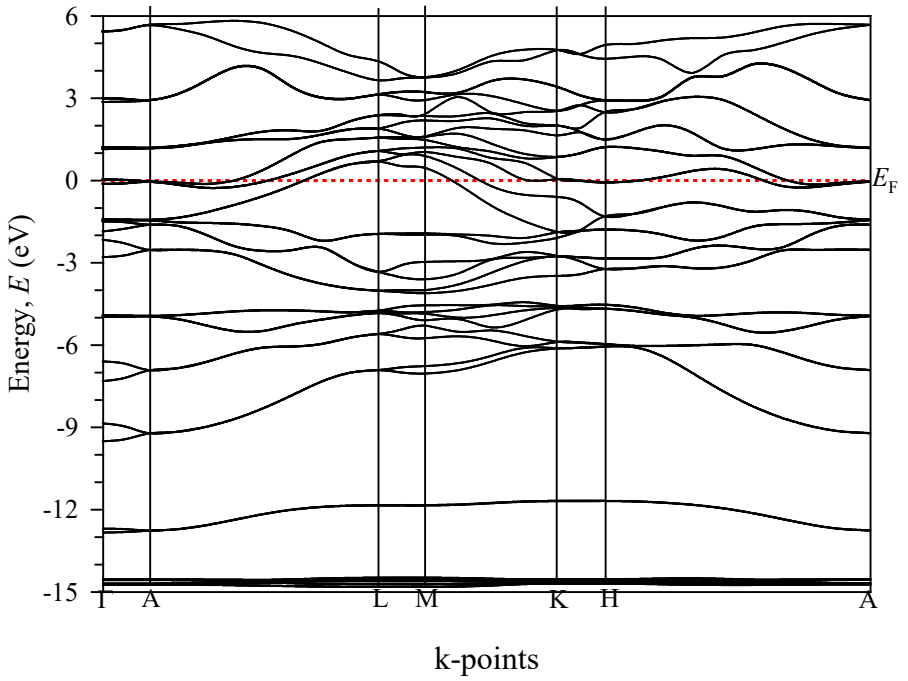

Fig. 6.3.1(a). Electronic band structure of superconducting MAX phase Mo_2GaC.

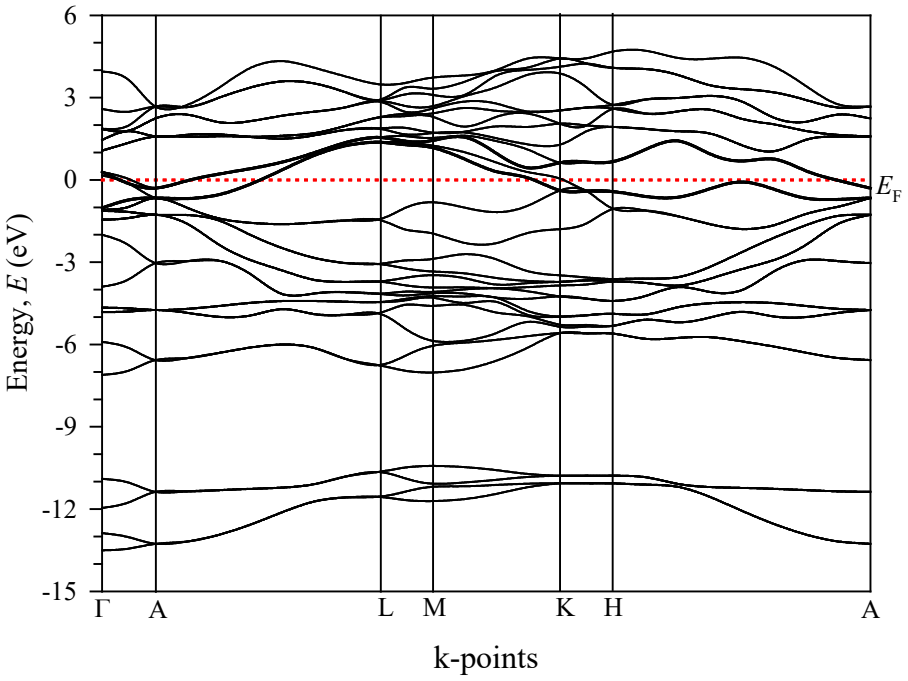

Fig. 6.3.1(b). Electronic band structure of superconducting MAX phase Nb_2AsC.

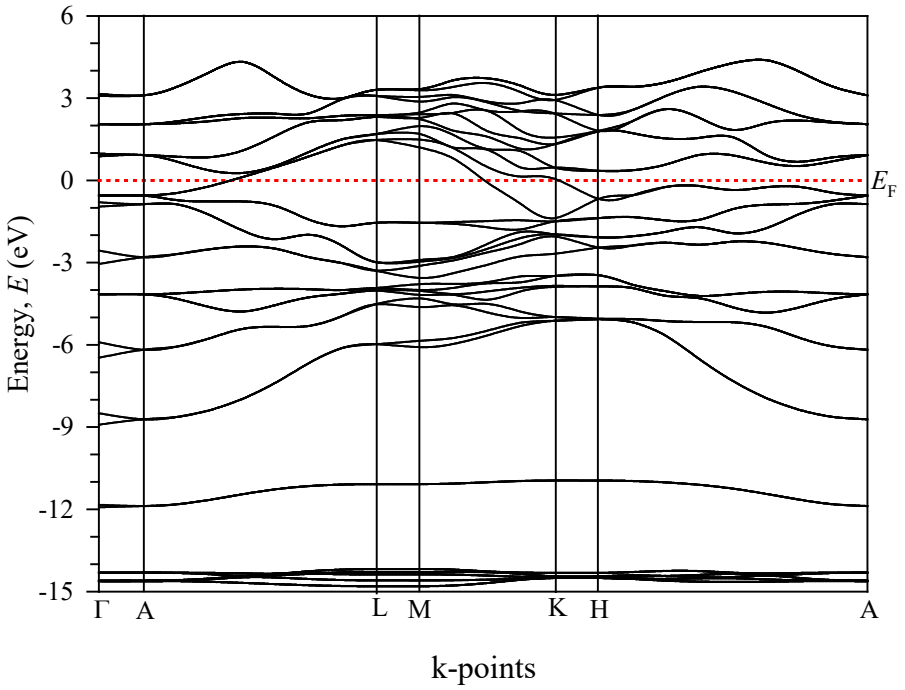

Fig. 6.3.1(c). Electronic band structure of superconducting MAX phase Nb_2InC.

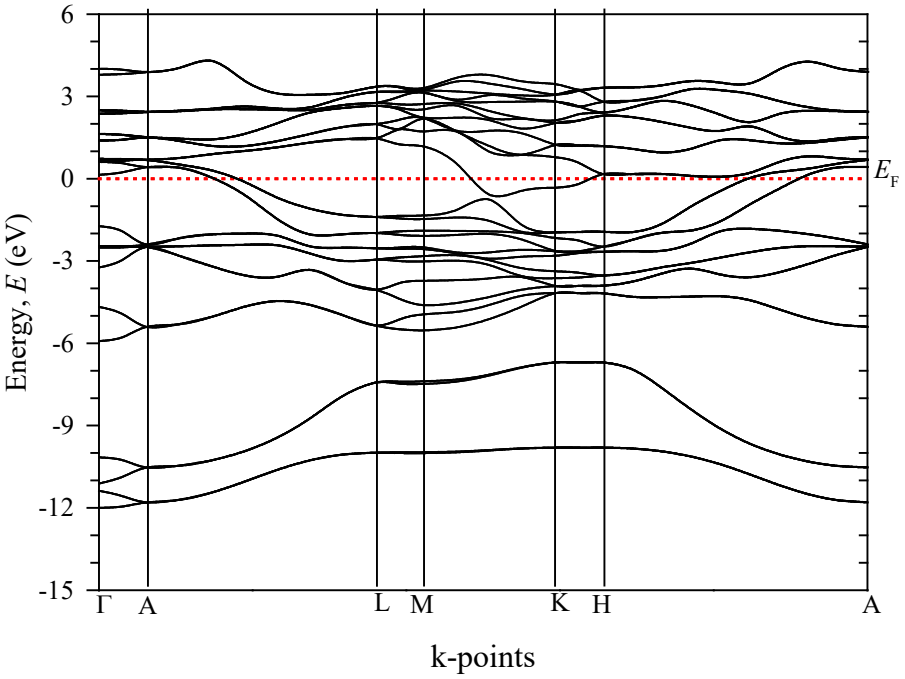

Fig. 6.3.1(d). Electronic band structure of superconducting MAX phase Ti_2GeC.

6.3.2 Density of states

The calculated total and partial density of states (DOS) of the four superconducting MAX compounds Mo_2GaC, Nb_2AsC, Nb_2InC, and Ti_2GeC are shown in Figs. 6.3.2(a)–6.3.2(d). The DOS in the vicinity of the Fermi level E_F normally lies in a dip for a mechanically stable phase. This location may split bonding and antibonding states giving rise to stronger cohesion, the structural stability [43] and high bulk modulus. In addition, the existence of a deep valley named pseudogap at the left of the Fermi level in the DOS indicates the structural stability [44]. Therefore, the studied four nanolaminates are stable mechanically. The *d* states of the M (Mo, Nb, and Ti) elements are mainly contributing to the DOS at the Fermi level of the selected four 211 MAX phases and should play a dominant role in the conduction properties. Carbon (C) does not contribute significantly to the DOS at the Fermi level and therefore is not involved in electrical transport. A (Ga, As, In, and Ge) atoms have a poor contribution at the Fermi level. These results are consistent with the previous reports on other MAX phases [45]. At the Fermi level, the DOSs for Mo_2GaC, Nb_2AsC, Nb_2InC, and Ti_2GeC are 4.55, 2.46, 3.66, and 3.03 states per unit cell per eV, respectively, which are similar to those found in literatures [11,15,17-19,46,47]. The finite values of the DOSs at the Fermi levels confirm the metallic properties of these nanolaminates.

It is observed that just below the Fermi level the *p* states of A-elements interact with the *d* states of M-atoms and in the deeper energy C 2*p* as well as C 2*s* states hybridize with M *d* states and as a result the covalent M–A and M-C bonds occur. Due to closeness to the Fermi level M-A bonds are weaker than M-C bonds and strong M *d*–C *p* hybridization stabilizes the structures of M_2AC. It is obvious that a covalent bonding occurs between the comprising elements due to the reason that states are degenerate with both angular momentum and lattice site, and also due to the difference in electronegativity between the constituting elements, some ionic interaction can be expected. Therefore, the bonding nature in four carbide M_2AC compounds may be described as a mixture of covalent, ionic, and, due to the *d* resonance in the vicinity of the Fermi level, metallic.

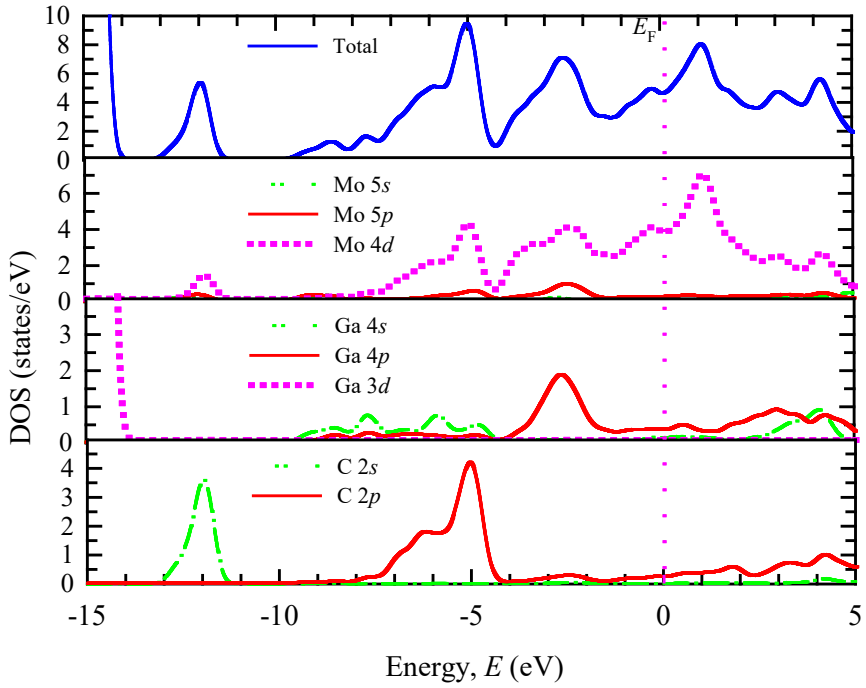

Fig. 6.3.2(a). Total and partial density of states of superconducting Mo_2GaC.

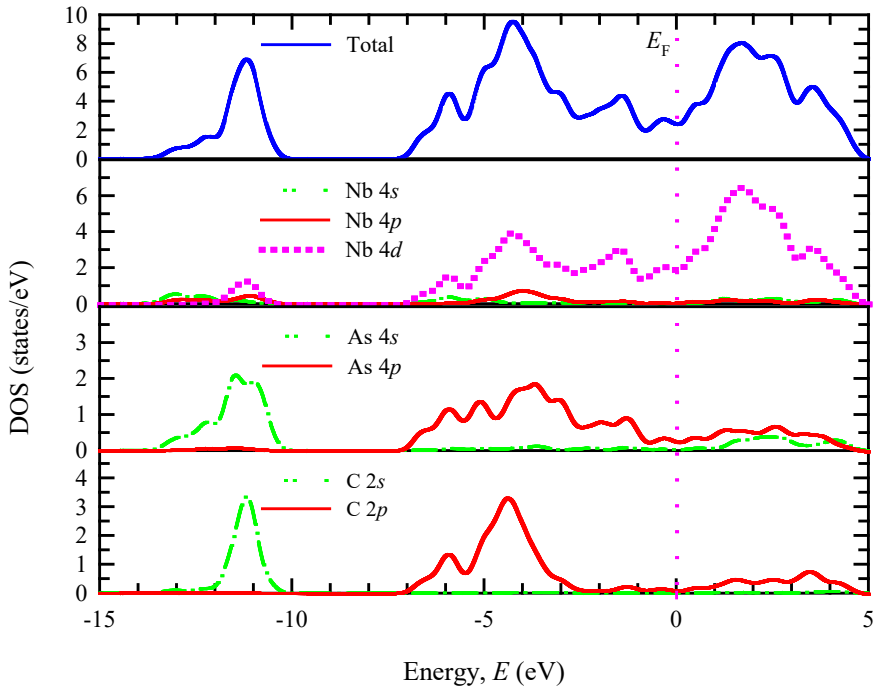

Fig. 6.3.2(b). Total and partial density of states of superconducting Nb_2AsC.

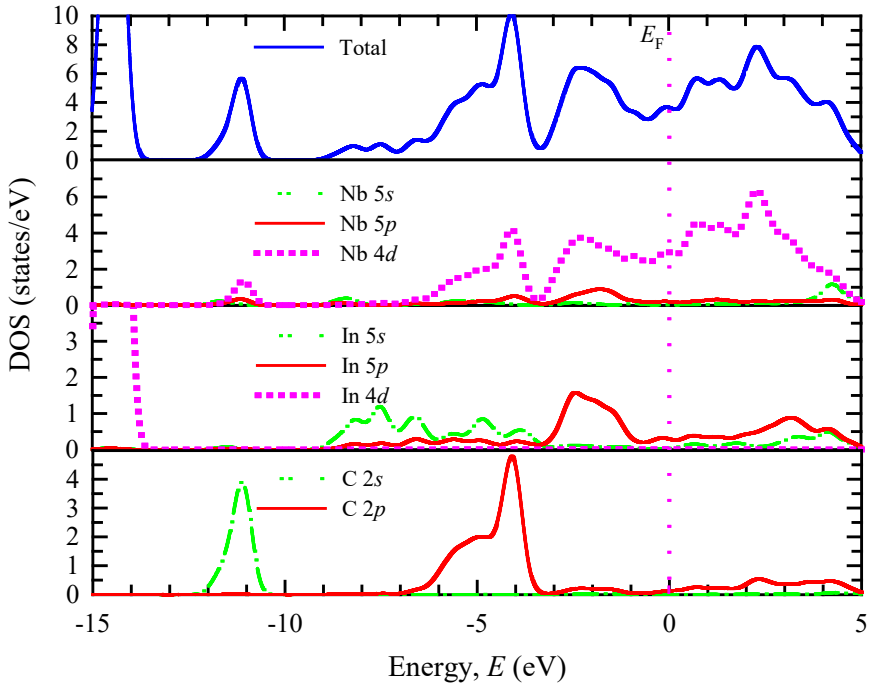

Fig. 6.3.2(c). Total and partial density of states of superconducting Nb_2InC.

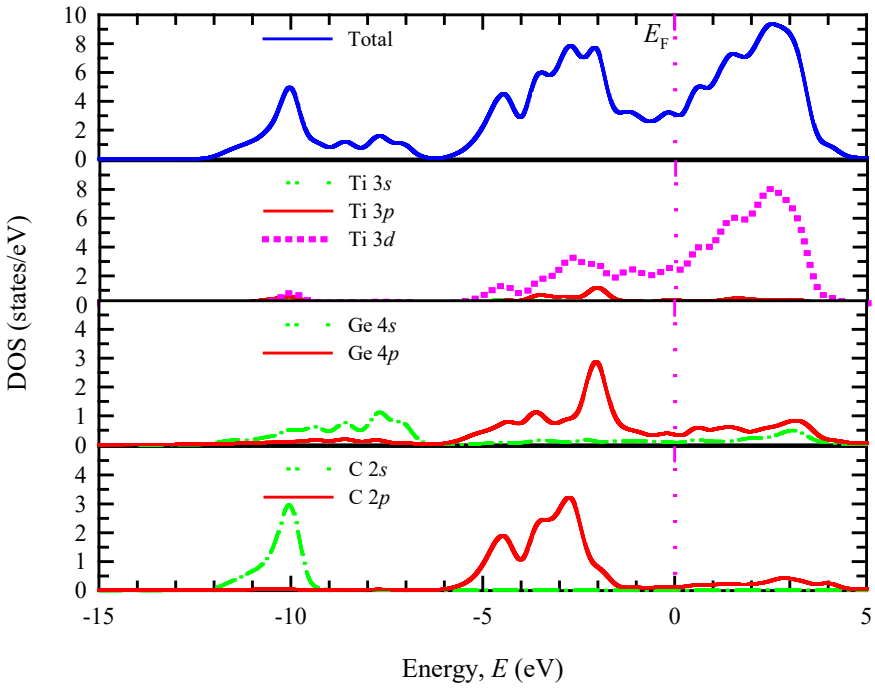

Fig. 6.3.2(d). Total and partial density of states of superconducting Ti_2GeC.

6.3.3 Fermi surfaces

The investigated Fermi surfaces of the four superconducting MAX phases are shown in Figs. 6.3.3(a) – 6.3.3(d). The Fermi surface of Mo_2GaC presented in Fig. 6.3.3(a) consists of electronic-like sheet with prismatic-like system centered along the Γ–A direction. The surface also includes enough complex topology of the hole-like sheets centered in the corners of the Brillouin zone. The Fermi surface of Mo_2GaC is formed mainly by the low-dispersive Mo 4*d* like bands from [MoC] blocks, which should be responsible for the superconductivity of Mo_2GaC.

The superconducting Nb_2AsC has the Fermi surface formed by both the electron- and hole-like sheets of different topology shown in Fig. 6.3.3(b). The cylindrical-like first sheet with rectangular cross section is centered along the Γ-A direction. The central sheet is surrounded by two similar sheets positioned at the opposite directions, which formed cross-shaped combinedly. Two different prismatic sheets are positioned at the lateral sides of the Brillouin zone along the both L–M and H–K directions. The superconducting behaviour of this nanolaminate arises due to the low dispersive Nb 4d like bands from [NbC] blocks.

Fig. 6.3.3(c) shows the Fermi surface of Nb_2InC that is made of enough complex topology of both electronic- and hole-like sheets centered along the Γ–A direction. There are two dimensional-type sheets parallel to the k_z direction, centered at the lateral sides of the Brillouin zone along the L–M direction. The Fermi surface of Nb_2InC like Mo_2GaC is formed mainly by the low dispersive Nb 4*d* like bands from [NbC] layers, which should be responsible for superconductivity for Nb_2InC.

The investigated Fermi surface of Ti_2GeC is shown in Fig. 6.3.3(d). The centre of the Fermi surface consists of four hole-like sheets with different topology centered along the Γ-A direction. The first sheet is sand-watch shaped and surrounded by very close cylindrical-like second sheet. The remaining two sheets are cylindrical-like with hexagonal cross-section. These two sheets are nearly closed but apart from the second sheet. There is also additional electron and hole-like sheets along the H-K direction. The Fermi surface is formed mainly by the low-dispersive bands, which should be responsible for the superconductivity in the compound.

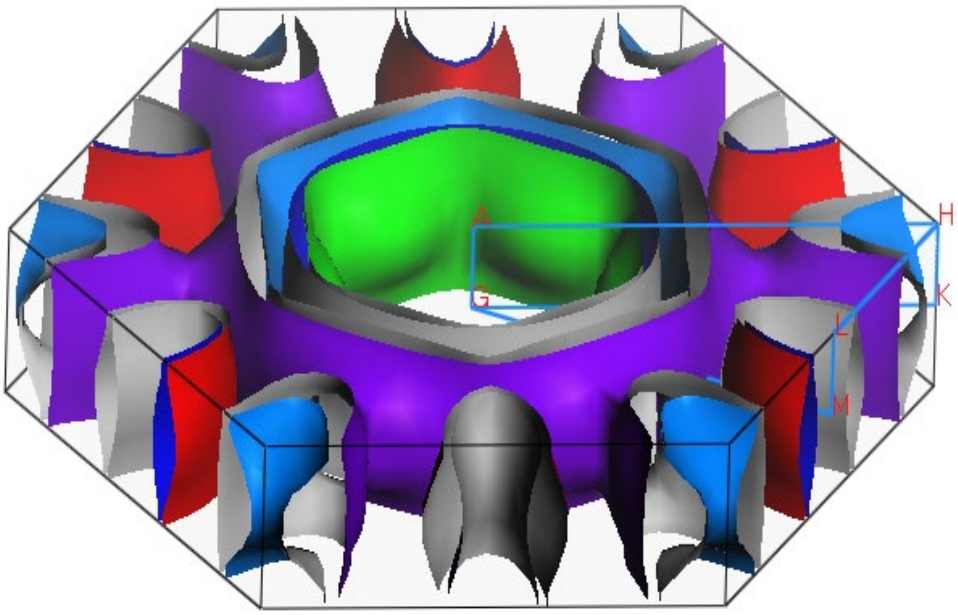

Fig. 6.3.3(a). Fermi surface of superconducting MAX phase Mo_2GaC.

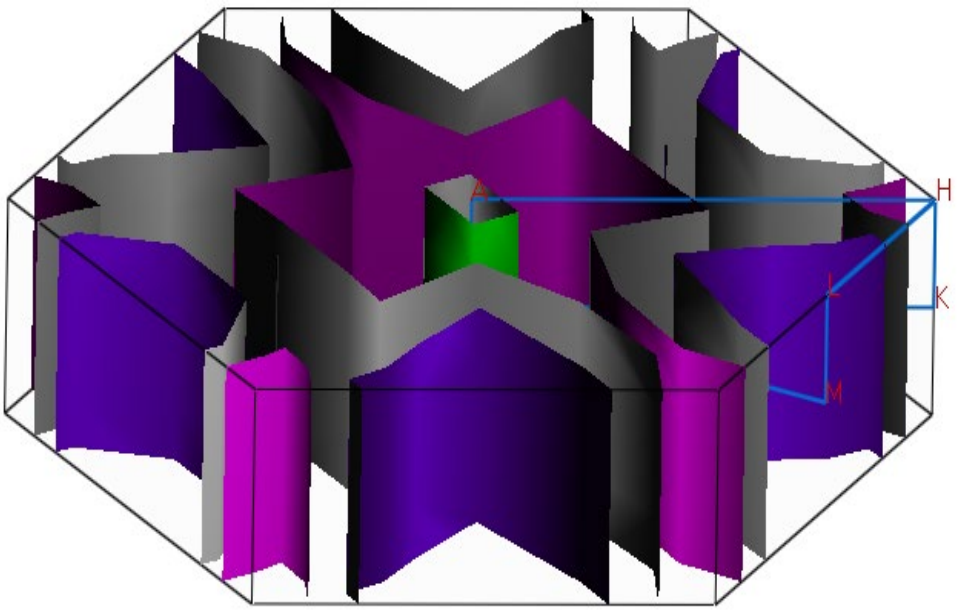

Fig. 6.3.3(b). Fermi surface of superconducting MAX phase Nb_2AsC.

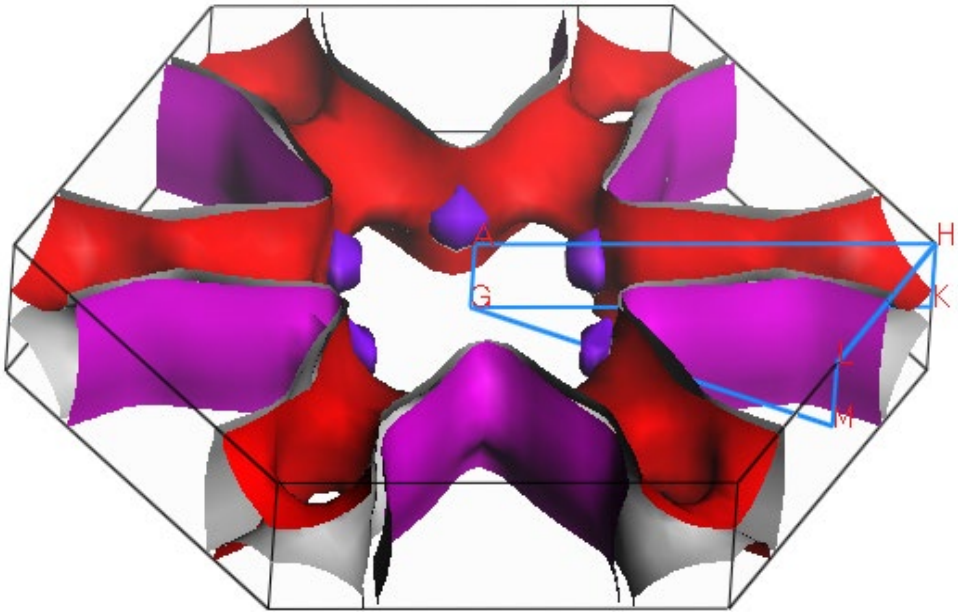

Fig. 6.3.3(c). Fermi surface of superconducting MAX phase Nb_2InC.

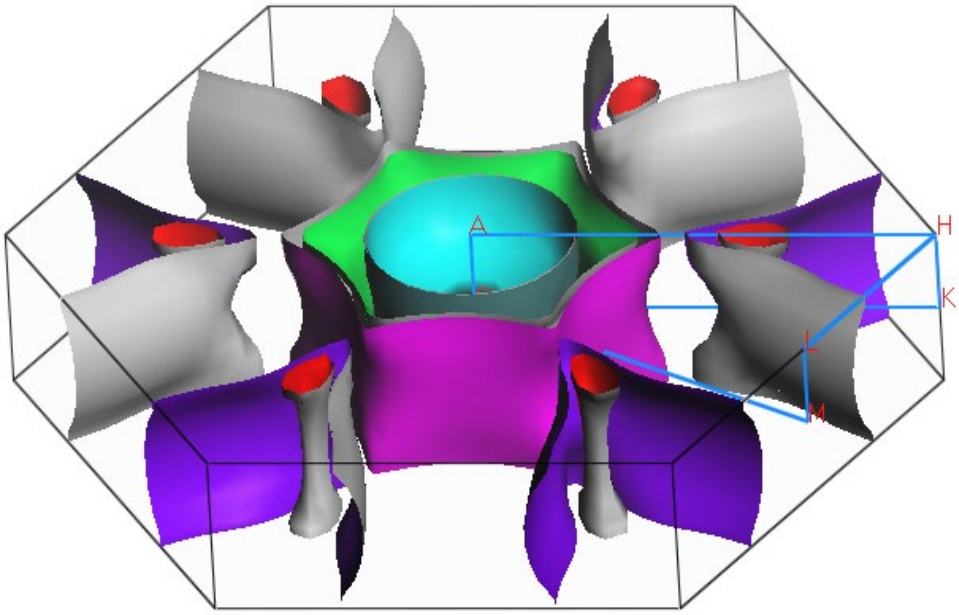

Fig. 6.3.3(d). Fermi surface of superconducting MAX phase Ti_2GeC.

6.4. Mulliken bond population and theoretical hardness

To describe the bonding nature and to evaluate the theoretical Vickers hardness of Mo_2GaC, Nb_2AsC, Nb_2InC, and Ti_2GeC, the Mulliken bond populations are investigated. The results obtained from the calculations are given in Table 5.4(a). The Mulliken bond populations measure the degree of overlap of the electron clouds of the two bonding atoms, and its highest and lowest values signify the strength of covalency and ionicity in chemical bonds, respectively. Therefore, it can be seen that the M-C bonds possess stronger covalent bonding than M-M bonds. This result is consistent with DOS calculation and Mulliken bond population analysis for V_4AlC_3 [48] and Nb_4SiC_3 [49]. Further, the typical electronegativity rule is that bonds with an electronegativity difference within 0.5 to 1.6 are considered polar covalent. On the other hand, a difference between 0.0 and 0.4 indicates a non-polar covalent. Here in Nb-C bond, the electronegativity difference between Nb (1.6) and C (2.5) is 0.9 and in Nb-Nb bond, the difference is exactly zero. As per this rule, the Nb-C bonds possess polar covalent bonding and Nb-Nb bonds hold non-polar covalent bonding. Since Nb is a metal, the Nb-Nb bonds are also metallic. Polar covalent bonds are always stronger than non polar covalent bonds. In fact, transition metals and intermetallic compounds based on transition metals can exhibit mixed metallic and covalent bonding [50]. DOS calculations of these materials also reveal that the overall bonding picture in these compounds may be described as a mixture of covalent, metallic, and ionic interactions.

Again, the degree of metallicity may be defined as $f_m = P^{\mu'}/P^{\mu}$. In our calculations, the values of f_m for Nb-Nb bonds in Nb_2AsC and Nb_2InC are 0.042 and 0.064, respectively, which are larger than that of the other bond (i.e., Nb-C: 0.016, 0.0135), indicating that the Nb-Nb bonds are more metallic than Nb-C bonds. Similarly, Mo-Mo (Ti-Ti) bond is more metallic than Mo-C (Ti-C) bond in Mo_2GaC (Ti_2GeC). After calculating the individual bond hardness of all bonds in the crystal the total Vickers hardness of the compound is found by taking geometric average of these bonds hardness. Considering the individual bond hardness, we can conclude that Nb-C bonds have the highest hardness in Nb_2AsC and Nb_2InC. However, Nb-C

bond-lengths are shorter than those of Nb-Nb bonds, and thus considering general relationships between bond length and hardness, we expect that Nb-C bonds are harder than Nb-Nb bonds. This expectation is also valid for Mo_2GaC and Ti_2GeC. The theoretically calculated values of the Vickers hardness for Mo_2GaC, Nb_2AsC, Nb_2InC, and Ti_2GeC are 9.6, 6.7, 7.9, and 11.6 GPa, respectively. It is worth mentioning that the values obtained here lie between the lowest (1.4 GPa for Cr_2GaC [51]) and the highest values (~15 GPa for Ti_3SiC_2 [52]) for MAX phases known so far. Further, to understand deeply the origin of intrinsic hardness on the atomistic level and to calculate accurately the values of Vickers hardness, the empirical formula (Eq. 4.26) used here has already been successful. For justification, one can see a set of theoretical values of Vickers hardness reported by Gou *et al*. [53] for crystals with partial metallic bonding that coincide with experiments. For instance, the theoretical (experimental) Vickers hardness for TaC, ZrC, TiN, and ZrN are 30.1 (29.0), 22.5 (25.8), 24 (23), and 16.7 (15) GPa, respectively. According to the value of v_b^μ, we observe that the lowest bond volume results in a highest hardness of the bond and according to the value of H_V, we may conclude that Nb_2AsC is relatively soft and easily machinable compared to other three phases.

Table 6.4a: Calculated Mulliken bond numbers n^μ, bond length d^μ, bond overlap population P^μ, bond volume v_b^μ and bond hardness H_v^μ of μ-type bond and metallic population $P^{\mu'}$, and Vickers hardness H_v of Mo_2GaC, Nb_2AsC, Nb_2InC, and Ti_2GeC.

Compounds	Bonds	n^μ	d^μ (Å)	P^μ	v_b^μ (Å^3)	$P^{\mu'}$	H_v^μ (GPa)	H_v (GPa)
Mo_2GaC	Mo-C	4	2.12	0.92	5.24	0.0478	40.83	9.6
	Mo-Mo	2	4.27	0.43	43.11	0.0478	0.53	
Nb_2AsC	Nb-C	4	2.23	1.09	8.58	0.0178	22.06	6.7
	Nb-Nb	2	3.73	0.42	40.16	0.0178	0.63	
Nb2InC	Nb-C	4	2.19	0.99	4.89	0.0134	51.29	7.9
	Nb-Nb	2	4.88	0.21	54.07	0.0134	0.19	
Ti_2GeC	Ti-C	4	2.12	1.06	5.57	0.0181	44.03	11.6
	Ti-Ti	2	4.17	0.58	42.26	0.0181	0.81	

6.5. Optical properties

The calculated optical properties of Mo_2GaC, Nb_2AsC, Nb_2InC, and Ti2GeC for photon energies up to 20 eV for polarization vectors [100] and [001] are shown in Figs. 6.5(a) – 6.5(p). For the metallic compounds both inter-band and intra-band transitions contribute to dielectric function. As the investigated materials are metallic, which is evident from our calculated band structures, a Drude term [54,55] with unscreened plasma frequency 5 eV and damping 0.05 eV has been used. Its effect is to enhance the low energy part of the spectrum. We have used a 0.5 eV Gaussian smearing for all calculations.

Dielectric function is the most general property of a solid, which modifies the incident electromagnetic wave of light. The real parts of the dielectric functions of the four nanolaminates for two different polarizations are shown in Figs. 6.5(a) and 6.5(b) along with the measured values for $NbC_{0.87}$ [56] and TiC [57]. All the phases exhibit metallic characteristics in the energy range for which $\varepsilon_1(\omega) < 0$. We observe that the highest peak centered at 3.7 eV for $NbC_{0.87}$ is shifted to the left with a sharp peak at around 2.66 eV for Nb_2AsC, and 2.20 eV for Nb_2InC for the polarization direction [100]. We also see that the highest peak positioned at 1.9 eV for TiC is shifted to the left with a sharp peak at around 0.9 eV for Ti_2GeC. A highest peak for Mo_2GaC is found at around 2.77 eV. In Figs. 6.5(c) and 6.5(d), the imaginary part of the dielectric functions of the four MAX superconductors for both polarization directions approaches zero from above at about 10.5 – 11.75 eV. The peak of the imaginary part of the dielectric function is related to the electron excitation. In imaginary part ε_2, the peak for <1.2 eV is due to the intra-band transitions.

In optics, the index of refraction of an optical medium is a dimensionless number that describes how light, or any other radiation, propagates through that medium. The real parts of the refractive indices for the incident light directions [100] and [001] are shown in Figs. 6.5(e) and 6.5(f), respectively. The nature of the variation of the refractive indices of Mo_2GaC, Nb_2AsC, and Nb_2InC with the incident light

energy is almost same but for Ti_2GeC it shows different qualitative features except in the 10 – 15 eV regions for the both directions. The static refractive indices of the four phases for polarization direction [100] are 17.53, 10.46, 7.98, and 84.56, respectively. On the other hand, the corresponding values for these compounds for direction [001] are 7.49, 7.88, 6.06, and 84.58, respectively. The large value of n for Ti_2GeC implies that the velocity of light in Ti_2GeC is reduced by many times with compared to other three phases when light enters into Ti_2GeC from air. The extinction coefficients of the four nanolaminates are presented in Figs. 6.5(g) and 6.5(h) for the polarization vectors [100] and [001], respectively. The extinction coefficients of the four MAX superconductors exhibit the same qualitative features in the entire energy range excepting 0 – 3.8 eV.

The absorption coefficient provides the information regarding optimum solar energy conversion efficiency and it indicates how far light of a specific energy (frequency) can penetrate into the material before being absorbed. In Figs. 6.5(i) and 6.5(j) the four nanolaminates confirm their metallic nature showing absorption band in the low energy range. For Mo_2GaC, Nb_2AsC, Nb_2InC, and Ti_2GeC the absorption spectra for both directions arise sharply below 7 eV and their highest peaks for the polarization direction [100] arise at 7.7, 8.1, 7.4, and 6.2 eV, respectively. The highest peaks for the incident light direction [001] are found at around 7.2, 8.2, 7.0, and 6.1 eV, respectively. The highest peaks are associated with the transition from A/C p to M d states.

The energy loss spectrum describes the energy loss of a fast electron traversing inside the material [58]. The frequency associated with the highest peak of energy loss spectrum is defined as the bulk plasma frequency ω_p, which appears at $\varepsilon_2 < 1$ and $\varepsilon_1 = 0$ [55,59]. The energy loss functions for the compounds under study are displayed in Figs. 6.5(k) and 6.5(l). In the energy loss spectra, we find that the plasma frequencies of Mo_2GaC, Nb_2AsC, Nb_2InC, and Ti_2GeC for both incident light directions are nearly equal to 17.2, 16.5, 14.8, and 14.5 eV, respectively. These materials will be transparent if the incident light has frequency greater than their respective plasma frequency.

Figs. 6.5(m) and 6.5(n) represent the reflectivity spectra for the two different polarizations as a function of incident light energy. For comparison, the measured spectra of $NbC_{0.98}$ [56] and TiC [57] are displayed in the plot. It is seen that the reflectivity spectra for the four phases exhibit no significant changes in the energy range 1.8 – 6.0 eV and the values are always above 44%. This almost constant reflectance in the visible region (up to 3.1 eV) should make the four phases appear metallic gray. Further, the spectra of the different phases rise to reach maximum value of ~ 0.93 – 0.97 in the UV region (between 10.48 and 11.65 eV). According to Li *et al*. [56] the MAX compound Ti_3SiC_2 having the average reflectivity ~ 44% in the visible light region, show the nonselective characteristic that is responsible for reducing solar heating. Therefore, we can say that the four MAX compounds Mo_2GaC, Nb_2AsC, Nb_2InC, and Ti_2GeC are also candidate materials for coating to minimize the solar heating.

The optical conductivity means the electrical conductivity in the presence of an alternating electric field. The term 'optical' here covers the entire frequency range, and is not restricted only to the visible region of the spectrum. The optical conductivity may be expected to be a good gauge of photoconductivity. Absolutely, it was illustrated in $Nd_2CuO_{4-\delta}$ [60] by synchronous measurements of both the optical and photoconductivity. The real parts of optical conductivity for the four MAX superconductors are shown in Figs. 6.5(o) and 6.5(p). For all the phases, it is seen that optical conductivity occurs at zero photon energy due to the overlapping of the valence and conduction bands at the Fermi level. Therefore, photocurrent can be generated within a wide range of photon energies. These four nanolaminates have their highest peaks in optical conductivity in the energy range 0.8 – 6.0 eV. Therefore, the studied four superconducting MAX phase compounds will be highly electrically conductive when the incident photon has energy within this range. The enhancement of electrical conductivity due to absorption of electromagnetic radiation of photon energy greater than 11.2 eV is so small. The measured optical conductivity of $NbC_{0.98}$ [56] is also shown in the figure for comparison.

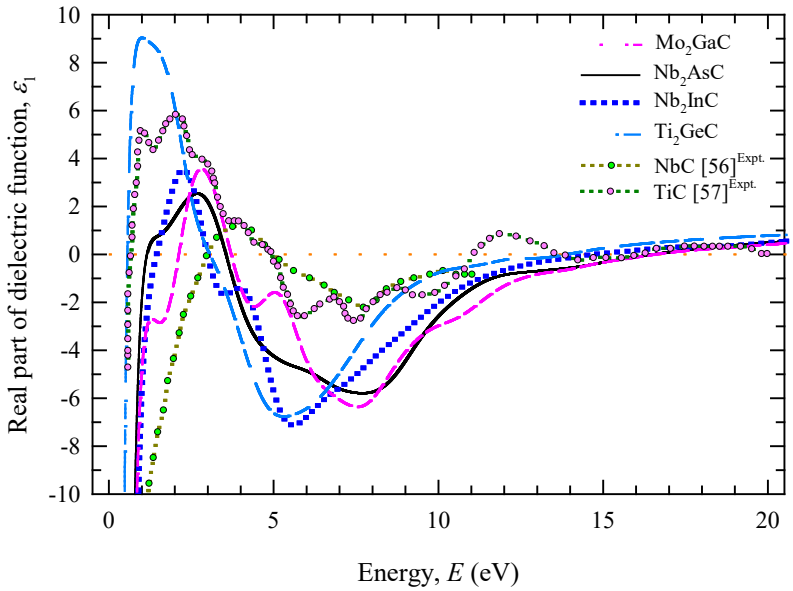

Fig. 6.5(a). Real part of the dielectric function ε_1 of Mo_2GaC, Nb_2AsC, Nb_2InC, and Ti_2GeC for the incident light direction [100].

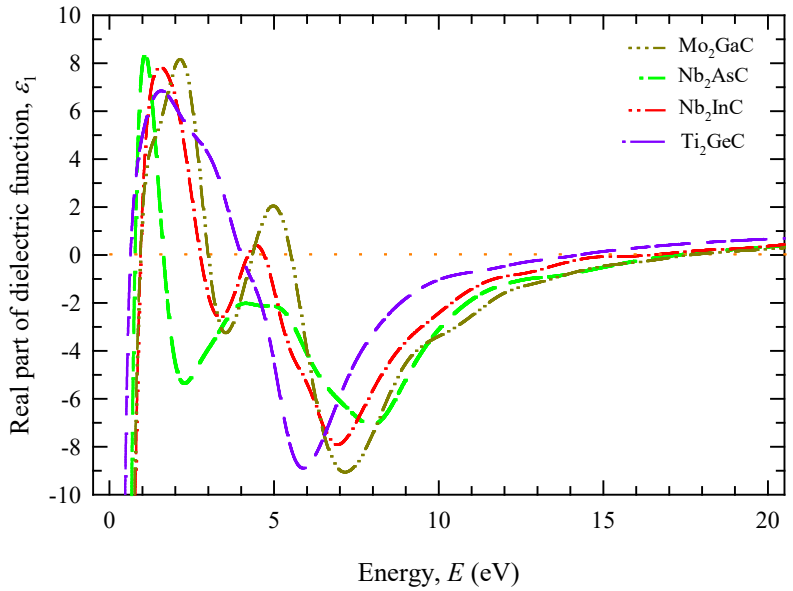

Fig. 6.5(b). Real part of the dielectric function ε_1 of Mo_2GaC, Nb_2AsC, Nb_2InC, and Ti_2GeC for the incident light direction [001].

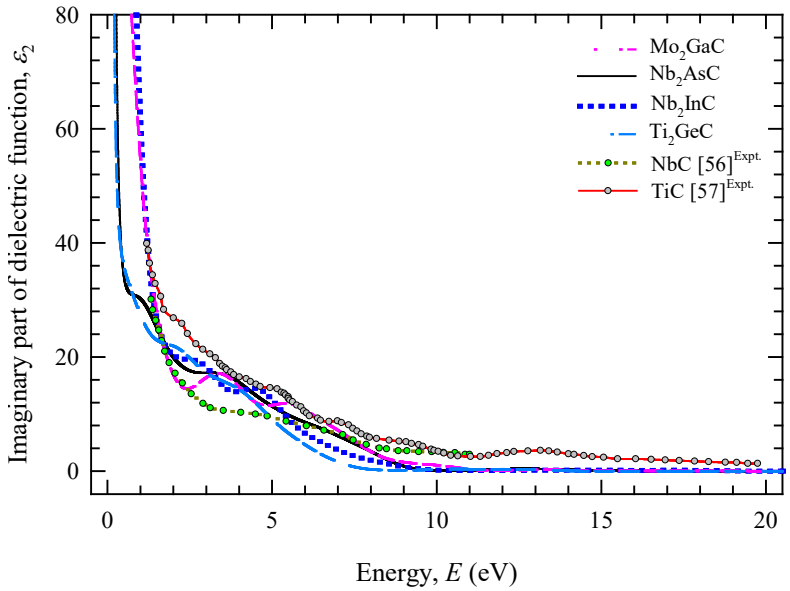

Fig. 6.5(c). Imaginary part of the dielectric function ε_2 of Mo_2GaC, Nb_2AsC, Nb_2InC, and Ti_2GeC for the incident light direction [100].

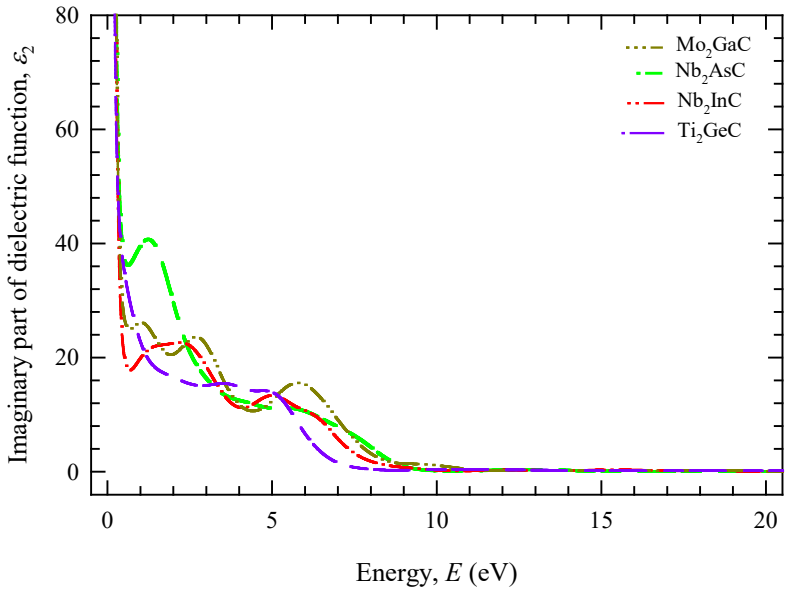

Fig. 6.5(d). Imaginary part of the dielectric function ε_2 of Mo_2GaC, Nb_2AsC, Nb_2InC, and Ti_2GeC for the incident light direction [001].

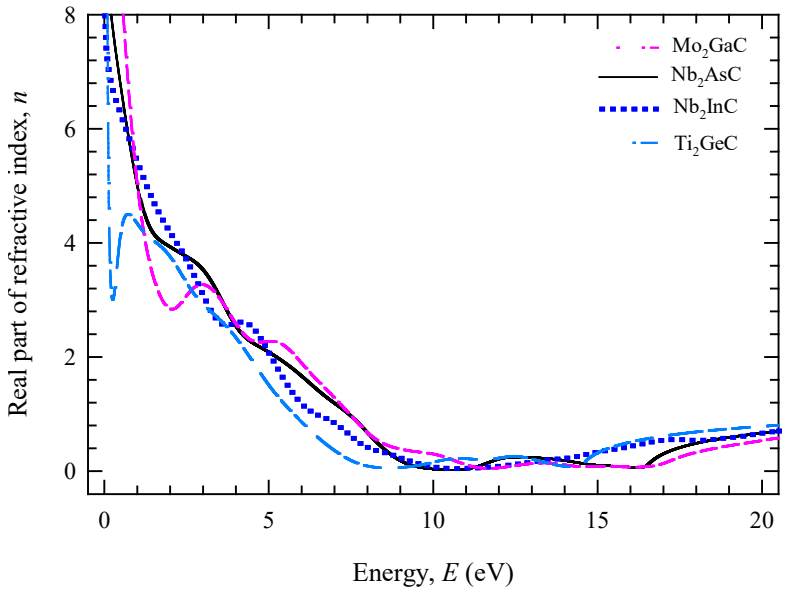

Fig. 6.5(e). Real part of the refractive index n of Mo_2GaC, Nb_2AsC, Nb_2InC, and Ti_2GeC for the incident light direction [100].

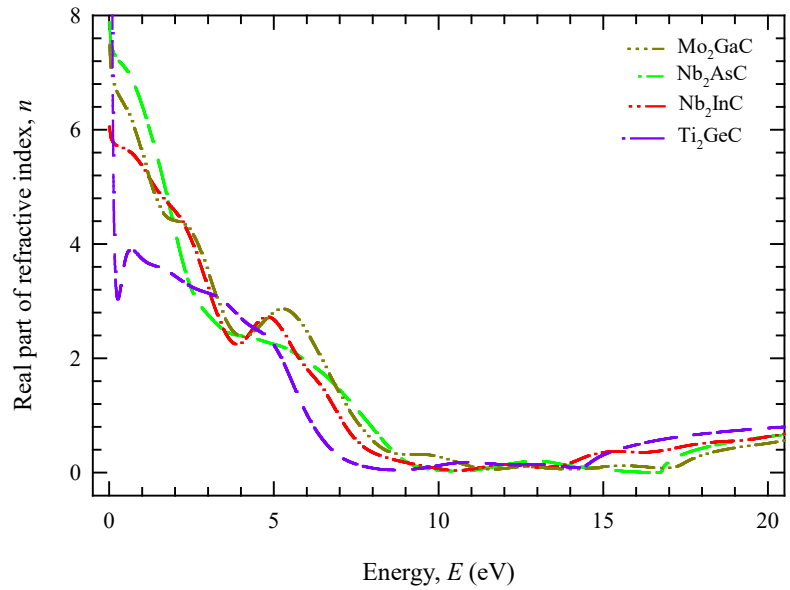

Fig. 6.5(f). Real part of the refractive index n of Mo_2GaC, Nb_2AsC, Nb_2InC, and Ti_2GeC for the incident light direction [001].

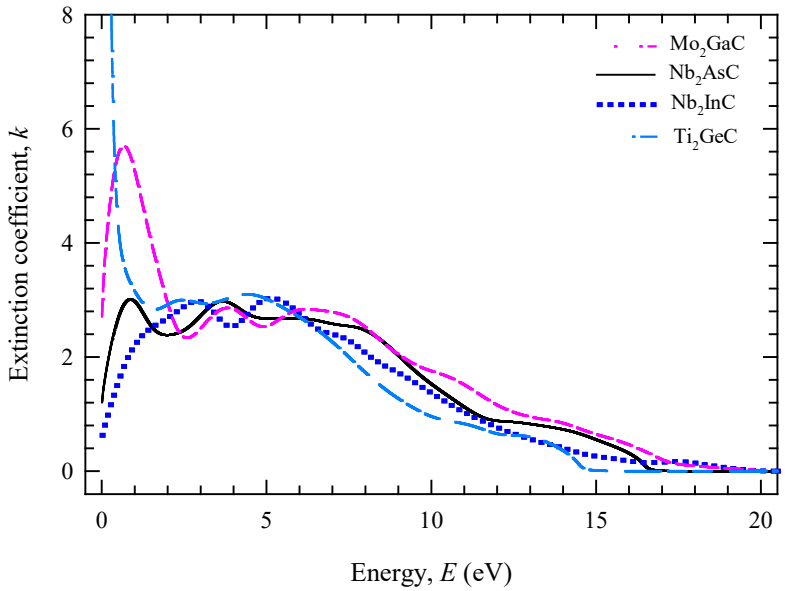

Fig. 6.5(g). Extinction coefficient k of Mo_2GaC, Nb_2AsC, Nb_2InC, and Ti_2GeC for the incident light direction [100].

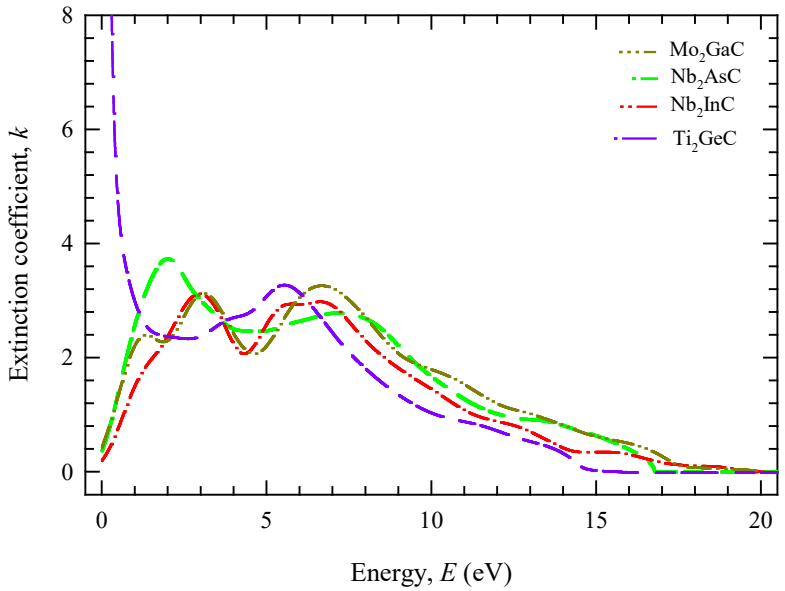

Fig. 6.5(h). Extinction coefficient k of Mo_2GaC, Nb_2AsC, Nb_2InC, and Ti_2GeC for the incident light direction [001].

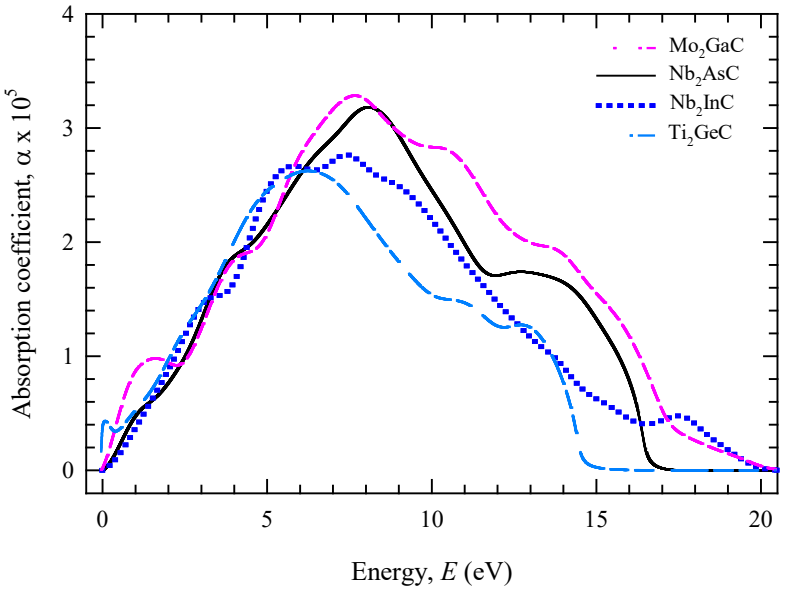

Fig. 6.5(i). Absorption coefficient α of Mo_2GaC, Nb_2AsC, Nb_2InC, and Ti_2GeC for the incident light direction [100].

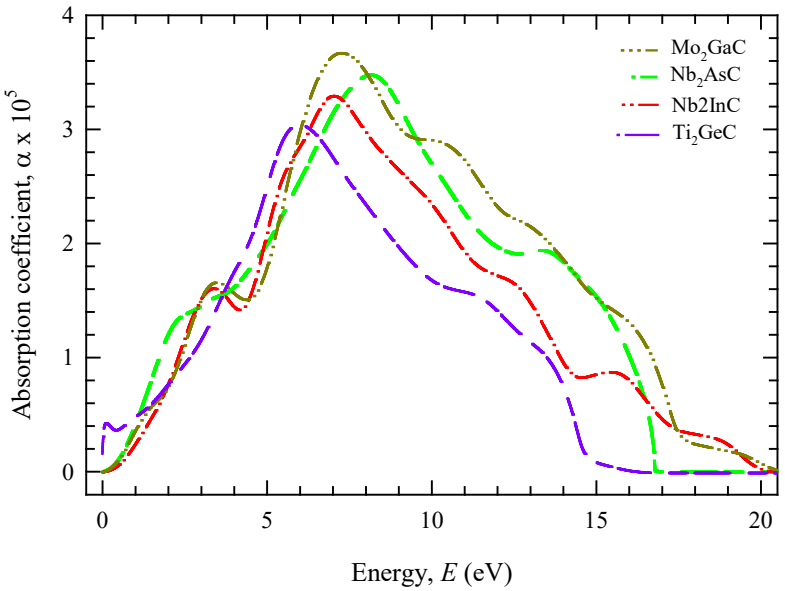

Fig. 6.5(j). Absorption coefficient α of Mo_2GaC, Nb_2AsC, Nb_2InC, and Ti_2GeC for the incident light direction [001].

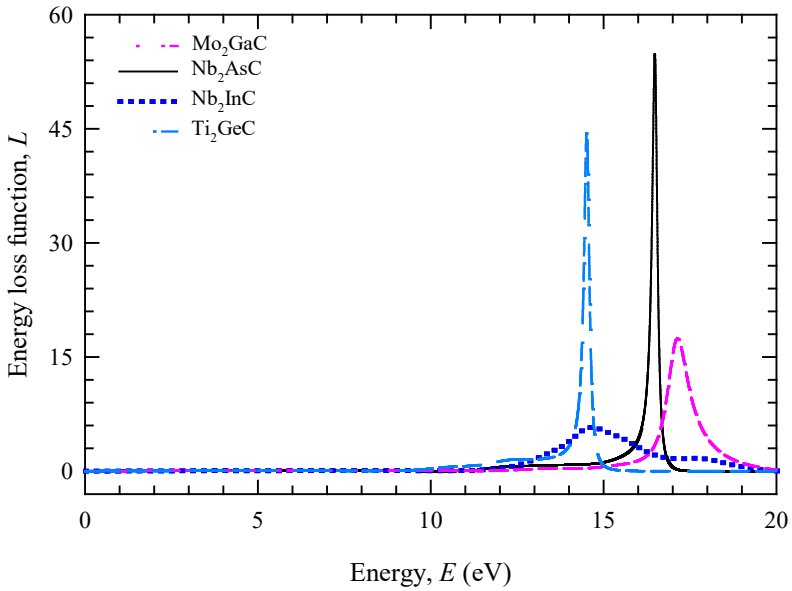

Fig. 6.5(k). Energy loss function L of Mo_2GaC, Nb_2AsC, Nb_2InC, and Ti_2GeC for the incident light direction [100].

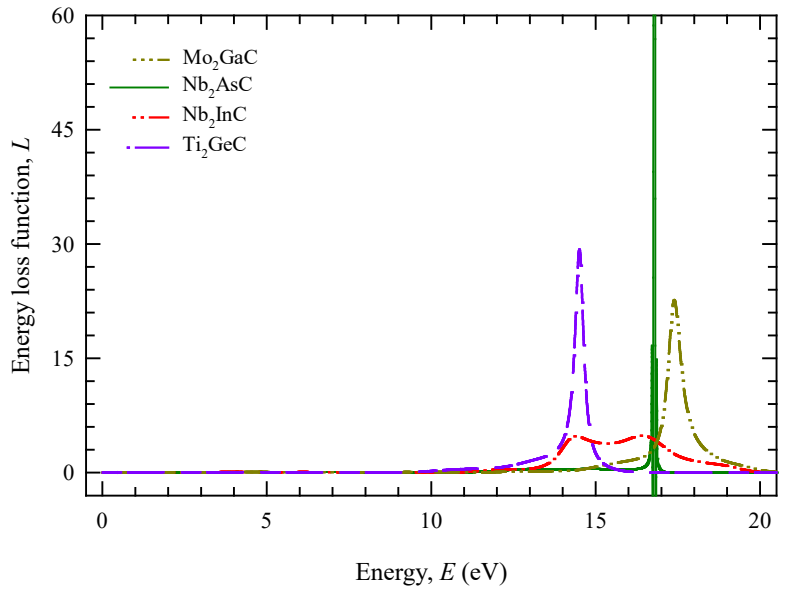

Fig. 6.5(*l*). Energy loss function L of Mo_2GaC, Nb_2AsC, Nb_2InC, and Ti_2GeC for the incident light direction [001].

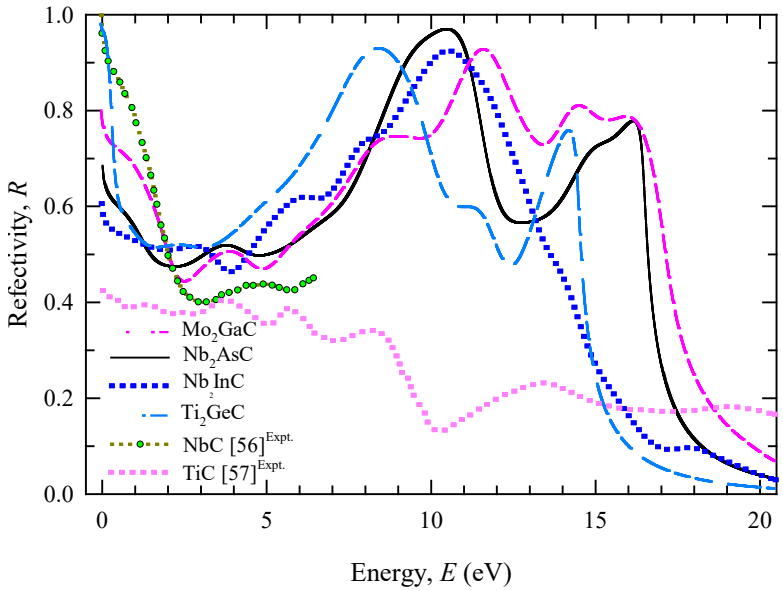

Fig. 6.5(m). Reflectivity R of Mo_2GaC, Nb_2AsC, Nb_2InC, and Ti_2GeC for the incident light direction [100].

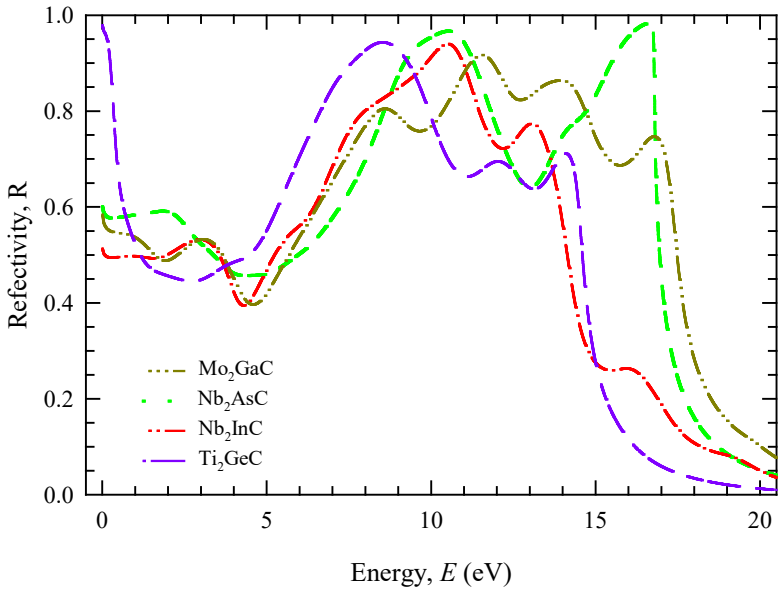

Fig. 6.5(n) Reflectivity R of Mo_2GaC, Nb_2AsC, Nb_2InC, and Ti_2GeC for the incident light direction [001].

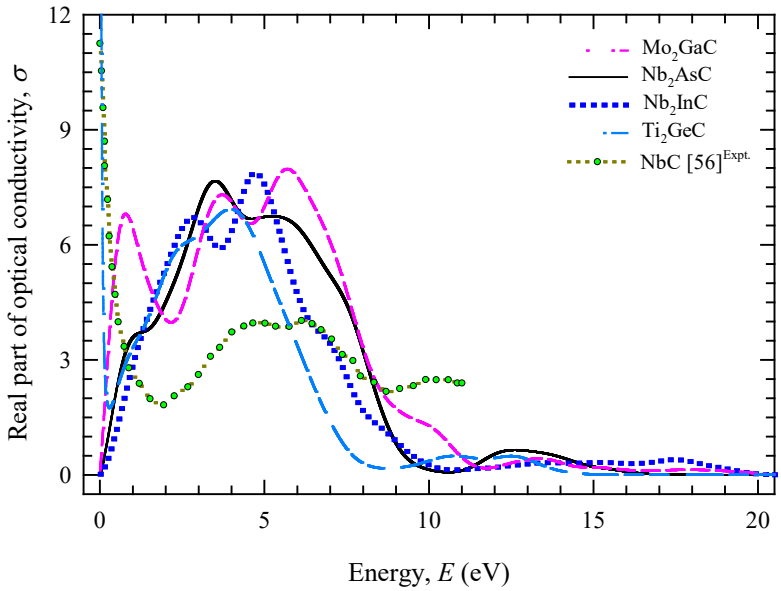

Fig. 6.5(o) Real part of the optical conductivity σ of Mo_2GaC, Nb_2AsC, Nb_2InC, and Ti_2GeC for the incident light direction [100].

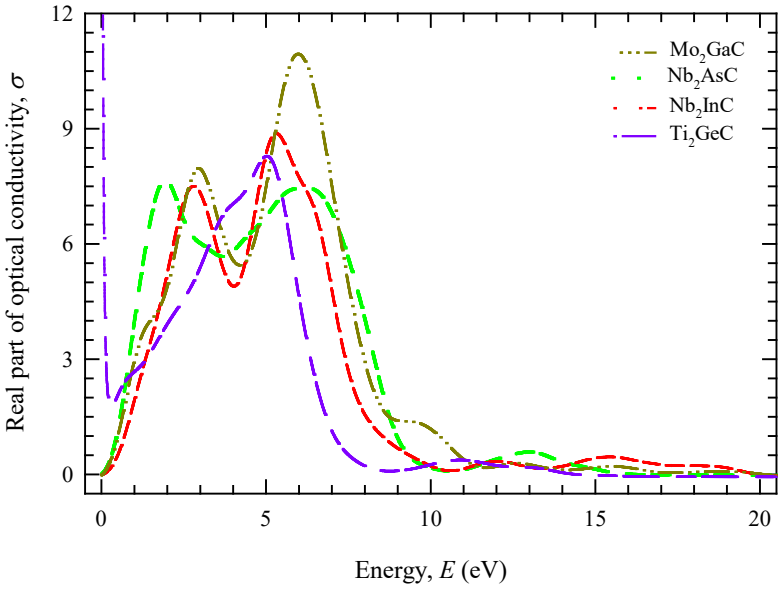

Fig. 6.5(p) Real part of the optical conductivity σ of Mo_2GaC, Nb_2AsC, Nb_2InC, and Ti_2GeC for the incident light direction [001].

6.6. Thermodynamic properties

The quasi-harmonic Debye model is applied to investigate the thermodynamic properties in the temperature range from 0 to 1200 K. The pressure effect is studied in the 0–50 GPa range.

The dependence of the isothermal bulk modulus of the four superconducting MAX phases on temperature and pressure is shown in Figs. 6.6(a) and 6.6(b), respectively. Our results reveal that all B values (larger for Nb_2AsC) are nearly flat for temperature below 150 K and above 150 K, B for Ti_2GeC decreases at a slightly faster rate than other compounds. Figure 6.6(b) shows the pressure variation of room temperature (300 K) bulk modulus along with the results for Ti_2GeC calculated by Fu et al. [20]. Our results for Ti_2GeC show fair agreement with these results. It is observed that B increases with increasing pressure at a given temperature and decreases with increasing temperature at a given pressure, which is harmonious with the trend of volume.

Figure 6.6(c) presents the temperature variation of Debye temperature Θ_D at zero pressure of Mo_2GaC, Nb_2AsC, Nb_2InC, and Ti_2GeC and Fig. 6.6(d) shows Debye temperature at 300 K as a function of pressure. We observe that Θ_D decreases non-linearly with increasing temperature for all the phases. On the other hand, the pressure dependent Debye temperature exhibits a non-linear increase. The variation of Θ_D with pressure and temperature assures that the thermal vibration frequency of atoms in the MAX phases changes with pressure and temperature.

The specific heat capacity, C_V at constant-volume and C_P at constant-pressure for Mo_2GaC, Nb_2AsC, Nb_2InC, and Ti_2GeC as a function of temperature are shown in Figs. 6.6(e) and 6.6(f). The experimental values of specific heat at constant pressure for a typical superconducting MAX phase Nb_2SnC [61] are displayed in Fig. 6.6(e) for comparison with our results. These experimental results roughly coincide with our values. We see that both heat capacities increase with increasing temperature. These results indicate that phonon thermal softening occurs when the temperature is raised.

There is a difference between C_P and C_V in the normal state for the phases due to the thermal expansion caused by anharmonic effects. This difference is given by $C_P - C_V = \alpha_V^2(T)BTV$, where α_V is the volume thermal expansion coefficient. The specific heat obeys the Debye T^3 power-law in the low temperature limit. The anharmonic effect on heat capacity is restrained at the temperature above 300 K, and C_V approaches the classical asymptotic limit of $C_V = 3nNk_B = 99.8$ J/mol K. These results imply that the interactions between ions in the nanolaminates have great effect on heat capacities particularly at low temperatures. To evaluate the electronic contribution to specific heat through the Sommerfeld constant γ within the free electron model: $\gamma = (1/3)\pi^2 k_B^2 N(E_F)$, we can use $N(E_F)$ from the investigated DOS for the four nanolaminates. This scheme gives the values 5.4, 2.9, 4.3, and 3.6 mJ mol^{-1} K^{-2} for Mo_2GaC, Nb_2AsC, Nb_2InC, and Ti_2GeC, respectively.

We can determine the electron-phonon coupling constant (λ) using McMillan's relation [62]. Taking the known values of T_C, calculated Θ_D with the repulsive Coulombic pseudopotential ($\mu^* = 0.10$), the estimated λ values are 0.48, 0.40, 0.57, and 0.56 for Mo_2GaC, Nb_2AsC, Nb_2InC, and Ti_2GeC, respectively. These values are similar in several studied MAX phases [63,64] and indicate that all the phases are moderately coupled superconductors.

The volume thermal expansion coefficient, α_V as a function of temperature and pressure are shown in Figs. 6.6(g) and 6.6(h), respectively. The coefficients of all phases under study increase rapidly with increasing temperature up to 300 K but at temperature above 300 K the increment is gradual. On the contrary, at a constant temperature, the expansion coefficients decrease rapidly with increasing pressure but at different rates. It is established that the volume thermal expansion coefficient is inversely related to the bulk modulus of a material. The calculated values of α_V at 300 K for Mo_2GaC, Nb_2AsC, Nb_2InC, and Ti_2GeC are 2.40×10^{-5} K^{-1}, 2.04×10^{-5}, 2.42×10^{-5}, and 3.155×10^{-5} K^{-1}, respectively. For Nb_2AsC, the estimated linear expansion coefficient ($\alpha = \alpha_V/3$) is 6.8×10^{-6} K^{-1}, which agrees rather well with the experimental value of $\alpha = 7.3 \times10^{-6}$ K^{-1} [13].

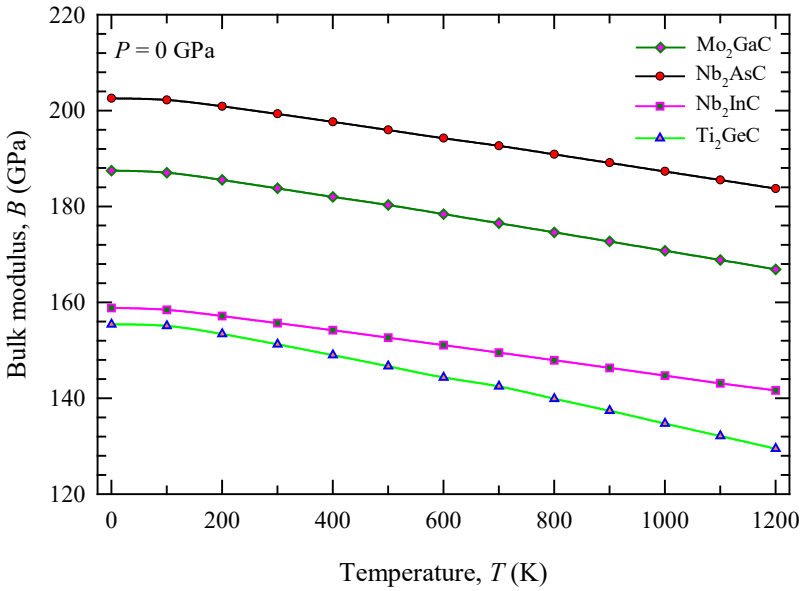

Fig. 6.6(a). Temperature dependence of Bulk modulus B of the four MAX phase superconductors Mo_2GaC, Nb_2AsC, Nb_2InC, and Ti_2GeC.

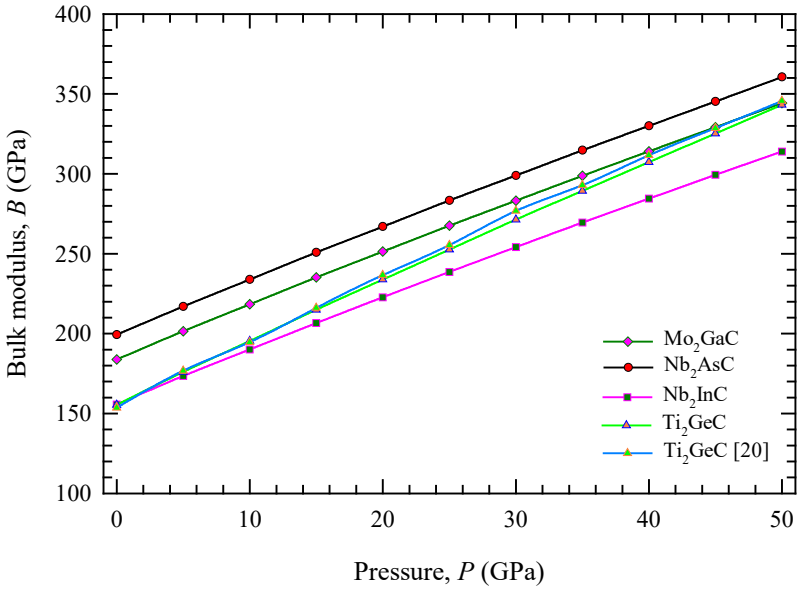

Fig. 6.6(b). Pressure dependence of Bulk modulus B of the four MAX phase superconductors Mo_2GaC, Nb_2AsC, Nb_2InC, and Ti_2GeC.

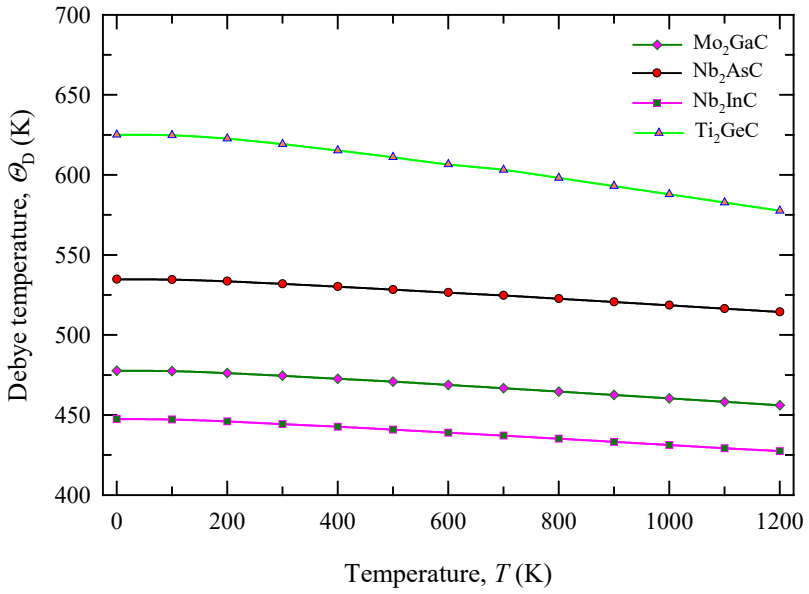

Fig. 6.6(c) Temperature dependence of Debye temperature Θ_D of the four MAX superconductors Mo_2GaC, Nb_2AsC, Nb_2InC, and Ti_2GeC.

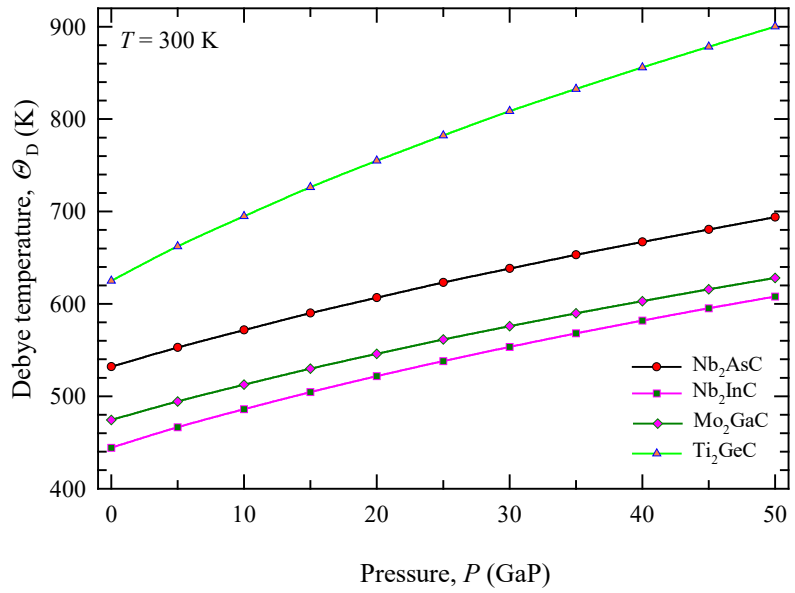

Fig. 6.6(d). Pressure dependence of Debye temperature Θ_D of the four MAX superconductors Mo_2GaC, Nb_2AsC, Nb_2InC, and Ti_2GeC.

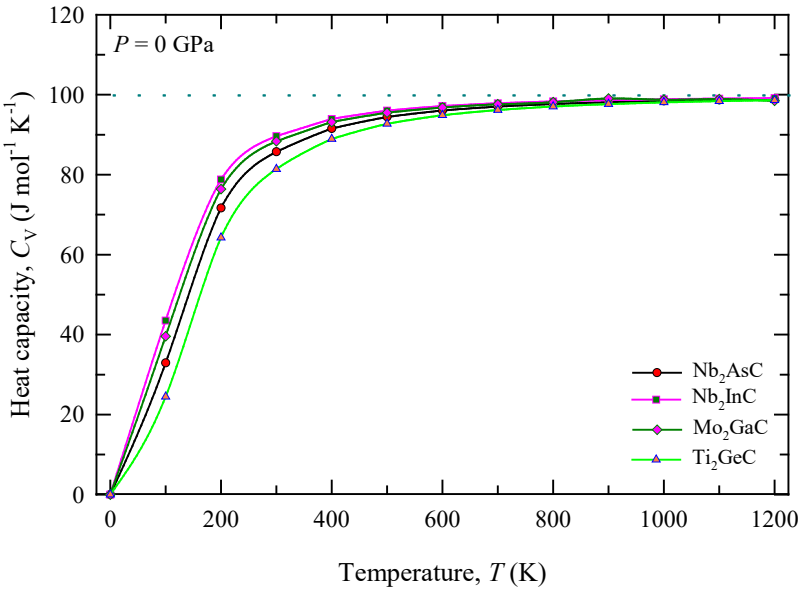

Fig. 6.6(e) Temperature dependence of heat capacity C_V of the four MAX phase superconductors Mo_2GaC, Nb_2AsC, Nb_2InC, and Ti_2GeC.

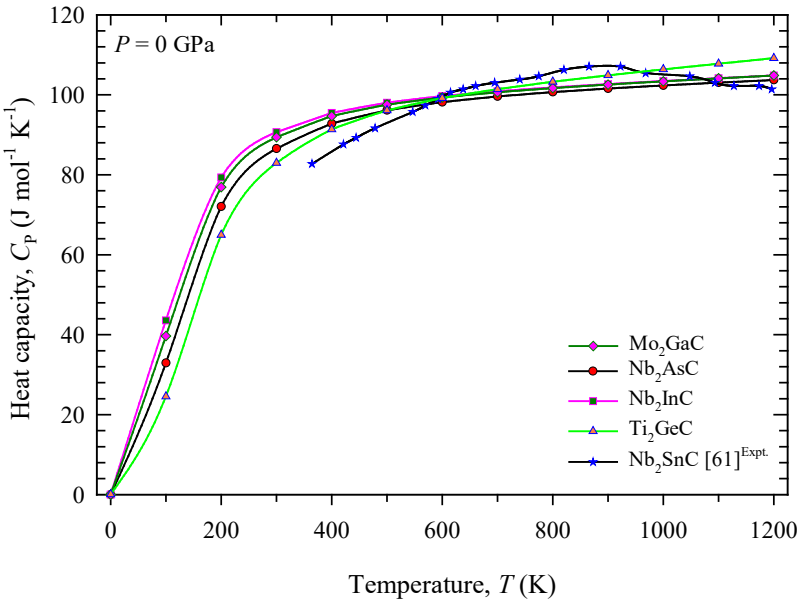

Fig. 6.6(f) Temperature dependence of heat capacity C_P of the four MAX phase superconductors Mo_2GaC, Nb_2AsC, Nb_2InC, and Ti_2GeC.

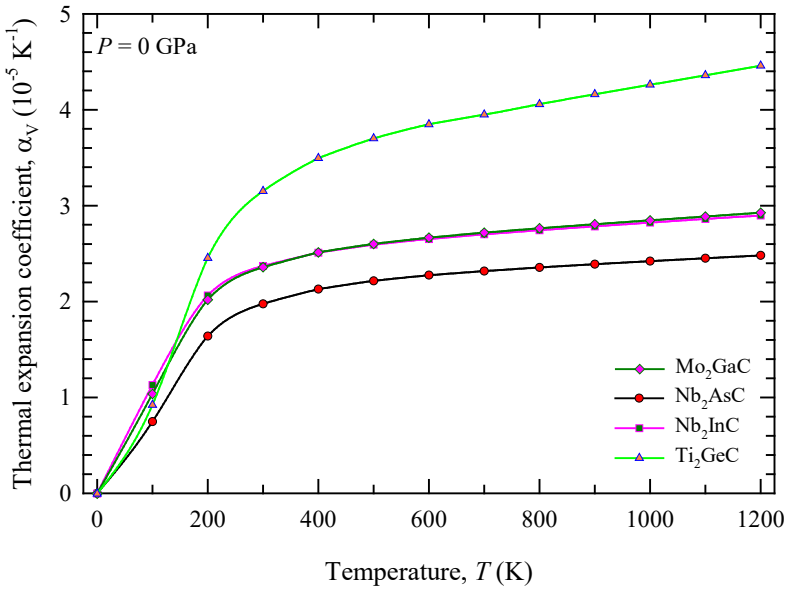

Fig. 6.6(g) Temperature dependence of thermal expansion coefficient α_V of the four MAX phases Mo_2GaC, Nb_2AsC, Nb_2InC, and Ti_2GeC.

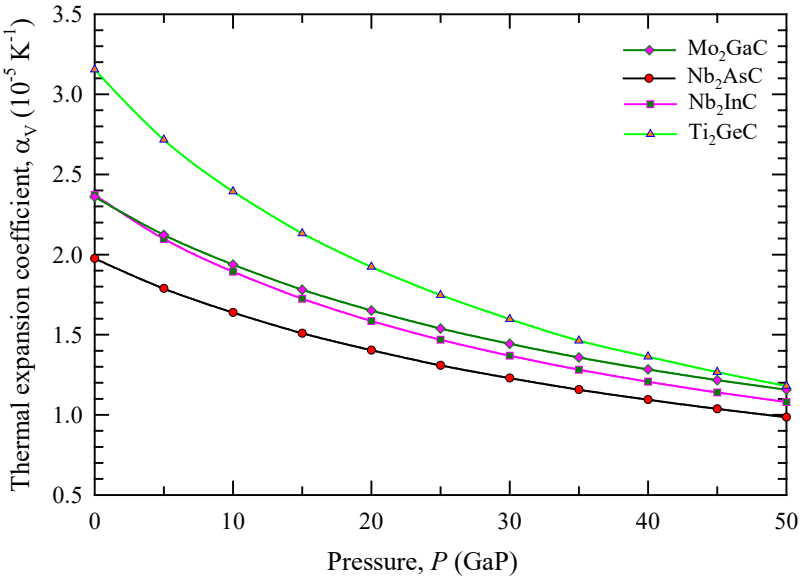

Fig. 6.6(h) Pressure dependence of thermal expansion coefficient α_V of the four MAX phases Mo_2GaC, Nb_2AsC, Nb_2InC, and Ti_2GeC.

References

[1] W. Kohn and L.J. Sham, "*Self-Consistent Equations Including Exchange and Correlation Effects*", Phys. Rev. **140**, (1965) A1133.

[2] S.J. Clark, M.D. Segall, C.J. Pickard, P.J. Hasnip, M.I.J. Probert, K. Refson, and M.C. Payne, "*First principles methods using CASTEP*", Z. Kristallogr. **220** (2005) 567.

[3] J.P. Perdew, K. Burke, and M. Ernzerhof, "*Generalized Gradient Approximation Made Simple*", Phys. Rev. Lett. **77** (1996) 3865.

[4] J.A. White and D.M. Bird, "*Implementation of gradient-corrected exchange-correlation potentials in Car-Parrinello total-energy calculations*", Phys. Rev. B **50** (1994) 4954.

[5] H.J. Monkhorst and J.D. Pack, "*Special points for Brillouin-zone integrations*", Phys. Rev. B **13** (1976) 5188.

[6] T.H. Fischer and J. Almlof, "*General methods for geometry and wave function optimization*", J. Phys. Chem. **96** (1992) 9768.

[7] M.A. Blanco, E. Francisco, and V. Luaña, "*GIBBS: isothermal-isobaric thermodynamics of solids from energy curves using a quasi-harmonic Debye model*", Comput. Phys. Commu. **158** (2004) 57.

[8] F. Birch, "*Finite strain isotherm and velocities for single-crystal and polycrystalline NaCl at high pressures and 300°K*", J. Geophys. Res.: Solid Earth **83** (1978) 1257.

[9] I.R. Shein and A.L. Ivanovskii, "*Elastic properties of superconducting MAX phases from first-principles calculations*," Phys. Status. Solidi B **248** (2011) 228.

[10] M.F. Cover, O. Warschkow, M.M.M. Bilek, and D.R. McKenzie, "*A comprehensive survey of M_2AX phase elastic properties*", J. Phys.: Condens. Matter **21** (2009) 305403.

[11] I.R. Shein, and A.L. Ivanovskii, "*Structural, elastic, electronic properties and Fermi surface for superconducting Mo_2GaC in comparison with V_2GaC and Nb_2GaC from first principles*", Physica C **470** (2010) 533.

[12] M. Khazae, M. Arai, T. Sasaki, M. Estili, and Y. Sakka, "*The effect of the interlayer element on the exfoliation of layered Mo_2AC (A = Al, Si, P, Ga, Ge, As or In) MAX phases into two-dimensional Mo_2C nanosheets*", Sci. Technol. Adv. Matter. **15** (2014) 014208.

[13] T.H. Scabarozi, S. Amini, O. Leaffer, A. Ganguly, S. Gupta, W. Tambussi, S. Clipper, J.E. Spanier, M.W. Barsoum, J.D. Hettinger and S.E. Lofland, "*Thermal expansion of select $M_{n+1}AXn$ (M = early transition metal, A = A group element, X = C or N) phases measured by high temperature x-ray diffraction and dilatometry*", J. Appl. Phys. **105** (2009) 013543.

[14] A. Bouhemadou, "*Calculated structural and elastic properties of M_2InC (M = Sc, Ti, V, Zr, Nb, Hf, Ta)*", Mod. Phys. Lett. B **22** (2008) 2063.

[15] M. Romero, and R. Escamilla, "*Pressure effect on the structural, elastic and electronic properties of Nb_2AC (A = S and In) phases; ab initio study*", Comp. Mater. Sci. **81** (2014) 184.

[16] M.G. Brik, N.M. Avram, and C.N. Avram, "*Ab initio calculations of the electronic, structural and elastic properties of Nb_2InC*", Comp. Mater. Sci. **63** (2012) 227.

[17] A. Bouhemadou, "*Calculated structural, electronic and elastic properties of M_2GeC (M =Ti, V, Cr, Zr, Nb, Mo, Hf, Ta and W)*", Appl. Phys. A **96** (2009) 959.

[18] S. Cui, W. Feng, H. Hu, Z. Lv, G. Zhang, and Z. Gong, "*First-principles studies of the electronic and elastic properties of Ti_2GeC*", Solid State Commun. **151** (2011) 491.

[19] G. Hug, "*Electronic structures of and composition gaps among the ternary carbides Ti_2MC*", Phys. Rev. B **74** (2006) 184113.

[20] H. Fu, W. Liu, Y. Ma, and T. Gao, "*Prediction study of the axial compressibility, anisotropy and dynamic properties for single crystal Ti_2GeC*", J. Alloys Compd. **506** (2010) 22.

[21] M.W. Barsoum, "*The $M_{N+1}AX_N$ phases: A new class of solids; thermodynamically stable nanolaminates*," Prog. Solid State. Chem. **28** (2000) 201.

[22] O. Beckmann, H. Boller, and H. Nowotny, "*Neue H-Phasen*," Monatsh. Chem. **99** (1968) 1580.

[23] R.S. Kumar, S. Rekhi, A.L. Comelius, and M.W. Barsoum, "*Compressibility of Nb_2AsC to 41 GPa*", Appl. Phys. Lett. **8**6 (2005) 111904.

[24] W. Jeitschko, H. Nowotny, and F. Benesovsky, "*Die H-Phasen Ti_2TlC, Ti_2PbC, Nb_2InC, Nb_2SnC and Ta_2GaC*," Monatsh. Chem. **95** (1964) 431.

[25] W. Jeitschko, H. Nowotny, and F. Benesovsky, "*Die H-phasan Ti_2InC, Hf_2InC and Ti_2GeC*", Monatsh. Chem. **94** (1963) 1201.

[26] M.W. Barsoum, "*Physical Properties of the MAX phases Encyclopedia of Materials: Science and Technology*", Amsterdam, Elsevier, 2004.

[27] N.A. Phatak, S.K. Sexena, Y.W. Fei, and J.Z. Hu, "*Synthesis and structural stabily of Ti_2GeC*", J. Alloys Compd. **474** (2009) 174.

[28] M.Y. Gamarnik and M.W. Barsoum, "*Bond lengths in the ternary compounds Ti_3SiC_2, Ti_3GeC_2 and Ti_2GeC*", J. Matter. Sci. **34** (1999) 169.

[29] B. Manoun, S.K. Saxena, H.P. Liermann, R.P. Gulve, E. Hoffman, M.W. Barsoum, G. Hug and C.S. Zha, "*Compression of Zr_2InC to 52GPa*", Appl. Phys. Lett. **85** (2004) 1514.

[30] B. Manoun, F.X. Zhang, S.K. Saxena, T. El-Raghy and M.W. Barsoum, "*X-ray high-pressure study of Ti_2AlN and Ti_2AlC*", J. Phys. Chem. Solids **67** (2006) 2091.

[31] S.R. Kulkarni, R. Selva Vennila, N.A. Phatak, S.K. Sexena, C.S. Zha, T. El-Raghy, M.W. Barsoum, W. Luo and R. Ahuja, "*Study of Ti_2SC under compression up to 47 GPa*", J. Alloy Comp. **448** (2008) L1.

[32] B. Manoun, R.P. Gulve, S.K. Saxena, S. Gupta, M.W. Barsoum and C.S. Zha, "*Compression behavior of M_2AlC (M=Ti, V, Cr, Nb, and Ta) phases to above 50GPa*", Phys. Rev. B **73** (2006) 024110.

[33] B. Manoun, S.K. Saxena, R. Gulve, H.P. Liermann, A. Ganguly, M.W. Barsoum, and C.S. Zha, "*Compression of $Ti_3Si_{0.5}Ge_{0.5}C_2$ to 53 GPa*", Appl. Phys. Lett. **84** (2004) 2799.

[34] A. Onedara, H. Hirano, T.Yuasa, N.F. Gao, and Y. Miyamoto, "*Static compression of Ti_3SiC_2 to 61 GPa*", Appl. Phys. Lett. **74** (1999) 3782.

[35] M. Born, "*On the stability of crystal lattices*", Math. Proc. Camb. Philos. Soc. **36** (1940) 160.

[36] W. Voigt, "*Ueber die Beziehung zwischen den beiden Elasticitätsconstanten isotroper Körper*", Ann. Physik 274 (1889) 573.

[37] A. Reuss, "*Berechnung der Fließgrenze von Mischkristallen auf Grund der Plastizitätsbedingung für Einkristalle*", *Z. Angew. Math. Mech*. **9** (1929) 49.

[38] R. Hill, "*The Elastic Behaviour of a Crystalline Aggregate*", *Proc. Phys. Soc*. A **65** (1952) 349.

[39] S.F. Pugh, "*Relations between the elastic moduli and the plastic properties of polycrystalline pure metals*", Philos. Mag. **45** (1954) 823.

[40] J. Haines, J. M. Léger, and G. Bocquillon, "*Synthesis and design of Superhard Materials*", Annu. Rev. Mater. Res. **31** (2001) 1

[41] W.Y. Ching, Y. Mo, S. Aryal and P. Rulis, "*Intrinsic Mechanical Properties of 20 MAX-Phase Compounds*", J. Am. Ceram. Soc. **96** 2292 (2013).

[42] M.T. Nasir, M.A. Hadi, S.H. Naqib, F. Parvin, A.K.M.A. Islam, M. Roknuzzaman, M.S. Ali, "*Zirconium Metal Based MAX Phases Zr_2AC (A = Al, Si, P, and S): A First-principles Study*", Int. J. Mod. Phys. B **28** (2014) 1550022.

[43] J.H. Xu, and A.J. Freeman, "*Band filling and structural stability of cubic trialuminides: YAl_3, $ZrAl_3$, and $NbAl_3$*", Phys. Rev. B **40** (1986) 11927.

[44] D. Music, Z. Sun, and J.M. Schneider, "*Structure and bonding of M_2SbP (M=Ti,Zr,Hf)*", Phys. Rev. B **71** (2006) 092102.

[45] G. Hug and E. Fries, "*Full-potential electronic structure of Ti_2AlC and Ti_2AlN*", Phys. Rev**.** B **65** (2002) 113104.

[46] S.V. Halilov, D.J. Singh, and D.A. Papaconstantopoulos, "*Soft modes and superconductivity in the layered hexagonal carbides V_2CAs, Nb_2CAs, and Nb_2CS*", Phys. Rev. B **65** (2002) 174519.

[47] I.R. Shein and A.L. Ivanovskii, "*Ab Initio Calculation of the Electronic Structure, Fermi Surface, and Elastic Properties of the New 7.5 K Superconductor Nb_2InC*", JETP Lett. **91** (2010) 410.

[48] C. Li, B. Wang, Y. Li, and R. Wang, "*First-principles study of electronic structure, mechanical and optical properties of V_4AlC_3*," J. Phys. D: Appl. Phys. **42** (2009) 065407.

[49] C. Li, J. Kuo, B. Wang, Y. Li, and R. Wang, "A new layer compound Nb_4SiC_3 predicted from first-principles theory," J. Phys. D: Appl. Phys. **42** (2009) 075404.

[50] D. Nguyen, V. Vitek, and A.P. Horsfield, "*Environmental dependence of bonding: A challenge for modeling of intermetallics and fusion materials*," Progr. Mater. Sci. **52**, (2007) 255.

[51] Z.M. Sun, H. Hashimoto, Y. Zou, and S. Tada, "*Synthesis of ternary compounds Cr_2GaC and Ti_2GaC*," Proc. 2006 Autumn Meeting of Japan Institute of Metals, Niyigata, Japan.

[52] J.M. Molina-Aldareguia, J. Emmerlich, J.–P. Palmquist, U. Jansson, and L. Hultman, "*Kink formation around indents in laminated Ti_3SiC_2 thin films studied in the nanoscale*," Scrip. Mater. **49** (2003) 155.

[53] H.Y. Gou, L. Hou, J.W. Zhang, and F.M. Gao, "*Pressure-induced incompressibility of ReC and effect of metallic bonding on its hardness*," Appl. Phys. Lett. **92** (2008) 241901.

[54] S. Li, R. Ahuja, M.W. Barsoum, P. Jena, and B. Johansson, "*Optical properties of Ti_3SiC_2 and Ti_4AlN_3*," Appl. Phys. Lett. **92** (2008) 221907.

[55] R. Saniz, L. H. Ye, T. Shishidou, and A.J. Freeman, "*Structural, electronic, and optical properties of $NiAl_3$: First-principles calculations*," Phys. Rev. B **74** (2006) 014209.

[56] C.Y. Allison, F.A. Modine, and R.H. French, "*Optical and electrical properties of niobium carbide*," Phys. Rev. B **35** (1987) 2573.

[57] D.W. Lynch, C.G. Olson, D.J. Peterman, and J.H. Weaver, "*Optical properties of TiC_x ($0.64 \leq x \leq 0.90$) from 0.1 to 30 eV*", Phys. Rev. B **22** (1980) 3991.

[58] M. Xu, S. Wang, G. Yin, J. Li, Y. Zheng, L. Chen, and Y. Jia, "*Optical properties of cubic Ti_3N_4, Zr_3N_4, and Hf_3N_4*", Appl. Phys. Lett. **89** (2006) 151908.

[59] J.S. de Almeida, and R. Ahuja, "*Electronic and optical properties of RuO_2 and IrO_2*," Phys. Rev. B **73** (2006) 165102.

[60] G. Yu, C.H. Lee, A.J. Heeger, and S.W. Cheong, "*Photoconductivity and optical conductivity in lightly doped $Nd_2CuO_{4-\delta}$*", Physica C **203** (1992) 419.

[61] M.W. Barsoum, T. El-Raghy, W.D. Porter, H. Wang, J.C. Ho, and S. Chakraborty, "*Thermal properties of Nb_2SnC*," J. Appl. Phys. **88** (2000) 6313.

[62] W.L. McMillan, "*Transition Temperature of Strong-Coupled Superconductors*," Phys. Rev. **167** (1968) 331.

[63] S.E. Lofland, J.D. Hettinger, T. Meehan, A. Bryan, P. Finkel, S. Gupta, M.W. Barsoum, and G. Hug, "*Electron-phonon coupling in $M_{n+1}AX_n$-phase carbides*," Phys. Rev. B **74** (2006) 174501.

[64] J.D. Hettinger, S.E. Lofland, P. Finkel, , T. Meehan, J. Palma, K. Harrell, S. Gupta, A. Ganguly, T. El-Raghy, and M.W. Barsoum, "*Electrical transport, thermal transport, and elastic properties of M_2AlC (M = Ti, Cr, Nb, and V)*," Phys. Rev. B **72** (2005) 115120.

7. Conclusions

First-principles calculations based on density functional theory have been carried out to investigate the structural stability, elastic properties, electronic structure, Fermi surface, theoretical hardness, optical functions, and thermodynamic properties of the four 211 MAX superconducting phases Mo_2GaC, Nb_2AsC, Nb_2InC, and Ti_2GeC. The evaluated structural parameters at zero pressure are in excellent agreement with the available theoretical and experimental data. The pressure effect on the structural properties of these nanolaminates shows that both the lattice constants and unit cell volume decrease almost linearly with the increase of pressure. On the other hand, the hexagonal ratio increases gradually with increasing pressure. These mean that, the lattice constant *a* decreases with a faster rate than *c*. Therefore, the compressibility along c-axis is lower than that along the a-axis.

The calculated elastic parameters allow us to conclude that the superconducting phases are mechanically stable compounds. In addition, they are characterized as brittle material and show elastic anisotropy. Comparatively, Mo_2GaC and Nb_2AsC possess large elastic anisotropy in comparison with other two phases. The elastic constants at different pressures satisfy the Born criteria for the mechanical stability of the studied four MAX phases and show the monotonous increase of the five independent elastic constants C_{ij} with the pressure up to 50 GPa. Nb_2AsC has the highest bulk modulus, shear modulus and Young modulus among the studied four superconducting MAX phases. As a result, Nb_2AsC is the most difficult to be compressed. It is also stiff and can withstand shear strain to the largest extent. The relatively low values of Poisson's ratios of the four nanolaminates indicate their high degree of directional covalent bonding. The pressure effect on polycrystalline elastic properties such as bulk modulus, shear modulus and Young's modulus results their monotonous increase with increasing pressure. The G/B ratios decrease with increase of pressure and consequently, the brittleness of the four compounds should decrease gradually with continuous increase of pressure.

The electronic structures of the four MAX superconductors reveal that they are metals and exhibit covalent nature. Moreover, the M-C bonds possessed stronger covalent bonding than the M-M bonds. At around the Fermi level, the DOS mainly originates from the M *d* states. The M *d*-C *p* hybridization is the driving force in the structure and the presence of A-atoms changes the M-C-M-C covalent bond chain into a M-C-M-A bond chain, forming a layered structure. The Fermi surfaces are formed mainly by the low-dispersive bands, which should be responsible for the presence of superconductivity in Mo_2GaC, Nb_2AsC, Nb_2InC and Ti_2GeC. The optical properties such as dielectric function, refractive index, absorption spectrum, energy-loss function, reflectivity, and photoconductivity are determined and analyzed in detail. The optical properties such as refractive index, reflectivity, and photoconductivity are found to be polarization dependent. The reflectivity spectra imply that the studied MAX phases are potential candidate materials for coating to reduce solar heating.

Finally, the temperature and pressure dependence of volume thermal expansion coefficient, bulk modulus, Debye temperature, and specific heats are investigated successfully using the quasi-harmonic Debye model and the results are discussed. The increase of specific heats with temperature indicates that phonon thermal softening occurs when the temperature increases. The estimated electron-phonon coupling constants signify that the four MAX phases are moderately coupled superconductors. The present study provides us with clear indications of small anisotropy in the elastic and optical properties of the four superconducting MAX phases. In conclusion, we hope that these findings will stimulate experimental effort to investigate the optical and thermodynamic properties of the four superconducting 211 MAX phases.